



HAL
open science

Cement foam stability : link with cement paste rheological properties

Blandine Feneuil

► **To cite this version:**

Blandine Feneuil. Cement foam stability : link with cement paste rheological properties. Materials. Université Paris-Est, 2018. English. NNT : 2018PESC1045 . tel-02084040

HAL Id: tel-02084040

<https://pastel.hal.science/tel-02084040>

Submitted on 29 Mar 2019

HAL is a multi-disciplinary open access archive for the deposit and dissemination of scientific research documents, whether they are published or not. The documents may come from teaching and research institutions in France or abroad, or from public or private research centers.

L'archive ouverte pluridisciplinaire **HAL**, est destinée au dépôt et à la diffusion de documents scientifiques de niveau recherche, publiés ou non, émanant des établissements d'enseignement et de recherche français ou étrangers, des laboratoires publics ou privés.

UNIVERSITÉ
— PARIS-EST



Navier



IFSTAR

THÈSE

pour obtenir le grade de docteur délivré par

Université Paris-Est

Spécialité doctorale “**Sciences des matériaux**”

**Stabilité des mousses de ciment :
lien avec les propriétés rhéologiques
de la pâte de ciment**

***Cement foam stability:
link with cement paste rheological properties***

présentée et soutenue publiquement par

Blandine FENEUIL

le 11 octobre 2018

devant le jury composé de

Mme	Véronique SCHMITT	Présidente du jury
Mme	Anne-Laure BIANCE	Rapporteure
M.	Guillaume OVARLEZ	Rapporteur
M.	Jean-Baptiste D'ESPINOSE DE LACAILLERIE	Examinateur
M.	Pascal BOUSTINGORRY	Invité
M.	Nicolas ROUSSEL	Co-directeur de thèse
M.	Olivier PITOIS	Directeur de thèse

Abstract

Cement foam advantages compared to normal concrete are its low density, low material need and thermal insulation capacity. To better understand how the morphology of cement foam affects its properties, we wish to create solid samples with well controlled structure. This involves two steps: the creation of a fresh cement foam with chosen structure, and the stability of this structure up to cement hardening. First step is ensured by our preparation protocol, and second step is investigated in this thesis.

First, we study the interaction of surfactants and cement paste. Some surfactants cannot stabilize foam in cement paste highly alkaline solution. Some others, mainly anionic surfactants, adsorb on cement grain surface, which modifies interactions between cement grains and consequently the yield stress of the cement paste. At low surfactant concentration, cement grain surface becomes hydrophobic and yield stress increases due to hydrophobic attraction between cement grains. At high surfactant concentration, adsorbed micelles create a steric repulsion between cement grains and make cement paste yield stress drop.

Second, we study the effect of bubbles on the yield stress of aerated cement paste, at air content below 40%. The measured yield stress is normalized by the yield stress of the suspending cement paste. For a surfactant with low affinity to cement grains surface, results are consistent with literature, whereas dimensionless yield stress is much higher than expected when surfactant strongly adsorbs on cement grain surface. This effect is attributed to the change of the bubble surface properties due to the adsorption of hydrophobic cement grains at the air-liquid interface.

Then, we focus on cement foam stability, at air content 83%. We first study three series of experiments at given water-to-cement ratio and bubble size. For each series, the yield stress of the cement paste is changed by addition of superplasticizer or high amount of anionic surfactant. Unexpectedly, the best foam stability is obtained for relatively low yield stress. Rheological measurements on the fresh cement foams allowed us to understand this improved stability as a consequence of the reorganization of cement grains into denser packing. In a second part on stability, we study the influence of bubble size, water-to-cement ratio and surfactant content. A stability criterion is defined from the bubble size and the interstitial cement paste yield stress.

Eventually, we observe that cement foam structure affects water imbibition velocity. Imbibition front is slowed down when it crosses the constrictions between the bubbles.

Résumé

Les mousses de ciment présentent d'intéressantes propriétés : une faible densité, une faible consommation de matière première et une bonne résistance thermique. Certaines de ces propriétés dépendent de sa morphologie. Pour mieux comprendre cette dépendance, on veut créer des échantillons de mousse de ciment avec une structure bien contrôlée : les bulles sont de même taille, et les quantités d'air, de ciment, d'eau et de tensioactif sont fixées. Pour ce faire, on mélange d'une part une mousse aqueuse de morphologie contrôlée, stabilisée par des tensioactifs, et d'autre part une pâte de ciment. Le but de cette thèse est d'étudier comment conserver cette structure jusqu'à la prise du ciment.

Tout d'abord, nous étudions l'interaction entre tensioactifs et pâte de ciment. Certains tensioactifs ne sont pas compatibles avec la solution alcaline présente dans la pâte de ciment et ne permettent pas de produire une mousse dans ces conditions. Parmi les tensioactifs compatibles avec la solution interstitielle de ciment, certains s'adsorbent sur les grains de ciment. Cette adsorption change les interactions entre grains de ciment et par conséquent, la contrainte seuil de la pâte. A faible concentration en tensioactif, la monocouche de molécules adsorbée rend les grains de ciment hydrophobes, ce qui produit une attraction hydrophobe entre grains et une augmentation de la contrainte seuil de la pâte. A forte concentration en tensioactif, les micelles adsorbées engendrent une répulsion stérique entre les grains de ciment et une chute de la contrainte seuil.

Dans un deuxième temps, nous étudions l'effet des bulles d'air sur la contrainte seuil d'une pâte de ciment aérée, lorsque celle-ci contient moins de 40% d'air. Les mesures sont normalisées par la contrainte seuil de la pâte interstitielle afin d'être comparées à la littérature. Lorsque le tensioactif utilisé s'adsorbe peu sur les grains de ciment, les résultats sont semblables à ceux de la littérature obtenus sur des fluides à seuil modèles. En revanche, lorsque le tensioactif utilisé a une grande affinité avec les grains de ciment, la contrainte seuil normalisée est bien supérieure aux prédictions. Notre hypothèse pour expliquer ce résultat est une modification des propriétés de surface des bulles à cause de l'adsorption des grains de ciment rendus partiellement hydrophobes par le tensioactif.

Ensuite, nous nous focalisons sur la stabilité des mousses de ciment avant la prise, pour une fraction d'air de 83%. On s'intéresse tout d'abord à trois séries de mesures, en gardant pour chacune d'elles le rapport eau/ciment et la taille des bulles constants. Pour chacune des trois séries, seule la contrainte seuil de la pâte de ciment est changée par l'addition de superplastifiant ou d'une grande quantité de tensioactif anionique. On obtient alors un résultat inattendu : la meilleure stabilité est observée lorsque la pâte de

ciment utilisée pour faire la mousse est fluide. Les mesures des propriétés rhéologiques de la mousse nous font émettre l'hypothèse que la bonne stabilité aux faibles contraintes seuil de pâte de ciment est due à la réorganisation des grains de ciment en un réseau granulaire plus dense. Pour aller plus loin sur l'étude de la stabilité des mousses, nous faisons ensuite varier la taille des bulles, le rapport eau/ciment et la quantité de tensioactif. Nous définissons un critère de stabilité pour l'ensemble de ces mousses, qui dépend de la contrainte seuil interstitielle de la pâte de ciment confinée par les bulles et de la taille des bulles.

Pour finir, nous mesurons la vitesse d'imbibition des échantillons solides. Nous observons que la vitesse est plus faible que celle attendue, à cause d'un ralentissement du front d'eau lors du passage des constriction entre les bulles.

Remerciements

Ce travail a été financé par le Labex MMCD et s'est déroulé au laboratoire Navier.

Il a bénéficié des contributions d'un grand nombre de personnes que je tiens à remercier, et dont je ne vais citer qu'une petite partie puisque la liste exhaustive remplirait trop de pages.

Merci tout d'abord à mes encadrants Oliver et Nicolas, pour le temps que nous avons passé à analyser les derniers résultats et décider de nouvelles expériences à mener.

Merci à tous les expérimentateurs croisés dans les laboratoires, jamais avares de conseils sur les méthodes de préparation et sur les dispositifs expérimentaux, pour votre compassion devant les expériences ratées, votre aide pour qu'elles soient réussies, et votre bonne humeur pendant les journées de ménage. Merci aux Kepleriens, Julie, Laurent, Yacine, Florence, Jennifer, Ilham, Yousra, Michel, Marie, Meng, Xiao, Oumar, Francesco, Gaétan, Thibault, Elie, etc ; à l'équipe de Bienvenüe, Patrick, Daniel, Hela, Nadia, Aileen, etc; et tout particulièrement à l'équipe mousse, avec qui j'ai pu partager la joie d'admirer la structure cristalline des mousses monodisperses ordonnées : Olivier, François, Aymeric, Asmaa, Luana, Charles.

Merci à l'équipe technique, David, Cédric et Christophe pour votre patience lors des demandes de nouvelles pièces et votre rapidité pour les fabriquer.

Merci pour l'aide pour les démarches administratives, tout particulièrement à Sandrine.

Merci pour les kilomètres parcourus pendant la pause déjeuner en nageant et (surtout !) en courant, nécessaires à la concentration pendant les après-midi de bibliographie ou d'expériences, à Julie, David, Laurent, Yacine, Cédric, Denis, Jennifer, Alizée, Marie, Rémy, François, Asmaa, Gaétan, Thibault, Elie, etc.

Merci pour tous les moments de convivialité, très souvent autour d'une tasse de thé, moments privilégiés pour échanger divers conseils et réflexions existentielles sur le but de la recherche, à tous les collègues croisés à Kepler, à Bienvenüe, aux Ponts et au cours des conférences, ainsi qu'à mes amis et ma famille.

Contents

Contents	viii
Introduction	1
1 State of the art	3
1.1 Introduction	4
1.2 Aerated concrete	5
1.2.1 Production methods	5
1.2.1.1 Chemical foaming	5
1.2.1.2 Physical foaming	5
1.2.2 Properties	6
1.2.2.1 Density and compressive strength	6
1.2.2.2 Thermal resistance	7
1.2.2.3 Rheology	8
1.3 Fresh cementitious materials	9
1.3.1 Suspension	9
1.3.2 Yield stress fluid	10
1.3.3 Hydration and thixotropic behavior	11
1.3.4 The role of chemical admixtures	12
1.3.5 Surfactants in cement paste	13
1.4 Aqueous foams	14
1.4.1 Surface tension and Laplace's law	14
1.4.2 Role of surfactant in foams	14
1.4.3 Foam structure	15
1.4.4 Foam stability	17
1.4.4.1 Drainage	17
1.4.4.2 Coalescence	18
1.4.4.3 Ostwald ripening	19
1.4.5 Foam rheology	19
1.4.5.1 Solid regime	20
1.4.5.2 Flow	20
1.4.6 Conclusion on aqueous foams	20
1.5 Complex foams and bubble suspensions	21
1.5.1 Hydrophobic particles	21

1.5.2	Hydrophilic particles	24
1.5.3	Yield stress fluid	25
1.5.4	Rheology of complex foams and bubble suspensions	26
1.5.4.1	Aerated yield stress fluids	26
1.5.4.2	Granular foams	28
1.6	Conclusion	30
2	Effects of surfactants on the yield stress of cement paste	39
2.1	Introduction	40
2.2	Background	40
2.2.1	Surfactant molecules in cement paste	40
2.2.2	Foam stability	42
2.2.3	Yield stress of solid suspensions	43
2.3	Materials and methods	44
2.3.1	Materials	44
2.3.1.1	Cement	44
2.3.1.2	Synthetic cement pore solution	44
2.3.1.3	Surfactants	44
2.3.1.4	Cement paste preparation	44
2.3.2	Methods	46
2.3.2.1	Surfactant compatibility with cement pore solution	46
2.3.2.2	CMC	46
2.3.2.3	Yield stress	46
2.3.2.4	Adsorption	47
2.3.2.5	Contact angle	47
2.4	Results and discussion	48
2.4.1	Surfactants in synthetic cement pore solution	48
2.4.2	Adsorption sites and surfactant distribution	50
2.4.3	Relation between yield stress and adsorbed surfactant	53
2.4.3.1	Yield stress drop at high concentration range	53
2.4.3.2	Yield stress increase at low concentration range	54
2.5	Conclusion	55
	Bibliography	58
	Appendix A: Additional surfactants	59
	Appendix B: Compatibility with calcium hydroxide solution	61
	Appendix C: Delay of hydration	62
3	Yield stress of aerated cement paste	63
3.1	Introduction	63
3.2	Materials and methods	65
3.2.1	Materials	65
3.2.2	Method	65
3.2.2.1	Preparation of aerated and reference cement paste	65
3.2.2.2	Foam generation	66

3.2.2.3	Samples	67
3.2.2.4	Yield stress measurement	67
3.3	Results	68
3.3.1	Reference yield stress	68
3.3.2	Aerated cement paste	69
3.4	Discussion	70
3.4.1	Reference yield stress with surfactant	70
3.4.1.1	Reference yield stress with TTAB	71
3.4.1.2	Reference yield stress with Bio-Terge	72
3.4.2	Dimensionless yield stress	72
3.4.3	Bare bubbles (TTAB)	73
3.4.4	Particle covered bubbles	75
3.5	Conclusion	77
	Bibliography	80
4	Optimal cement paste yield stress for the production of stable cement foams	81
4.1	Introduction	82
4.2	Materials and methods	83
4.2.1	Materials	83
4.2.2	Methods	84
4.2.2.1	Protocol	84
4.2.2.2	Precursor foam	84
4.2.2.3	Mixing	84
4.2.2.4	Final stability	85
4.2.2.5	Rheological measurement	86
4.2.2.6	Water suction out of the cement pastes	86
4.2.3	Cement paste yield stress	86
4.3	Results	88
4.3.1	Stability	88
4.3.2	Rheological measurements	90
4.3.2.1	Foam yield stress	90
4.3.2.2	Elasticity	90
4.3.3	Water suction	91
4.4	Discussion	92
4.4.1	Comparison with aqueous foams	92
4.4.2	Early age rheological properties	93
4.4.3	Time evolution of rheological properties	95
4.4.4	Stability loss at very high surfactant content	97
4.5	Conclusion	98
	Bibliography	101

5	Stability criterion for fresh cement foams	103
5.1	Introduction	104
5.2	Materials and methods	105
5.2.1	Materials	105
5.2.1.1	Cement	105
5.2.1.2	Surfactants	105
5.2.2	Methods	106
5.2.2.1	Precursor foam and mixing	106
5.2.2.2	Protocol	106
5.2.2.3	Observation of stability	107
5.2.2.4	Stability of aqueous foam	107
5.2.2.5	X-ray tomography	108
5.2.3	Properties of cement paste	108
5.2.3.1	Yield stress of cement paste	108
5.2.3.2	Surface tension of cement paste	109
5.3	Results	110
5.3.1	Stability of aqueous foams	110
5.3.2	Drainage and ripening	110
5.3.2.1	Smaller bubbles ($R \lesssim 500 \mu\text{m}$)	110
5.3.2.2	Bigger bubbles ($R \gtrsim 500 \mu\text{m}$)	114
5.3.3	Influence of initial yield stress and bubbles size	116
5.4	Discussion	117
5.4.1	Destabilization mechanisms	117
5.4.2	Characteristic destabilization times	118
5.4.3	Effect of Bingham capillary number	119
5.4.4	15 min interstitial Bingham capillary number	121
5.5	Conclusion	122
	Bibliography	124
	Appendix A: aqueous foam stability	125
6	Water imbibition of open-cell cement foams	127
6.1	Introduction	127
6.2	Materials and methods	128
6.2.1	Materials	128
6.2.2	Cement foam production	128
6.2.3	Characterization of the foam morphology	129
6.2.4	Permeability measurement	130
6.2.5	Imbibition experiment	131
6.3	Results and discussion	131
6.4	Conclusion	136
	Bibliography	137
	Conclusion	139

A	Compressive resistance	I
A.1	Materials and methods	I
A.1.1	Materials	I
A.1.2	Sample preparation protocol	I
A.1.3	Compression tests	II
A.2	Results and discussion	III
A.2.1	Curve shape	III
A.2.1.1	Air content $\Phi > 75\%$, Steol and TTAB samples	III
A.2.1.2	Air content $\Phi < 40\%$	IV
A.2.2	Compression resistance	IV
A.2.2.1	Comparison with literature	IV
A.2.2.2	Effect of surfactant	V
A.2.2.3	Effect of W/C	V
A.2.2.4	Effect of bubble size	VI
A.3	Conclusion	VII

Introduction

Environment impact of buildings is considerable, both because of the material need for their construction and the energy demand during their life. Implementation of novel construction materials is required to save raw material resources and build energy efficient buildings. Partial replacement of solid by air bubbles offers a promising solution to address these issues. Aerated concrete, with varying air content from a few percent to 98%, provides a wide range of construction materials with reduced raw material need, reduced transport costs because of its low density, and improved thermal insulation properties.

Microstructural features of solid foams have significant impact on several functional properties. The size of the openings between the bubbles is known to play an important role on cement foam permeability and acoustic absorption capacity. The study of well-controlled cement foam samples is expected to provide better understanding of relation between foam morphology and functional properties.

The production of cement foams with well controlled morphology requires two steps. Firstly, a well-controlled fresh cement foam must be produced. Secondly, the controlled structure must not evolve as long as the cement has not hardened. However, when cement paste is fresh, the cement foam sometimes destabilizes: bubbles tend to raise and to grow. The goal of this work is to give hints to formulate stable cement foams. The role of the rheological properties of the cement paste is mainly investigated.

We describe in chapter 1 the preparation techniques and the main properties of the cement foams reported in the literature. The diversity of the formulations of these foams makes their comparison difficult. Then, we focus independently on the characteristics of fresh cement paste and on the properties of aqueous foams. At the scale of the cement grains, cement paste can be seen as solid particles interacting with each other, and suspended in alkaline solution. At the macroscopic scale, cement paste behaves like a yield stress fluid, i.e. it can flow under applied stress above its yield stress. Aqueous foams are also yield stress fluids. Besides, they are unstable systems due to the difference of density between liquid and air, and to the high energy required to create the numerous air-liquid interfaces. Three destabilization mechanisms occur: drainage is due to gravity, Ostwald ripening leads to gas transfer between the bubbles and coalescence is the breakage of walls separating neighbor bubbles. Finally, in the last part of chapter 1, we analyze literature results on complex foams to understand how fresh cement paste can affect stability and rheological properties of cement foams.

In chapter 2, we investigate the interaction between surfactants and cement paste,

without adding bubbles. We study the efficiency of surfactants, first in cement paste interstitial solution, and then in the presence of cement grains. In addition, we measure how surfactants adsorb on cement grains, and how adsorption affects the surface properties of the grains, the consistency of the cement paste and the setting time. We show in this chapter that if surfactant type and concentration are well chosen, it can be used as an additive in cement paste to make cement grain surface hydrophobic and to monitor the yield stress of the paste.

In chapter 3, we focus on aerated cement pastes at low air volume content, below 40%. We investigate the effect of the air inclusions on the yield stresses of the pastes and we compare our results with models and measurements performed on model yield stress fluids. We note and discuss a major difference between the cases when cement grains are hydrophobic and hydrophilic.

In chapter 4 and 5, we focus on cement foam stability, at air content 83%. In chapter 4, we change the yield stress of the cement paste by varying the amount of surfactant or superplasticizer, while water-to-cement ratio and bubble size are kept constant. Unexpectedly, remarkable stability is observed when cement paste yield stress is low, which coincides with a major enhancement of the yield stress due to confinement between the bubbles. In chapter 5, we study the influence of bubble size, water-to-cement ratio and surfactant content, in order to define a stability criterion for cement foams from the bubble size, the yield stress of the interstitial cement paste and the time evolution of the cement paste.

In chapter 6, we measure water imbibition of cement foams with open porosity, prepared with two different surfactants. Classic model cannot account for the low measured imbibition velocity. We attribute this effect to the morphology of solid foams. Indeed, we observe that water front is slowed down when it crosses the windows between the bubbles.

Lastly, some measurements of the compressive stress of cement foams samples are presented in Appendix A.

Chapter 1

State of the art

Sommaire

1.1 Introduction	4
1.2 Aerated concrete	5
1.2.1 Production methods	5
1.2.1.1 Chemical foaming	5
1.2.1.2 Physical foaming	5
1.2.2 Properties	6
1.2.2.1 Density and compressive strength	6
1.2.2.2 Thermal resistance	7
1.2.2.3 Rheology	8
1.3 Fresh cementitious materials	9
1.3.1 Suspension	9
1.3.2 Yield stress fluid	10
1.3.3 Hydration and thixotropic behavior	11
1.3.4 The role of chemical admixtures	12
1.3.5 Surfactants in cement paste	13
1.4 Aqueous foams	14
1.4.1 Surface tension and Laplace's law	14
1.4.2 Role of surfactant in foams	14
1.4.3 Foam structure	15
1.4.4 Foam stability	17
1.4.4.1 Drainage	17
1.4.4.2 Coalescence	18
1.4.4.3 Ostwald ripening	19
1.4.5 Foam rheology	19
1.4.5.1 Solid regime	20

1.4.5.2 Flow	20
1.4.6 Conclusion on aqueous foams	20
1.5 Complex foams and bubble suspensions	21
1.5.1 Hydrophobic particles	21
1.5.2 Hydrophilic particles	24
1.5.3 Yield stress fluid	25
1.5.4 Rheology of complex foams and bubble suspensions	26
1.5.4.1 Aerated yield stress fluids	26
1.5.4.2 Granular foams	28
1.6 Conclusion	30

1.1 Introduction

Construction industry faces everyday new challenges. Need of new infrastructures is growing; architectural innovations call for stronger and more flexible materials. At the same time, environmental issues require to save raw resources and to enhance energy efficiency of the new and renovated buildings.

Therefore, new construction materials must be developed. However, a successful new construction material has to meet lots of requirements such as low production cost, low environmental impact, thermal insulation, sound insulation, mechanical strength, durability, fire resistance and manufacturing/placement efficiency.

Cementitious materials fulfill a lot of these requirements. They are composed of a binder (usually a mixture including Portland cement), water and aggregates, most of which can be found near the construction site. They can be poured into molds or easily shaped during a few hours after mixing. After chemical reaction of cement with water, it possesses high compressive strength. In addition, it is fire resistant and lasts several decades, up to centuries. But it raises a major environmental concern because of the high amount of raw materials needed and the carbon dioxide released during cement manufacture.

Addition of small amount of air bubbles into concrete improves its life time in areas exposed to freeze-thaw cycles. In larger amount, it helps to save resources, reduce the material density and improve its thermal resistance. Aerated concrete is thus a promising material, as it combines the advantages of concrete while improving its environmental performance.

In this chapter, we will first briefly describe the fabrication methods and properties of aerated cementitious materials (part 1.2). We will see that the formulations and manufacturing methods are very numerous, and, therefore, the range of the final properties of these materials is very wide. This motivates the approach used in the following chapters, where we choose to prepare and study aerated materials with well controlled formulation and morphology. We will mainly deal with the manufacture and the early time evolution of well-controlled cement foams (chapters 2 to 5). This requires proper understanding of

the fresh properties of aerated cementitious material. These properties result from the behaviors of both the continuous phase (concrete, cement or mortar) and the bubbles. In part 1.3, we will give an overview of the properties of fresh cementitious materials. In parts 1.4 and 1.5, we will deal with foams.

1.2 Aerated concrete

1.2.1 Production methods

Two types of methods are used to add air bubbles into concrete, mortar or cement paste: chemical methods or physical methods. Note that materials are usually named in the literature accordingly to their fabrication method. Cellular concrete or autoclaved concrete refers to chemical foaming, while foamed concrete or cement foam refers to physical foaming [1].

1.2.1.1 Chemical foaming

Chemical foaming consists in adding to the mix slurry an additive which is able to react and produce gas. Produced gas remains stuck in the slurry and forms pores. This method is used for autoclaved aerated concrete. Autoclaved aerated concrete is a solution patented in the 1920's [2] to manufacture prefabricated lightweight concrete blocks. In this case, the additive is aluminium powder [3] which releases hydrogen in cement or concrete alkaline environment [4]. Aluminium grain size and quantity control the final size and volume of porosity [1]. Mechanical strength of autoclaved concrete is enhanced by curing at high temperature and pressure (190° C and 1.2 MPa) [1, 5]; this curing method is called autoclaving. Another common foaming agent for chemical foaming is hydrogen peroxide H_2O_2 [6, 7].

1.2.1.2 Physical foaming

Physical foaming methods require the use of surfactant molecules to avoid coalescence of bubbles. The effect of surfactant is detailed later in the next sections: in part 1.3.5, we study their effect in cement paste, and, in 1.4, how they stabilize aqueous foams.

Bubbles can be brought into cement/concrete slurry by two methods. First, bubbles can be entrained by fast mixing of the slurry ([8, 9, 10]). Surfactants used for this method are usually called air entraining agents (AEA). They are used, for instance, to create freeze-thaw resistant concretes, where air volume fraction is between 4 and 8%. Higher air volume fraction can also be reached. For instance, the fiber reinforced foams prepared by *Akthar & Evans* [11] have air volume content up to 95%. The morphology and the amount of the entrained bubbles are however hard to control, and the resulting foam can be unstable [1].

Precursor foam method allows a better control of the foamed cement properties [12]. Some authors also suggest that these foams have better thermal insulation capacities [7].

A separate precursor foam, i.e. an aqueous foam made of water and surfactant, is prepared and then incorporated into the slurry [13, 14, 15]. The morphology of the hardened cement depends on the bubble size distribution of the precursor foam and on the evolution of the bubbles during mixing and until cement hardening. Conservation of bubble size during mixing is however challenging. Paste consistency must be well chosen: if it is too fluid, bubbles tend to rise and escape from the mix, and if it is not fluid enough, bubbles tend to break [13, 16]. Both cases lead to a decrease of the incorporated air volume.

In this thesis, we focus on material with very well controlled structure, that is why the chosen manufacturing method is the precursor foam method (see chapters 3 to 6). Therefore, for the literature review on the properties of cement foams, we focus mainly on the foams obtained with this method; materials obtained by air entrainment or chemical foaming are only used when complements are necessary.

1.2.2 Properties

1.2.2.1 Density and compressive strength

Cement foams are first characterized by their low density. Many studies aim at improving the mechanical strength at a given density. For autoclaved aerated concrete, densities range from 300 kg/m^3 to 1200 kg/m^3 with compressive strength from about 1 to 10 MPa [2].

Cement foams prepared using physical methods usually have lower strengths. In Fig. 1.1, we can see compression strength as a function of density for samples prepared with precursor foam method as a function of density. On the whole, compression strength increases with density. The graph however illustrates the heterogeneity of the measured strengths: results obtained by *Jones & McCarthy* [14] are much below the measurements of *Tonyan & Gibson* [17] and *Abd & Abd* [18] at similar densities. At a given density, mechanical strength depends on the composition and on the preparation protocol of the cement foam. For instance, *Nambiar and Ramamurthy* [13] (red symbols in Fig.1.1) have noticed an important effect of the filler type on the cement foam resistance. *Falliano et al.* [19] measured the yield stress of cement foams made by the precursor foam method with various cements, surfactants, curing methods and water to cement ratio and observed that all these factors play a role on the hardened cement foam strength.

In many industrial applications, strength-density ratio of the cement foams must be optimized. From the literature results, we can distinguish three methods to go to this direction. The first one consists in increasing the strength of the concrete matrix. For instance, as mentioned previously, this is the role of autoclaving during the fabrication of autoclaved aerated concrete. The use of reinforcing fibers [11] and carbon nanotubes [20, 21] has also been studied. Secondly, some authors use a lighter concrete matrix; the air content at given density is therefore smaller. Lighter matrix can be obtained for example by the use of lightweight aggregates [12] and the replacement of sand by fly ash [13]. The third optimization mean could be the control of the bubble morphology, though, the effect of bubble morphology raises no consensus. In the strength-density model proposed

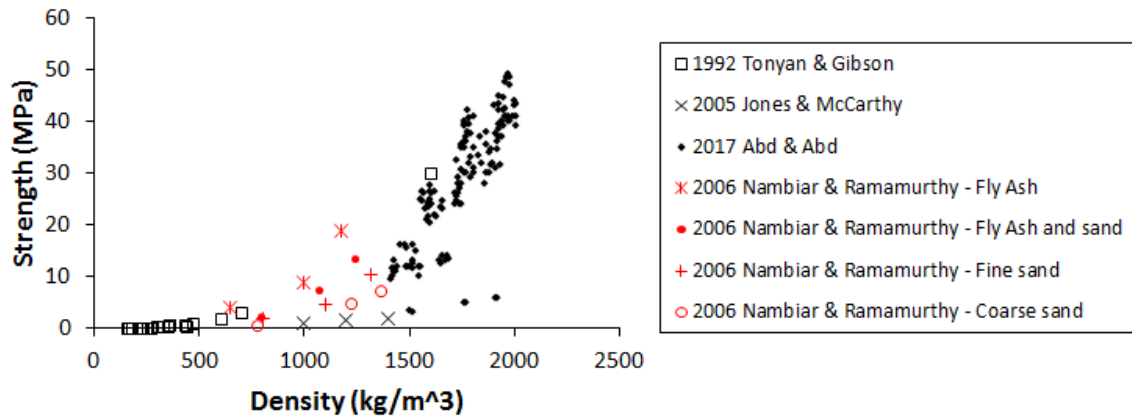


Figure 1.1: Compressive strength of some cement foams prepared by precursor foam method and measured 28 days after preparation. Empty back squares correspond to foams containing microsilica, polyester fibers and superplasticizer [17]; black crosses, sand [14]; black diamonds [18]. All red signs have been published in reference [13], different solid particles have been added to cement paste: fly ash (asterisks), fly ash and sand (dots), fine sand (crosses) coarse sand (circles).

by Hoff [22] and checked by Kearsley & Wainwright [23], no effect of the bubble morphology appears. However, Nambiar and Ramamurthy [13] suggest that the strength loss observed when fine sand is replaced by coarse sand is due to a non-homogeneous distribution of the air bubbles in the latter case. Some authors notice that decreasing water-to-cement ratio, although it increases the strength of the concrete matrix, decreases the cement foam compressive strength [19], they attribute this effect to the irregular shape of the bubbles. Some authors mention that best mechanical resistance is obtained when bubble size distribution is narrower [24, 25] and when bubbles are not connected [26, 27]. Others [1, 28] also suggest that the strength of chemically foamed concrete is better in the case of small and spherical bubbles.

However, a major difficulty to study the effect of foam structure on cement foam strength arises from the fact that, in the studies previously mentioned, the structure of the foam is not modified independently from the composition of the matrix. On the contrary, it results for instance from a change of paste fluidity or surfactant. As a consequence, the effect of foam structure on its final strength can hardly be distinguished from the modification of the strength of the cementitious matrix.

Some authors have also measured the tensile strength [7] as well as the compression elastic modulus [12] of aerated concrete. Similarly to compression strength, these mechanical properties also decrease when density decreases and are strongly related to the composition of the matrix.

1.2.2.2 Thermal resistance

Samson *et al.* [29] compare the thermal conductivities of lightweight concrete prepared with various methods: chemical foaming, air entrainment, pre-formed foam and lightweight

aggregate concretes (see Fig. 1.2). Thermal conductivity depends mainly on density, indeed, values obtained for lightweight aggregate concretes are similar to aerated concretes. Some authors report a linear relation between density and thermal conductivity [7]. In a minor extent, thermal conductivity depends also on the content on the continuous phase, for instance its moisture content [3]. A small dependence of the thermal resistance on the foam structure is observed by some authors [3, 30]. However, like mentioned previously in the case of compressive strength, porosity morphology has been changed by a modification of the formulation of the foam. For instance, in chemically produced metakaolin-blast furnace slag foams studied in [30], the size of the pores is changed with the concentration of added stabilizing surfactant.

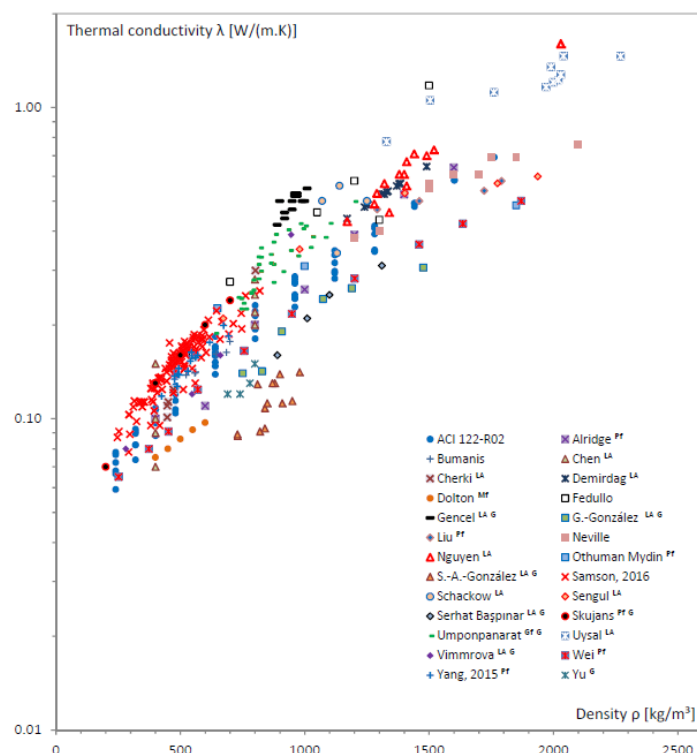


Figure 1.2: Thermal conductivity of lightweight concretes. Graph extracted from [29]. In the legend, LA corresponds to concrete containing lightweight aggregates; GF, to aerated concretes prepared with chemical foaming method; MF, to air-entrained concretes; PF, to pre-foaming method; G, to foamed gypsum.

1.2.2.3 Rheology

There is no consensus on the effect of bubbles on the fresh properties of cement foams. *Rixom and Mailvaganam* [16] report a decrease of fluidity when bubbles are entrained with some surfactant. On the contrary, *Aİtcin* [31] and *Ahmed et al.* [32] mention a reduction of the viscosity due to entrained bubbles.

1.3 Fresh cementitious materials

In literature concerning cementitious materials, a distinction is made between concrete, mortar and cement paste. Cement paste contains no aggregates whereas mortar includes fine aggregates (sand) and concrete, fine and coarse aggregates. In this work, we want to understand the interaction of foam and surfactant with cementitious materials. We therefore choose to study the most simple cementitious material, i.e. cement paste, containing only water and Portland cement. For the same reason, alternative binders such as fly ash and blast furnace slag, which are widely used in practice due to their lower environmental footprint, are not investigated here.

1.3.1 Suspension

Portland cement is mainly composed of clinker, obtained from limestone and clay. It is mixed, heated at 1450° and ground. It contains several oxides, mainly calcium oxide CaO ($\sim 60\%$) and silicium oxide SiO_2 ($\sim 20\%$), as well as Al_2O_3 , Fe_2O_3 , MgO , K_2O and Na_2O [33]. When it is mixed with water, some of the ions dissolve, and for several minutes up to hours, cement paste can be considered as a suspension of rigid particles in a strongly alkaline electrolyte solution. During this dormant period, the cement can be poured in mold or shaped. Then, chemical reaction between the cement oxides and water takes place and the formed hydration products bind the unreacted particles to form a solid material. We will discuss here only the properties of the fluid cement paste, before cement hydration.

Size of the cement grains range from about $1\ \mu\text{m}$ to $100\ \mu\text{m}$ with average about $10\ \mu\text{m}$ [34, 35]. The cement grains have irregular shape and very rough surfaces, the radius of curvature of the edges are of the order of magnitude of $500\ \text{nm}$ [34]. Cement powder specific surface area measured by Blaine apparatus is often close to $3000\text{-}4000\ \text{cm}^2/\text{g}$.

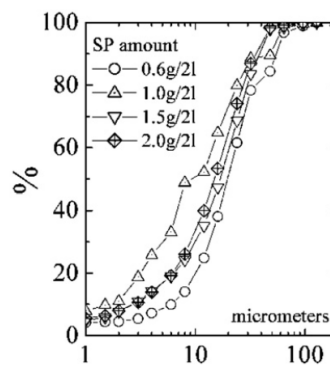


Figure 1.3: Example of volume distribution of cement grain size in water. Measure has been made with a laser granulometer, in the presence of various amounts of superplasticizer (SP) [36].

Cement density is close to $3.15\ \text{g}/\text{cm}^3$. Cement content of a paste is usually given in terms of the mass water-to-cement ratio W/C . For a cement paste, solid fraction Φ_p is related to the water-to-cement ratio by $\Phi_p = (W/C \times \rho_C / \rho_E + 1)^{-1}$, where ρ_C and ρ_E are the

densities of cement and water.

1.3.2 Yield stress fluid

A yield stress fluid is a material which can flow only if applied stress is above a critical stress, called yield stress and noted τ_y [37]. Below the yield stress, it behaves like an elastic solid, whose properties are often measured in a rheometer by applying oscillations of small strain amplitude. Above the yield stress, the material flows, and the shear rate $\dot{\gamma}$ depends on the applied shear stress τ .

In the case of cement paste, yield stress arises from attractive interactions between cement grains. A model, called Yodel (for yield stress model) has been derived by *Flatt and Bowen* [38] to relate the interactions at particle scale with the macroscopic yield stress of a solid suspension. Authors calculate how the unbroken bonds between solid particles affect the effective maximal solid volume fraction Φ_{max}^* of the suspension: when particles are connected to each other, they can be less effectively packed than unconnected particles, which reduces Φ_{max}^* . Solid suspension can flow only if solid volume fraction Φ_p is smaller than Φ_{max}^* . The yield stress calculated with this approach is:

$$\tau_y = m_1 \frac{\Phi_p^2 (\Phi_p - \Phi_{perc})}{\Phi_{max} (\Phi_{max} - \Phi_p)} \quad (1.1)$$

where Φ_{perc} is the minimum solid volume fraction required to create a percolated network of solid grains and Φ_{max} the maximal volume fraction of the grains with no attractive interaction. Φ_{perc} as well as Φ_{max} depend on the particle shape and size distribution. m_1 accounts for the intensity of the interparticle forces and is also related to the size distribution of the particles. The major particle forces are the electrostatic repulsion (for charged particles), the Van der Waals attraction and the steric repulsion (when some polymers are adsorbed on cement grain surface). Cement grains are charged, but due to high electrolyte content of cement paste interstitial solution, the range of the electrostatic repulsion is short: Debye length is $\kappa^{-1} \approx 0.7 \text{ nm}$ [39]. When molecules are adsorbed on solid grains and form a layer of thickness h_{ster} above κ^{-1} , they create a steric repulsion between cement grains and increase the interparticle distance h up to $2h_{ster}$. Van der Waal attraction depends on interparticle distance $F_{vdW} \propto 1/h^2$.

Flow properties of cement paste are well fitted with a Bingham model [34, 40, 41]:

$$\tau = \tau_y + \mu_d \dot{\gamma} \quad (1.2)$$

with μ_d the plastic viscosity of the paste. Both τ_y and μ_d are affected by the formulation of the paste. For instance, a rise of W/C increases not only the yield stress but also the plastic viscosity of the paste.

One of the methods to measure the yield stress consists in measuring the shear stress over a wide range of shear rates and fitting the results with Bingham model (equation 1.2). A second method is the start-of-flow curve: small constant shear rate is applied and shear stress is measured as a function of deformation. Yield stress is the maximum value

of the curve (see Fig. 1.4 (a) for a typical start-of-flow curve of cement paste). Different measurement methods can result in different values of the yield stress [36]. Note that the yield stress predicted by the Yodel corresponds to the start-of-flow method, and that this method will be used in the following chapters (see chapters 3 and 4).

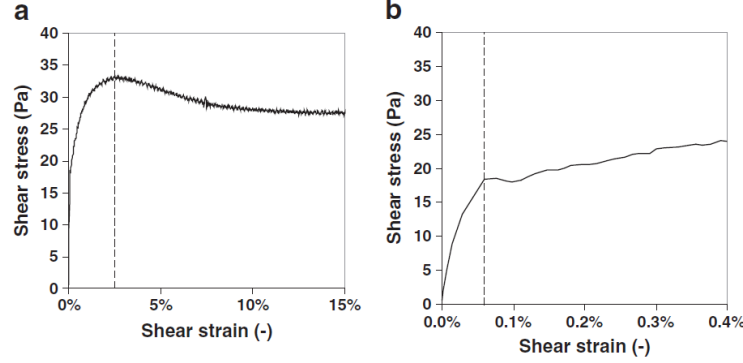


Figure 1.4: Example of start of flow curve of cement paste, with two different scales. Measured yield stress is the maximum observed in graph (a), the corresponding critical strain is 2.5%. On graph (b), the critical strain for C-H-S bonds is observed close to 0.05%. [35]

The formation of the structure of cement grains due to Van der Waals forces takes place in a few seconds. The critical strain of the percolated structure, i.e. the deformation needed to break the bonds, is a few percent.

When cement paste is at rest for several minutes, yield stress increases with time. Initial yield stress can be retrieved by a strong shearing of the cement paste. These observations remind the behavior of thixotropic materials [37, 41, 42]. Their cause is discussed below.

1.3.3 Hydration and thixotropic behavior

Cement paste hardening takes place through the nucleation and growth of hydration products, mainly calcium silicate hydrates (CSH). CSH nucleates preferentially in the pseudo contact zones between cement grains, i.e. at the places where the distance between solid surfaces is h . CSH hydrates act as solid bonds between cement grains and can be broken when cement paste is sheared. "Rigid" critical strain needed to break the CSH bond is much lower than the critical strain associated to flocculation: only a few hundredths of percent [35]. This small critical strain is illustrated in Fig. 1.4 (b). The elastic properties of cement paste due to CSH bond can be measured with oscillations tests: oscillations of strain amplitude $\epsilon_0 < 10^{-4}$ are applied, and stress response recorded. In-phase material response gives the elastic modulus, while out-of-phase response accounts for the viscous dissipation.

A typical elasticity evolution curve is shown in Fig. 1.5 (a). The network of CSH bond is formed in about 100 s. Then elastic modulus increases linearly with time due to the increase of the area of CSH bonds. Formation and growth of CSH bonds are also responsible for an increase of the yield stress. The stress at the rigid critical strain, i.e. about

0.05%, increases with time. After a few minutes, it overcomes the stress at the soft critical strain (about 2.5%). That is to say that the measured yield stress during the first minutes is related to the Van der Waals forces, whereas, after about 15 min, it is related to the CSH bonds and increases linearly with time [35] (see Fig. 1.5 (b)).

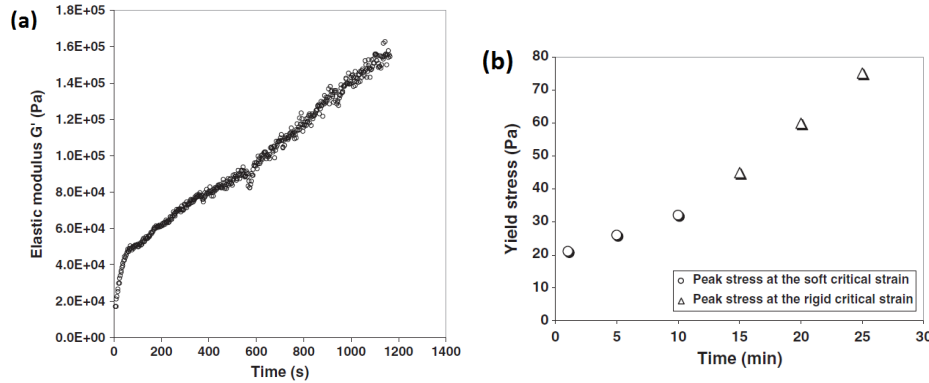


Figure 1.5: Evolution of the rheological properties of cement paste with time. (a): Elastic modulus, measured with strain oscillations, amplitude 0.03 % and frequency 1 Hz [35]. (b): Yield stress measured by start of flow curve [35].

1.3.4 The role of chemical admixtures

We have mentioned that, to prepare cement foams in chapters 3 to 5, we will add precursor aqueous foam to cement paste. The precursor foam contains surfactants. Adding chemical additives to cement paste can strongly affect its properties in the fresh state. Let us first say a few words about the common additives for concrete.

The most used of them are superplasticizers, which make the mix more fluid. Superplasticizers are polymers which adsorb on cement grain surface. Layers of adsorbed polymers (thickness h_{ster} is several nm) on neighboring grains cannot interpenetrate and create a steric repulsion. The increased separation distance h reduces the intensity of Van der Waals forces, which decreases the yield stress.

Rheological properties of cementitious materials can also be modified by the use of viscosity-modifying admixtures. With notation defined previously (see equation 1.2), they increase the plastic viscosity μ_d of the paste with no major modification of the yield stress τ_y . These additives are used for instance for self-compacting concrete, whose yield stress is very low, to maintain a homogeneous distribution of solid particles in the paste [43]. They are large polymers, which can either increase the viscosity of the interstitial solution, create bridges between cement grains by adsorbing simultaneously on several particles or produce depletion forces.

Some superplasticizers delay hydration of cement paste. This is often an undesirable effect due to the surface coverage of cement grains by the adsorbed polymers. When hydration retardation is required, other additives called retarders are used. Most of them are sugars. Their working mechanism is not yet perfectly understood; it may be related to preferential adsorption of these additives on the most reactive cement phases [44].

Other additives include setting accelerators and admixtures to prevent water from freezing.

1.3.5 Surfactants in cement paste

Surfactants, or “surface active molecules”, are also widely used concrete additives for two aims: air-entrainment in the production of freeze-thaw resistant concrete and shrinkage reduction. They are amphiphilic molecules, i.e. they are composed of a hydrophilic head and a hydrophobic tail. Surfactants are classified according to the nature of the hydrophilic head. They are called anionic if the head is negatively charged, cationic if it is positively charged, amphoteric or zwitterionic if both charges are present and non-ionic when it is not charged. In addition to the different hydrophilic heads, surfactants also differ by their molar mass. For usual synthetic surfactants, it is rather low: 288 g/mol for anionic sodium dodecyl sulfate (SDS) studied by [45] and 336 g/mol for cationic tetradecyltrimethylammonium bromide (TTAB). On the other hand, molar mass of proteins, used by [12, 46], is much bigger than SDS or TTAB, about 20 000 g/mol for instance for casein.

Several authors have observed that surfactants adsorb on cement grains. Fraction of adsorbed surfactant depends both on their chemical formula and on the cement composition [8, 47, 48]. Reported consequences of surfactant adsorption are a change of cement grains zeta potential [49], a hydrophobization of cement grains [49] and bridging between cement grains [16]. In addition, surfactants may interfere in cement hydration. Complexation with calcium ions is reported by [10, 45, 47] and modification of the structure of the hydration product crystals, by [10, 50]. Some authors have also measured a delay of hydration due to surfactants [47, 51, 52]; *Kuzielová et al.* [52] note that retardation can be avoided if low amount of surfactant is used.

Surfactants used for air-entrainment are called air entraining agent (AEA). They stabilize air bubbles which enter the paste during the mixing process. Most of AEA are negatively charged [10, 16, 43]. Some authors mention that voids are more stable in this case [8, 9]. Indeed, anionic surfactants tend to adsorb both on air-water interfaces and cement grain surfaces. They create bonds between cement grains and air bubbles, which avoids sedimentation of cement grains and rising of the bubbles.

Shrinkage reducing admixtures are often non-ionic surfactants. Shrinkage reduction is due to their ability to reduce the surface tension [43], and therefore, to decrease the internal stresses due to capillarity during hydration and drying of concrete (see parts 1.4.1 and 1.4.2 for the definition of surface tension and how it is affected by surfactants).

Effect of surfactant on the rheology of cement paste has hardly been studied independently from the consequences of bubbles addition. We can however mention the study of *Rixom and Mailvaganam* [16], who report an increase of apparent viscosity $\eta(\dot{\gamma}) = \tau/\dot{\gamma} = \tau_y/\dot{\gamma} + k$ for several mixing velocities (i.e. several shear rates $\dot{\gamma}$) when anionic surfactant is added. Non-ionic surfactant, on the other hand, has no effect on rheology.

This short literature review on surfactant in cementitious materials reveals that surfactants sometimes have the same consequences as usually concrete admixtures: they may

adsorb on cement grains, delay hydration, bridge the particles... However, these effects depend of the chemical formula of the surfactants. Systematic investigation of several surfactants is required to elucidate the consequences of surfactants in cement paste, in order to facilitate the selection of surfactants to formulate cement foams.

1.4 Aqueous foams

Foams have raised a lot of attention in the last decades due to their application not only in construction materials, but also in food industry, cosmetics, etc. They are materials containing two phases: gas bubbles are dispersed in a continuous phase. For all these materials, the final properties result, on the one hand, from the properties on the continuous phase, and on the other hand, from the role of the air bubbles. Let us first focus on liquid foams. The phenomena described in this part apply to precursor foams used for the cement foam fabrication (see part 1.2.1). In addition, they enlighten the role of the bubbles in the behavior of the cement foams. How the cement paste can affect this role is discussed in part 1.5.

We will only focus on the most important points to produce and understand cement foams. For a more detailed description of the physics of foams, the reader can refer to the books [53] and [54].

1.4.1 Surface tension and Laplace's law

The creation of an interface increases the free energy of the system proportionally to the surface area of the interface [55]. This additional surface energy is called surface tension and will be noted γ . In other words, surface tension is homogeneous to a force per unit length; it acts as a force that tends to reduce the area of the interface.

Surface tension leads to a difference of pressure between the phases of each side of the interface, called capillary pressure P_C and given by Laplace's law [53, 54, 55] (with R_1 and R_2 the major radii of curvature on the interface):

$$P_C = \gamma \left(\frac{1}{R_1} + \frac{1}{R_2} \right) \quad (1.3)$$

For example, in the case of an isolated bubble in a liquid, surface tension tends to reduce the size of the bubble. Major radii of curvature are equal, $R_1 = R_2 = R$, and Laplace's law becomes:

$$P_C = P_{gas} - P_{liq} = \frac{2\gamma}{R} \quad (1.4)$$

1.4.2 Role of surfactant in foams

Due to their specific shape, surfactants in solution tend to settle at air-liquid interface, with their hydrophilic head in the aqueous solution and their hydrophobic tail in the air. First consequence is a reduction of the surface energy: when surfactant concentration increases, surface tension γ decreases down to a minimal value. The minimal value

is reached at the surfactant critical micelle concentration (CMC), it is the concentration above which surfactant molecules gather into agglomerates, with their hydrophobic tail close to each other and hydrophilic head toward the solution. Surfactant agglomerates are called micelles. Surfactant effect on surface tension and distribution in solution is shown in Fig. 1.6.

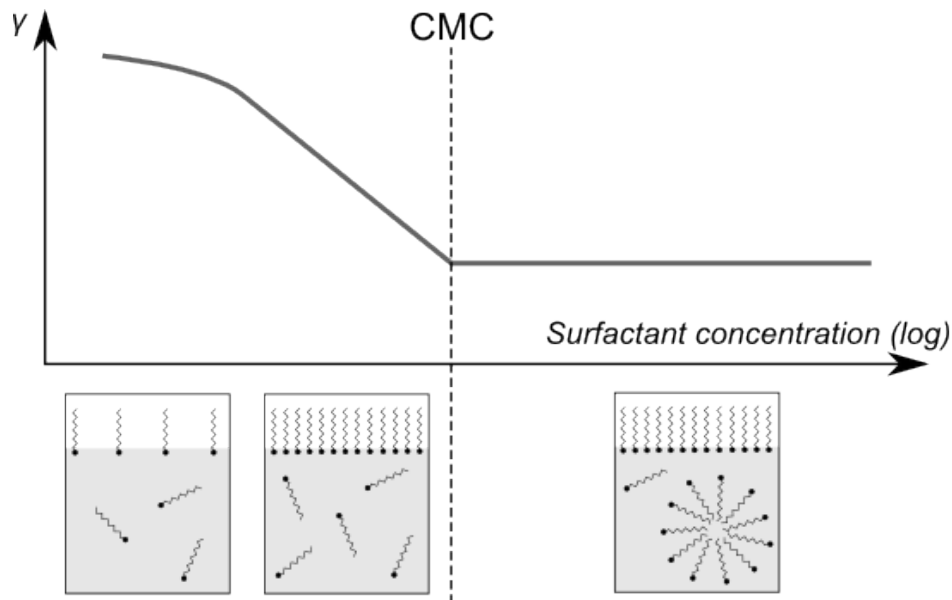


Figure 1.6: Effect of surfactants on air-water surface tension and surfactant distribution as a function of their concentration.

In addition, surfactant adsorbed layer at interfaces lead to a repulsion between the interfaces, which is essential to foam stability [53] (see paragraph 1.4.4).

Low molecular mass surfactant diffusion from bulk solution to interfaces is very fast [56]. Time needed to diffuse from the bulk solution to the interface is longer for proteins [56], therefore the surface tension value decreases slowly with time before reaching a minimum. This make the creation of a foam by shaking or strong mixing more difficult than in the case of low molecular mass surfactants. On the other hand, once adsorbed, proteins hardly desorb from the interface, which explains that the foams are very stable [53].

1.4.3 Foam structure

When the amount of air bubbles in a fluid is increased, surface tension tends to keep the bubbles spherical as long as their are not deformed by their neighbors. We call aerated materials with spherical bubbles “bubble suspensions”. In the following, we will distinguish the suspension regime from the foam regime, where the bubbles are deformed by their neighbors. Note that when continuous phase is a Newtonian liquid, bubble suspensions are in practice unstable because of buoyancy forces. Bubble suspensions will therefore not be studied in this part. We will mention them in part 1.5.

In a foam, air-liquid surface area is very large. Surface minimization strongly constraints the foam structure. The morphology of dry foams, i.e. when air fraction Φ is close

to 100%, is ruled by three laws, known as Plateau's laws from the name of the Belgian physicist who stated them in 1873 [53].

1. Two bubbles are separated by a liquid film of constant average curvature.
2. Three films join in channels called Plateau border and form 120° angles.
3. At each node, four Plateau borders intersect and form 109.5° angles.

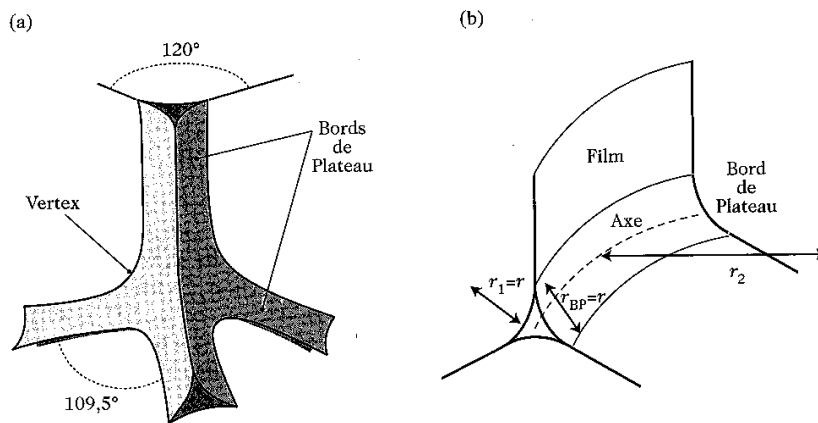


Figure 1.7: (a) Illustration of 2nd and 3rd Plateau's laws. (b) Schema of a Plateau border and notation of r , the radius of curvature of the Plateau border. Figure taken from [53].

When foams are dry, the volume of nodes and Plateau border is small. When the liquid volume fraction $\Phi_l = 1 - \Phi$ is increased, Plateau border volume increases and the surface of the liquid film between two bubbles decreases. The capillary pressure P_c , i.e. pressure difference between air and liquid in the Plateau borders, can be deduced from Laplace's law, which can be written with the notations defined in Fig. 1.7 (b) as:

$$P_c = P_{gas} - P_{liq} = \frac{\gamma}{r} \quad (1.5)$$

where r depends on the foam liquid fraction. To estimate its value, let us consider now monodisperse foams, where all the bubbles have the same size. When $\Phi_l < 6.3\%$, bubble configuration which minimizes the energy is body-centered cubic, whereas above 6.3% , it is face-centered cubic. Bubble in the body-centered cubic configuration is called Kelvin-Voigt cell. The following relation stands for Kelvin-Voigt cell when $\Phi_l \lesssim 1\%$ [53]:

$$r \approx R\sqrt{\Phi_l/0.33} \quad (1.6)$$

Bubbles being not spherical, R is defined as the radius of the spheres having the same volume as the bubbles.

1.4.4 Foam stability

We have seen that the morphology of a foam follows Plateau's laws and is affected by the liquid fraction. This morphology evolves with time: gravity leads to drainage, and ripening and coalescence tend to make the bubbles grow bigger, which reduces the interface quantity and therefore the total surface energy of the foam. The three foam destabilization mechanisms are illustrated in Fig. 1.8. Let us focus on each of them.

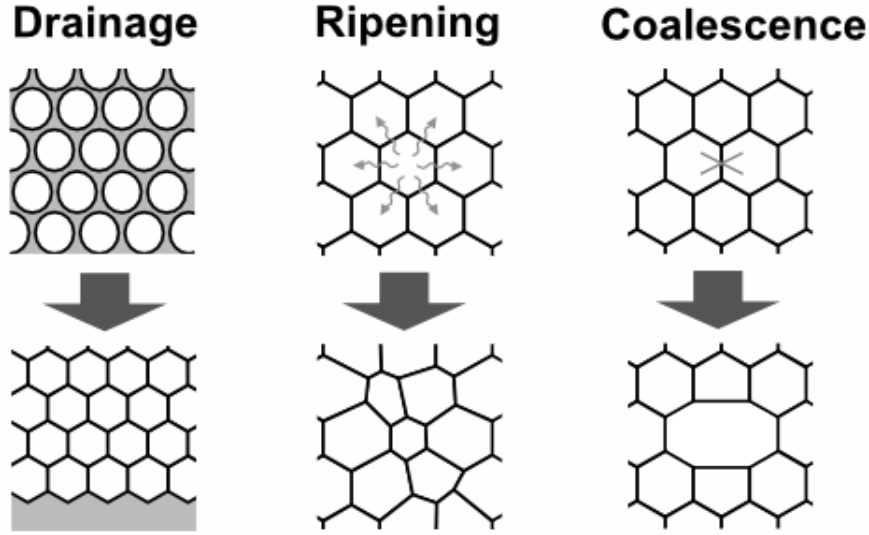


Figure 1.8: Schema of the three foam destabilization mechanisms.

1.4.4.1 Drainage

"Drainage" refers to the destabilization of the foam due to gravity. The interstitial fluid, denser than air bubbles, tend to flow towards the bottom of the foam.

In a liquid foam at equilibrium, the pressure in the liquid continuous phase is equal to the hydrostatic pressure: $P_{liq}(z) = P_{liq}(0) - \rho_l g z$, where ρ_l is the liquid density and $z = 0$ at the bottom of the foam, where the bubbles are spherical and air fraction is equal to the maximal volume fraction of disordered spheres $\Phi_c = 1 - \Phi_{l,c} = 64\%$. Together with equations 1.5 and 1.6, it shows that in a foam at hydrostatic equilibrium, the liquid fraction is imposed and depends on height [53]:

$$\frac{1}{\sqrt{\Phi_l(z)}} - \frac{1}{\sqrt{\Phi_l(0)}} \approx \frac{\sqrt{3}\rho_l^2 g^2 R z}{\gamma^2} \quad (1.7)$$

Examples of the liquid fraction profiles are drawn in Fig. 1.9.

When a liquid foam is not at hydrostatic equilibrium, liquid flows between the bubbles. Foam can be compared with a porous medium of porosity Φ_l and flow velocity can be predicted by the Darcy's law:

$$u = \frac{k}{\mu} \left(-\frac{dP_{liq}(z)}{dz} + \rho_l g \right) \quad (1.8)$$

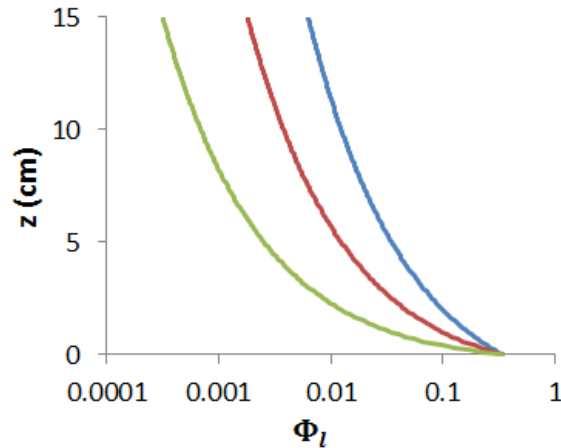


Figure 1.9: Liquid fraction as a function of height in a foam at hydrostatic equilibrium. Curves are plotted from equation 1.7 with $\gamma = 35$ mN/m, $\rho_l = 1000$ kg/m³ and several bubble sizes: blue curve, $R = 150$ μm ; red curve, $R = 300$ μm and green curve, $R = 750$ μm .

where the permeability k depends on the bubble size and on the liquid content. It is also affected by the surface viscosity and elasticity, which depends on the surfactant [53, 57].

The conclusion of this paragraph is that, for a given bubble size, gravity fixes the morphology of a simple liquid foam: liquid fraction and the radius of curvature of the Plateau borders are imposed at each height. As soon as the morphology of the foam differs from this structure, liquid flows inside the Plateau borders and nodes. To create cement foams and choose their air fraction, we will therefore need to rely on the complex behavior of cement paste.

1.4.4.2 Coalescence

Two neighbor bubbles are separated with a liquid film made of two air-liquid interfaces. Coalescence occurs when this film ruptures.

Film stability is due to the repulsion between the interfaces and is achieved thanks to the surfactants. Layers of adsorbed surfactant of each interface repel each other due to electrostatic repulsion (for ionic surfactants) and steric repulsion. The presence of non-adsorbed surfactant micelles, or protein or polymer in the film can also enhance interface repulsion [53]. The thickness of the film is typically a few tens of nanometers for low molecular weight surfactants, and can be bigger for instance in the case of proteins [53, 57].

Studies on an isolated film shows that the film ruptures when the pressure in air on each side of the film reaches a critical value, the maximal disjoining pressure, which can be deduced from the above described interface interactions. However, in a foam, film rupture can be observed even if bubble pressure is below the maximal disjoining pressure. Dynamic effect play also a role. For instance, creation of a new film during topological rearrangement can lead to rupture if liquid fraction is too low [58].

Key point is that the repulsion between interfaces depends not only on the chosen surfactant and its concentration, but also on the liquid composition. In particular, electrostatic repulsion has no effect if the distance separating the interfaces is above twice the Debye length [56]. The Debye length decreases when the concentration of ions in the solution decreases. Therefore, surfactant which are able to stabilize a foam in water might not be as efficient in cement paste, where electrolytes concentration is very high.

1.4.4.3 Ostwald ripening

As a consequence of Laplace's law, pressure in the smaller bubbles is higher than in the bigger bubbles. As gas migrates from the high pressure areas to the lower pressure areas, the size of the smaller bubbles keeps decreasing until they disappear. This phenomenon, called Ostwald ripening, leads to a reduction of the number of bubbles in time and to an increase of their average radius. In a foam, gas crosses the liquid films. A freshly prepared foam first undergoes a transient regime, during which ripening occurs only locally. Then, during the so-called auto-similar regime, the average radius of the bubbles is proportional to the square root of the time. In a bubble suspension where there is no film between the bubbles, ripening is slower: average radius increases as the cubic root of the time.

Ripening velocity of a 3D aqueous foam depends on several factors. Firstly, ripening depends on the morphology of the foam. If the foam is initially monodisperse, ripening is very slow at the beginning: after an induction period where no change can be observed, the transient regime occurs. Then the auto-similar regime finally takes place. In addition, ripening is faster if the initial bubble size is smaller. Secondly, the nature of the gas affects ripening: the less soluble the gas is, the slower the ripening. Thirdly, surfactant plays a major role: increasing the film thickness, creating of a less permeable layer near the interface and increasing the surface elastic modulus all slow down ripening [57, 59].

1.4.5 Foam rheology

Let us say a few words about emulsions. Emulsions are a suspension of liquid drops in a non-miscible liquid continuous phase. Like air-water interfaces, the interface between both immiscible liquids can be stabilized by surfactants. Concentrated emulsions, i.e. where dispersed phase volume fraction is above the maximal sphere volume fraction, possess a structure very similar to foams. Emulsion destabilization mechanisms are the same as for foams, but they are usually slower, which makes their study easier. In particular, liquid phases can have the same density and drainage effects can therefore be discarded. This makes experimental investigation of the rheology of emulsions easier than for foams. Most results obtained on emulsions are however true for foams [60, 61] and we will use them in this paragraph.

Foams (and concentrated emulsions) are yield stress fluids. When applied stress is small, bubbles stay in place while films and Plateau borders elongate: foams behave like an elastic solid. When applied stress is above the yield stress, bubbles displacement makes the foam flow.

1.4.5.1 Solid regime

Similarly to cement paste (see part 1.3.3), elastic properties of foams and emulsions in the solid regime can be measured by oscillation tests. Viscous modulus is one order of magnitude below the elastic modulus [61].

Foam elastic modulus does not depend on oscillation frequency in the range 0.01 - 1 Hz. For a monodisperse foam, it is related to foam structure by equation 1.9. This empirical relation has been first obtained on emulsions [62] with cone and plane geometry and Couette geometry. It has been later confirmed with a Couette tool on foams [60, 61]:

$$G'_{aq} = \alpha \frac{Y}{R} \Phi (\Phi - \Phi_c) \quad (1.9)$$

where α value is 1.4 according to [60, 61], while the value measured by [63] is 1.8.

The critical strain can be of the order of magnitude of 1 for dry foams and decreases down to zero when liquid content increases and bubbles or drops become spherical [53, 61, 64].

1.4.5.2 Flow

Flow curve for liquid foams can be modelled by an Hershel-Bulckley law [61, 65, 66, 67]:

$$\tau_y = \tau_{y,aq} + k \dot{\gamma}^n \quad (1.10)$$

The exponent n is about 0.5 in the absence of viscous dissipation and shear thinning effects in films, and below otherwise [61, 67]; it is therefore affected by surfactant. The plastic viscosity μ_d depends on the air fraction.

Yield stress dependence on liquid fraction has been experimentally observed for emulsions [64] and for foams [60]:

$$\tau_{y,aq} = \alpha \frac{Y}{R} (\Phi - \Phi_c)^2 \quad (1.11)$$

Coefficient α depends on the measurement method. In [53], it is mentioned that α varies between 0.2 and 0.5; value measured in [68] is 0.6.

1.4.6 Conclusion on aqueous foams

Production of an aqueous foam is possible thanks to the stabilization of the liquid films between the bubbles by surfactants. The morphology of a monodisperse foam at given air fraction and bubble size is ensured by the surface tension. However, foam destabilization due to drainage, ripening and coalescence makes the control of the liquid fraction and bubble size difficult. This raises major challenges to manufacture cement foams with controlled morphology.

Cement foam stability issues are sometimes solved by increasing hydration speed, by using fast setting cement [69] or adding accelerator admixtures [6, 7, 26]. However, fast setting cements cannot be used for all applications, especially if the time needed to put in place the material can vary. Therefore, we choose to investigate how the properties of the fresh cement paste itself, as described in part 1.3, can stabilize the cement foam.

1.5 Complex foams and bubble suspensions

We have seen in section 1.3 that a cement paste is a suspension of solid grains and that it behaves as a yield stress fluid. To investigate how this can affect the foam stability, we first focus on granular foams (parts 1.5.1 and 1.5.2), and then on the effect of yield stress (part 1.5.3).

1.5.1 Hydrophobic particles

Ramsden in 1904 [70] and *Pickering* in 1907 [71] studied respectively foams and emulsions containing particles and reported a very good stability. Best stability is achieved when contact angle θ of air-liquid interface on the solid surface is close to 90° (see example on Fig. 1.10).

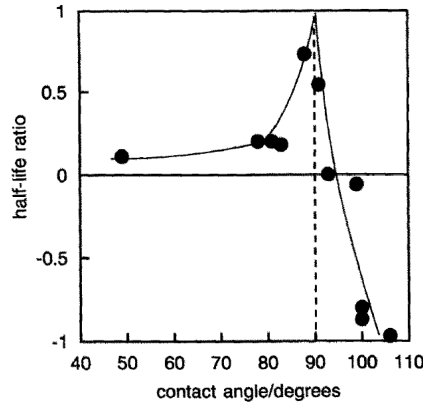


Figure 1.10: Effect of the addition hydrophobised Ballotini beads on the stability of aqueous foam. Half life ratio is $(t_{part} - t_{aq})/t_{aq}$ where t_{part} is the half life duration of the foam with particles and t_{aq} the half life of the aqueous foam. Graph taken from [72]

This remarkable stability is achieved thanks to the adsorption of the particles at air-liquid interface [56, 73, 74]. Note that for partially hydrophobic particle adsorption to occur, the particles must be small enough to be able to diffuse to the interface within the time of the experiment. In addition, adsorption barrier, due for instance to electrostatic repulsion between interface and particle, must be small enough [56]. When these conditions are fulfilled and a spherical particle of radius a reaches the interface, desorption energy is given by [73]:

$$E_{Des} = \gamma a^2 \pi (1 - |\cos\theta|)^2 \quad (1.12)$$

Desorption energy is maximal and equal to $\gamma a^2 \pi$ when $\theta = 90^\circ$, drops to $\gamma a^2 \pi / 4$ when $\theta = 60^\circ$ and is equal to zero for fully hydrophilic ($\theta = 0^\circ$) or fully hydrophobic ($\theta = 180^\circ$) particles.

Let us first mention that experiments have showed that adsorbed spherical particle monolayer can stop the propagation of a hole in the film [75].

Besides, particles tend to prevent the formation of holes in the film. Coalescence is avoided when adsorbed particles in films can stop the reduction of liquid film thickness to zero. The critical pressure which leads to zero film thickness depends on the configuration of the particles in the film. It has been theoretically calculated for a closely packed single layer and double layer of spherical particles [73, 76] (see illustration of configurations in Fig 1.11). For both configurations, calculated critical pressure is higher when $\theta = 0^\circ$ and decreases with contact angle. Film ruptures if (1) particles desorb or (2) film thickness between the adsorbed particles reaches zero. Combination of these two conditions leads to an optimal contact angle for film stability for each configuration: 70° for a single layer of particles and 86° for a double layer [76].

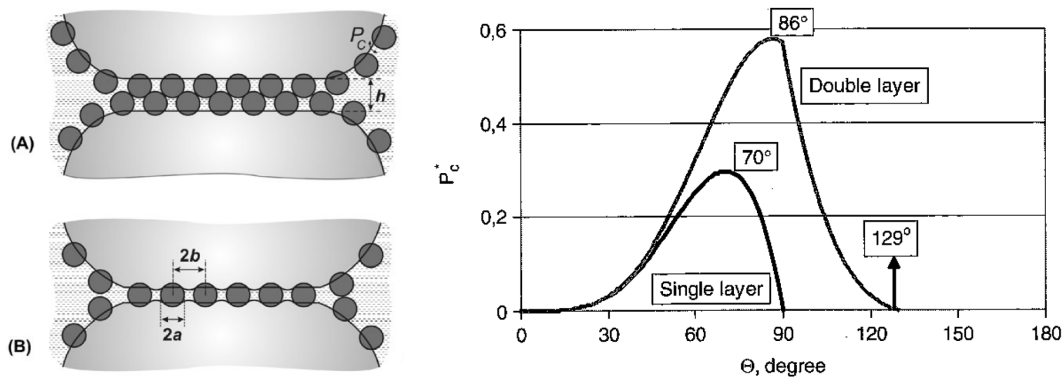


Figure 1.11: Left: illustration of double layer (A) and single layer (B) of particles [56]. Right: Dimensionless pressure leading to film rupture [77]

Several authors have studied foams stabilization with colloidal particles [78, 79, 80], with diameter ranging from several 10 nm to a few 100 nm. Van der Waals and electrostatic attractions between particles lead to the formation of agglomerates in the films which can enhance film stability. One possible explanation is the increase of the critical pressure at which the film thickness is zero due to a 3D organisation of the particles in the films [76, 80]. *Gautier et al.*[78] also observed the stabilization of foams with interfaces weakly covered by particles and suggested that this stability is due to the formation of patches of particles at contact areas between the bubbles.

In addition to reducing the risk of coalescence, adsorbed particles around a bubble can prevent gas dissolution into liquid phase and gas transfer to the neighboring bubbles. Ripening is stopped at one of the two following conditions:

- The overpressure inside the bubbles becomes zero: $P_{gas} - P_{liq} = 0$, or in other words, the macroscopic surface tension of the interface with particles becomes zero [56]. Observations of the shape of the bubbles [81, 82] and numerical simulations [83] showed that when the size of an armored bubble decreases, its shape does not remain spherical, as shown in Fig. 1.12. When the bubble deforms, the shape of the air-liquid interface between the particles also changes: it takes the form of a saddle, with average curvature zero, which, as shown by Laplace's law (equation 1.3), cancels the overpressure [83].

- Decrease of bubble volume leads to a decrease of gas pressure: $dP_{gas}/dR > 0$. This condition is fulfilled when the adsorbed particles form an elastic shell of elastic modulus $E_s = -\Sigma d\gamma/d\Sigma$ with $\Sigma = 2\pi R^2$ and when this elastic modulus fulfills to Gibbs criterion, $E_s > 2\gamma$ [79, 84].

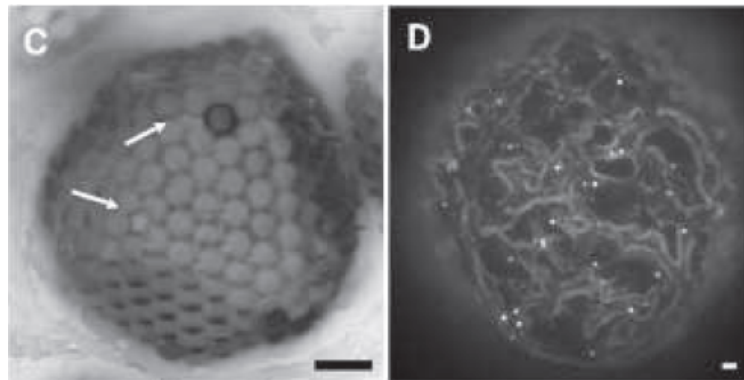


Figure 1.12: Images of deformed armored bubbles at two different particle-bubble size ratio: faceted shape for $a/R = 0.19$ (C) and crumpled shape for $a/R = 0.008$ (D). Scale bars are $8 \mu\text{m}$ long [83].

How can particle adsorption at interfaces be used to prepare cement foams? A solution successfully implemented by *Krämer et al.* [4, 21] is the use of hydrophobized nanosilica particles in the precursor foams. We can also wonder in which conditions cement grains can themselves stabilize the interfaces. It has been shown that adsorption barrier is proportional to the radius of curvature of the edge of the particles [56]. In this extent, cement grains, due to their irregular shape, are good candidates to adsorb at interfaces. In addition, adsorption barrier is reduced when electrolyte concentration is high, which is the case in cement paste interstitial solution. However, using cement grains to stabilize the interfaces requires to make them hydrophobic.

In practice, hydrophobization of solid particles can be achieved by the adsorption of surfactants. The review [85] describes adsorption mechanisms of ionic and non-ionic surfactants on solid surfaces. In the case of ionic surfactant in presence of an oppositely charged solid surface, adsorption takes place in two phases. At low surfactant concentrations, surfactant charged head is oriented to the solid surface, and hydrophobic tail, to the solution (see Fig. 1.13, (b)). In this regime, contact angle θ increases which increasing surfactant concentration until a maximal value. In the second regime, surfactant molecule agglomerate on the solid surface. Hydrophilic heads of adsorbed molecules in the second layer are directed toward the solution; thus, contact angle decreases when surfactant concentration increases (see Fig. 1.13, (c)). Contact angle of the solid particles can therefore be monitored by surfactant concentration.

In the case of cement, adsorption for anionic surfactant is higher than cationic surfactant [48, 86]. When anionic surfactant concentration increases, cement grain contact

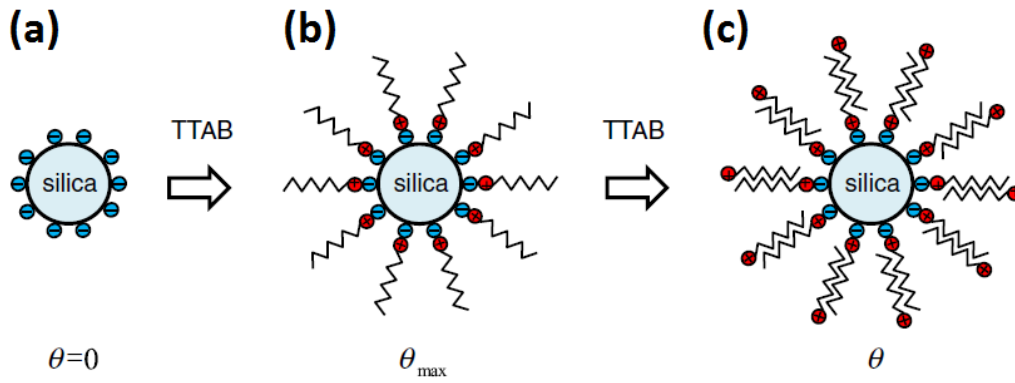


Figure 1.13: Mechanism of cationic surfactant adsorption at the surface of negatively charged silica beads. Blue and red circles represent respectively negative and positive charges [86].

angle increases up to a maximal value and then decreases [48, 86]. *Petit et al.* [86] observed that hydrophobic cement grains do adsorb at the surface of bubbles rising in a cement paste. How they affect foam stability remains to be investigated.

1.5.2 Hydrophilic particles

Hydrophilic particles, i.e. $\theta = 0^\circ$, remain in bulk aqueous solution and do not adsorb at interfaces. Experiments showed that the presence of particles increases the life time of a foam. In particular, they decrease drainage velocity. A small reduction of ripening rate has also been observed, but its was interpreted as a consequence of the higher liquid content in the foam due to the slower drainage [87].

Fig. 1.14 summarizes several experiments where the drainage of model granular foams has been measured. These foams have been prepared from a suspension of hydrophilic beads of uniform size and same density of aqueous phase.

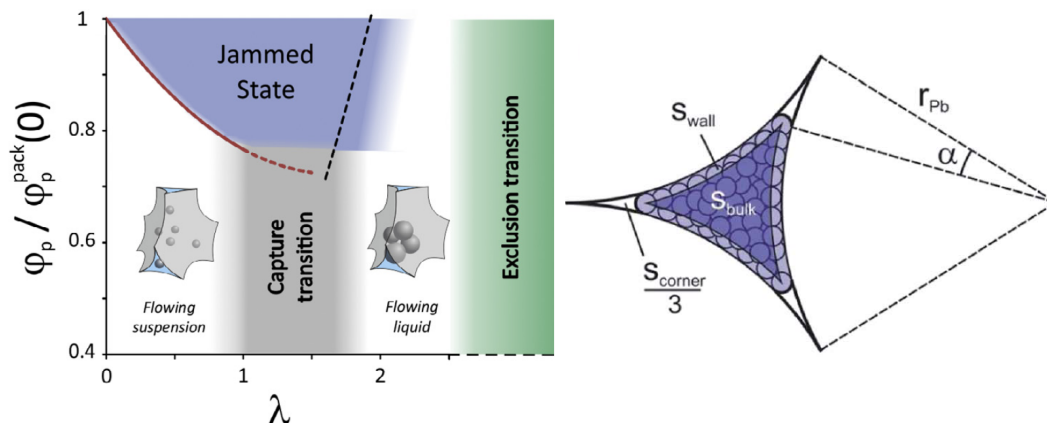


Figure 1.14: Left: Drainage behavior of hydrophilic particle foams. λ is the ratio of the sizes of the particles and of the Plateau borders, ϕ_p the particle volume fraction in the continuous phase and $\phi_p(0)$ its value for $\lambda \rightarrow 0$ [88]. Right: Illustration of sphere packing in a Plateau border section: solid volume fractions in the corners and against the walls are smaller than the bulk volume fraction [89].

Drainage behavior depends on λ , the ratio of the particle size to the Plateau border size r_{PB} , i.e. the radius of the biggest particles which can enter the Plateau borders. Relation of λ with liquid fraction has been obtained by numerical simulations for $0 \lesssim \lambda \lesssim 0.26$ [90]:

$$\lambda = \frac{a}{R_{BP}} = \frac{0.27\sqrt{\Phi_l} + 3.17\Phi_l^{2.75}}{1 + 0.57\Phi_l^{0.27}} \quad (1.13)$$

When $\lambda \lesssim 1$, the particles are not individually stuck in the foams. Therefore, particles can flow in the Plateau borders and nodes together with the liquid. The drainage velocity decreases when particle volume fraction increases and is stopped when Φ_p reaches a critical value Φ_p^{crit} which decreases when size ratio λ increases. For a given λ , effect of particle fraction on suspension viscosity μ can be fitted with a Krieger-Dougherty law:

$$\mu(\Phi_p) = \mu_{liq} \left(1 - \frac{\Phi_p}{\Phi_p^{crit}} \right)^{-2.5\Phi_p^{crit}} \quad (1.14)$$

where μ_{liq} is the viscosity of the liquid phase of the suspension. Dependence of Φ_p^{crit} on λ is a consequence of the specific shape of the Plateau borders and nodes in the foam. As illustrated by the schema on the right of Fig. 1.14, the beads cannot fill the whole volume. Excluded volume, in the corners and near the walls, increases with increasing bead size.

Stopping drainage with hydrophilic particles is facilitated when particles size increases up to $\lambda \sim 1$. However, when λ exceeds 1, the particles remain stuck in the nodes, and the liquid is free to move between the bubbles and the particles. Thus, drainage rate increases again [91].

This study on a model solid suspensions highlights the major effect of particle critical packing fraction. Critical packing fraction is expected to be affected by the particle shape, the surface properties and distribution. To implement drainage arrest with cement grains, the main issue would be to identify critical packing fraction and how it is affected by bubble size. A decrease of drainage rate caused by confinement has already be reported in foams containing coal fly ash particles [87] and clay nanoparticles [92].

Foams containing colloidal particles have also been investigated [93]. In this case however, the authors suggest that drainage stabilization is due to the presence of a yield stress in the colloidal suspension. Let us now focus on this point.

1.5.3 Yield stress fluid

As already mentioned, yield stress fluids do not flow when the stress they undergo is below the yield stress. Therefore, to understand how the yield stress can stabilize the foam, yield stress must be compared with the yield stress at stake during destabilization.

Regarding ripening, as we have seen in paragraph 1.4.4.3, destabilization is driven by capillary pressure. Thus, ripening of a foamy yield stress fluid should stop if yield stress is the same order of magnitude as the capillary pressure difference between the bubbles. The critical yield stress to stop ripening is therefore [94]:

$$\tau_{c,r} \sim \frac{\gamma}{R} \quad (1.15)$$

To estimate the stresses leading to drainage, authors have compared the Plateau borders and nodes to a porous medium whose pore size can be estimated by r_{PB} . Drainage is expected to stop when the yield stress reaches a critical value [93, 94]:

$$\tau_{c,d} \sim \rho g r_{PB} \quad (1.16)$$

where ρ is the density of the continuous phase. Drainage prevention due to yield stress has been experimentally observed by *Goyon et al.*[95], who have successfully created foams with constant air volume fraction (71%) over the sample height, stable for several hours (ripening was stopped by using low-solubility gas).

In addition, the presence of a yield stress makes the existence of bubble suspensions possible, with a stability of several hours. Indeed, bubble cannot rise if the buoyancy force $F_{buoyancy} = 4/3\rho g\pi R^3$ is compensated by the drag force due to suspending fluid yield stress $F_{drag} = C_d\tau_y\pi R^2$. C_d is a coefficient which depends on the geometry of the moving object and on the surface properties. The minimum yield stress to avoid bubble rising is therefore:

$$\tau_{c,buoyancy} = \frac{4R\rho g}{3C_d} \quad (1.17)$$

The value measured for a smooth sphere is $C_d = 6.7$ [96]. With $\rho \approx 2000 \text{ kg/m}^3$ for cement paste, calculated values are $\tau_{c,buoyancy} \approx 4 \text{ Pa}$ if $R = 1 \text{ mm}$ and $\tau_{c,buoyancy} \approx 0.04 \text{ Pa}$ if $R = 10 \text{ }\mu\text{m}$.

Therefore, the presence of a yield stress in cement paste, mortar or concrete explains why cement foams described in the literature can possess air content as low as 10% or 20% and still be stable.

1.5.4 Rheology of complex foams and bubble suspensions

Rheological behavior of foams described in part 1.4.5 is strongly affected by the rheological properties of the continuous phase.

1.5.4.1 Aerated yield stress fluids

The elastic modulus and the yield stress of aerated yield stress fluids have been studied both in the case of high air content (85 to 95%) and low air content (below 50%). Measurements and model of the reduced elastic modulus (i.e. normalized by the elastic modulus of the continuous phase G'_{int}) are shown in Fig. 1.15.

At given volume fraction, reduced elastic modulus depends on the elastic capillary number Ca_{el} , which accounts for the deformability of the bubbles compared to the surrounding continuous phase and is defined by¹:

¹Note that in reference [99] related to bubble suspensions, definition of elastic modulus differs from this definition by a factor 2: $Ca_{el} = RG'_0/(2\gamma)$.

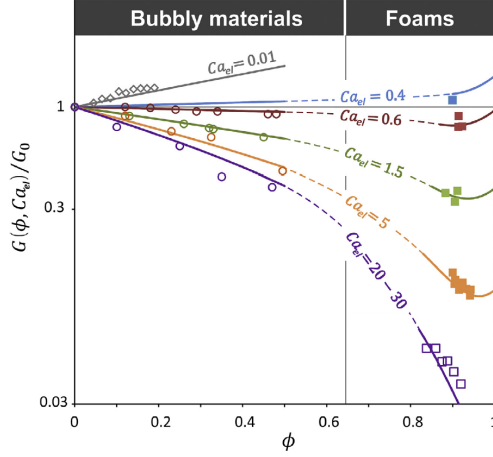


Figure 1.15: Elastic modulus of aerated yield stress fluids, normalized by the elastic modulus of the continuous phase, as a function of the volume fraction of the dispersed phase. Graph reproduced from [97]; it summarizes data from [97] for emulsion foams (filled squares), from [98] for gelatine foams (empty squares), from [99] for bubbles suspensions in emulsions (circles) and from [100] for liquid droplet in silicone gel (empty diamonds).

$$Ca_{el} = \frac{RG'_{int}}{\gamma} \quad (1.18)$$

At low air content, measurements of bubble suspension elastic modulus fit well with a theoretical prediction from [101]. The suspension elastic modulus decreases when air volume fraction increases for deformable bubbles, i.e. for large values of bubble radius or continuous phase elasticity, so that $Ca_{el} > 1/2$ [99]. When bubbles are non-deformable $Ca_{el} < 1/2$, suspension elastic modulus is expected to increase with air content. This effect has not been experimentally measured with bubbles but has been observed with small drops [100].

At high air content, macroscopic elasticity is a sum of the contribution of the bubbles G'_{aq} (see equation 1.9), the contribution of the elasticity of the interstitial fluid G'_{sk} and a coupling term ψ [97]. The contribution of the interstitial fluid G'_{sk} is given by *Gibson and Ashby* relation [102]:

$$G'_{sk} \approx G'_{int}(1 - \Phi)^2 \quad (1.19)$$

The coupling term ψ accounts for the deformation of bubbles due to embedding elastic fluid. An empirical relation has been proposed by [97] as a function of elastic capillary number and air fraction. $\psi \rightarrow 0$ when $\Phi \rightarrow 0$, i.e. when the volume of the suspending fluid is very low. In fact, when air fraction is very high, yield stress fluid foam behaves like a dry aqueous foam. $\psi/G'_{int} \rightarrow 0$ for large values of G'_{int} , that is to say that when the contribution of the capillary effect becomes negligible compared to interstitial elasticity, the contribution of the skeleton G'_{sk} is the main term, like in solid foams.

Yield stress of aerated yield stress fluids has also raised attention. It is affected by the

Bingham capillary number, defined by²:

$$Ca_y = \frac{R\tau_{y,int}}{\gamma} \quad (1.20)$$

For low air content $\Phi < 50\%$, behavior of indeformable bubbles ($Ca_y \rightarrow 0$) and fully deformable bubble ($Ca_y \rightarrow \infty$) have both been determined theoretically [101] as a function of the air content. The curves have been obtained experimentally in oil-in-water emulsion, respectively for $Ca_y \lesssim 0.22$ and $Ca_y = 1.1$ [99]. Theoretical curves and experimental points are shown in Fig. 1.16. Non-deformable bubbles hardly change the yield stress of the suspension for air fractions up to 50%, whereas in the case of deformable bubbles, yield stress decreases when air volume content increases.

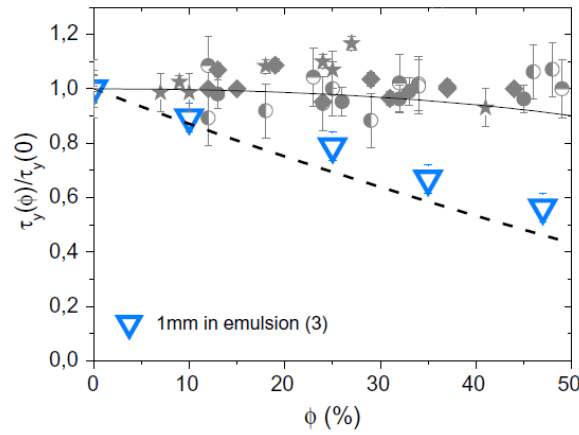


Figure 1.16: Yield stress of bubble suspensions in yield stress fluids. Measurements for $Ca_y \lesssim 0.22$ (grey points) and $Ca_y = 1.1$ (blue triangles) and theoretical curves for $Ca_y \rightarrow 0$ (solid line) and $Ca_y \rightarrow \infty$ (dotted line) [99].

In the foam regime, i.e. at high air content, macroscopic yield stress is related to Bingham capillary number and to air fraction by the following empirical relation [97]:

$$\frac{\tau_{y,foam}(\Phi)}{\tau_{y,aq}(\Phi)} = 1 + c(1 - \Phi)^{4/3} Ca_y^{2/3} \quad (1.21)$$

where $c = 110$ is a fitting parameter.

1.5.4.2 Granular foams

The case of granular foams containing hydrophilic particles has also been investigated. Elastic modulus and yield stress were measured after drainage of the foams. In particular, in the case of small particles ($\lambda < 1$), particle volume fraction in the continuous phase is equal to the maximal packing fraction $\phi_p = \phi_p^{crit}$. Size effects, described in part 1.5.2 on the drainage of granular foams, have a notable consequence on the rheological properties of the foams [63]. When the particle size a is much bigger than the bubble size, aqueous foam behaves like a continuous medium at the scale of the particles [63, 68]. As

²Definition used in [99] is $Ca_y = R\tau_{y,int}/(2\gamma)$.

a consequence, the granular foam rheological properties fit well with the properties of a yield stress fluid (i.e. the aqueous foam) reinforced by particles. On the other hand, when $\lambda \ll 1$, the small particles stuck in the Plateau borders and nodes can be considered as a continuous granular structure [68, 103]. As λ increases between those two asymptotic behaviors, the number of particles in the Plateau border decreases and reaches zero when $\lambda \approx 1$. Illustration of the particle configurations for increasing values of λ are shown in Fig 1.17.

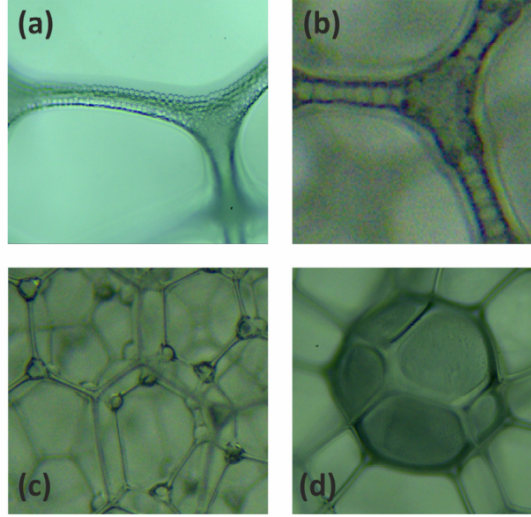


Figure 1.17: Images of granular foams for $R = 225 \mu\text{m}$ and increasing particle radius. (a) $a = 5 \mu\text{m}$, (b) strings of particles $a = 20 \mu\text{m}$, (c) isolated particles in foam nodes $a = 40 \mu\text{m}$, and (d) isolated large particles embedded in foam $a = 250 \mu\text{m}$ [63].

At given particle and air volume fractions, the biggest values of elastic modulus and yield stress are obtained for the small particles. Let us deal now with this small particle regime. Elastic modulus and yield stress curve do not depend on particle size as long as $a/R \lesssim 0.05$ [68, 103]. They are given by the same equations as yield stress fluid foams. Elasticity and yield stress of the granular phase are obtained as the only fitting parameters in equations 1.19 and 1.21, their respective values are $G'_{int} = 150 \text{ kPa}$ [103] and $\tau_{y,int} = 120 \text{ Pa}$ [68]. Note that coupling term was not taken into account for the calculation of G'_{int} , but it is expected to be negligible at this high value of the interstitial elastic modulus. These values of the interstitial elasticity and yield stress correspond to a dense granular material under confinement pressure 400 Pa , which is the order of magnitude of the pressure exerted by the bubbles on the continuous phase in the reported studies [63, 68, 103].

This analysis of the behavior of complex foams shows that, in the case of cement foams, interstitial cement paste is expected to strongly improve the stability of the foam compared to aqueous foam. Indeed, drainage is strongly reduced in the presence of yield stress or hydrophilic particles. Regarding coalescence, a proper choice of surfactant or the use of hydrophobic particles is required. Lastly, ripening can be stopped by the presence of yield stress or hydrophobic particles. Besides, cement paste rheological properties and

particle content is promising to increase the yield stress and elastic modulus of the foams. In addition, thanks to cement paste yield stress, aerated materials can be prepared with small air fractions.

1.6 Conclusion

Cement foams properties are mainly related to their density, but also to their formulation and preparation protocol. To study how they are affected by pore configuration, cement foams with well controlled morphological properties must be produced. Mixing well controlled precursor foam with cement paste seems to be a promising manufacturing method. However, the structure of fresh cement foam is endangered by three destabilization mechanisms, encountered in all liquid foams: drainage because of gravity, Ostwald ripening due to pressure differences between the bubbles, and coalescence when a liquid film ruptures. Comparison of studies on liquid and complex foams shows that cement paste characteristics offer promising hints to stop or slow down destabilization.

First, the presence of a high interstitial yield stress in foams can stop drainage and ripening. The interstitial yield stress is expected to depend on the water-to-cement ratio. Similarly to concrete admixtures, surfactant adsorption on cement grains is expected to modify the yield stress. This effect is the subject of chapter 2.

Second, particles have a strong effect on foam stability. Hydrophilic particles can slow down and stop drainage. Hydrophobic particles, on the other hand, adsorb at interfaces and can avoid ripening and coalescence. For the implementation of cement particles as stabilizers, we therefore have to monitor cement grain surface properties by choosing adequate surfactant and concentration. We will discuss this aspect in chapters 4 and 5.

We have reviewed literature studies about the rheology of aqueous and complex foams. They show that yield stress and elastic modulus of aerated yield stress fluid or particle foams depend on the rheological properties of the continuous phase and on the characteristics of the bubbles (size, volume fraction and surface tension). This analysis will be used in the following chapters for two points. In chapter 3, we will compare the measured yield stress of aerated cement pastes, prepared with two different surfactants, with yield stress of a model aerated yield stress fluid. In chapter 4, rheological measurement of fresh cement foams will be used to assess the properties of the interstitial cement paste.

Bibliography

- [1] A. Just and B. Middendorf, "Microstructure of high-strength foam concrete," *Materials Characterization*, vol. 60, pp. 741–748, 2009. 5, 7
- [2] X. Qu and X. Zhao, "Previous and present investigations on the components, microstructure and main properties of autoclaved aerated concrete - a review," *Construction and Building Materials*, vol. 135, pp. 505–516, 2017. 5, 6

- [3] N. Narayanan and K. Ramamurthy, "Structure and properties of aerated concrete: a review," *Cement & Concrete Composites*, vol. 22, pp. 321–329, 2000. [5](#), [8](#)
- [4] C. Kramer, M. Schauerte, T. Kowald, and R. Trettin, "Three-phase-foams for foam concrete application," *Materials Characterization*, vol. 102, pp. 173–179, 2015. [5](#), [23](#)
- [5] S. I. Al-Noury, W. H. Mirza, and S. Huq, "Density and strength characteristics of lightweight mortar," *Cement & Concrete Composites*, vol. 12, 1990. [5](#)
- [6] Z. Pan, H. Li, and W. Liu, "Preparation and characterization of super low density foamed concrete from Portland cement and admixtures," *Construction and Building Materials*, vol. 72, pp. 256–261, 2014. [5](#), [20](#)
- [7] Z. Huang, T. Zhang, and Z. Wen, "Proportioning and characterization of Portland cement-based ultra-lightweight foam concretes," *Construction and Building Materials*, vol. 79, pp. 390–396, 2015. [5](#), [7](#), [8](#), [20](#)
- [8] L. Du and K. Folliard, "Mechanisms of air-entrainment in concrete," *Cement and Concrete Research*, vol. 35, pp. 1463–1471, 2005. [5](#), [13](#)
- [9] M. Kilgys, A. Laukaitis, M. Sinica, and G. Sezemanas, "The influence of some surfactants on porous concrete properties," *Materials science*, vol. 13, no. 4, pp. 310–316, 2007. [5](#), [13](#)
- [10] H. Atahan, J. C. Carlos, S. Chae, P. Monteiro, and J. Bastacky, "The morphology of entrained air voids in hardened cement paste generated with different anionic surfactants," *Cement & Concrete Composites*, vol. 30, pp. 566–575, 2008. [5](#), [13](#)
- [11] F. Akthar and J. Evans, "High porosity (<90%) cementitious foams," *Cement and Concrete Research*, vol. 40, pp. 352–358, 2010. [5](#), [6](#)
- [12] H. Weigler and S. Karl, "Structural lightweight aggregate concrete with reduced density - lightweight aggregate foamed concrete," *The International Journal of Lightweight Concrete*, vol. 2, no. 2, pp. 101–104, 1980. [5](#), [6](#), [7](#), [13](#)
- [13] E. Kunhanandan Nambiar and K. Ramamurthy, "Influence of filler type on the properties of foam concrete," *Cement & Concrete Composites*, vol. 28, pp. 475–480, 2006. [6](#), [7](#)
- [14] M. Jones and A. McCarthy, "Utilising unprocessed low-lime coal fly ash in foamed concrete," *Fuel*, vol. 84, pp. 1398–1409, 2005. [6](#), [7](#)
- [15] A. Hilal, N. Thom, and A. Dawson, "On entrained pore size distribution of foamed concrete," *Construction and Building Materials*, vol. 75, pp. 227–233, 2015. [6](#)
- [16] R. Rixom and N. Mailvaganam, *Chemical Admixtures for Concrete*. E. & F.N. Spon Ltd, 3rd ed. ed., 1999. p106+. [6](#), [8](#), [13](#)

- [17] T. D. Tonyan and L. J. Gibson, "Structure and mechanics of cement foams," *Journal of Material Science*, vol. 27, pp. 6371–6378, 1992. 6, 7
- [18] A. M. Abd and S. M. Abd, "Modelling the strength of lightweight foamed concrete using support vector machine (svm)," *Case Studies in Construction Materials*, vol. 6, pp. 8–15, 2017. 6, 7
- [19] D. Falliano, D. De Domenico, G. Ricciardi, and E. Gugliandolo, "Experimental investigation on the compressive strength of foamed concrete: Effect of curing conditions, cement type, foaming agent and dry density," *Construction and Building Materials*, vol. 165, pp. 735–749, 2018. 6, 7
- [20] G. Yakovlev, J. Keriene, A. Gailius, and I. Girniene, "Cement based foam concrete reinforced by carbon nanotubes," *Materials science*, vol. 12, no. 2, pp. 147–151, 2006. 6
- [21] C. Krämer, M. Schauerte, T. Müller, S. Gebhard, and R. Trettin, "Application of reinforced three-phase-foams in UHPC foam concrete," *Construction and Building Materials*, vol. 131, pp. 746–757, 2017. 6, 23
- [22] G. Hoff, "Porosity-strength considerations for cellular concrete," *Cement and Concrete Research*, vol. 2, pp. 91–100, 1972. 7
- [23] E. P. Kearsley and P. J. Wainwright, "The effect of porosity on the strength of foamed concrete," *Cement and Concrete Research*, vol. 32, pp. 233–239, 2002. 7
- [24] K. Ramamurthy, E. Kunhanandan Nambiar, and G. Indu Siva Ranjani, "A classification of studies on properties of foam concrete," *Cement & Concrete Composites*, vol. 31, pp. 388–396, 2009. 7
- [25] A. Hajimohammadi, T. Ngo, and P. Mendis, "Enhancing the strength of pre-made foams for foam concrete applications," *Cement and Concrete Composites*, vol. 87, pp. 164–171, 2018. 7
- [26] J. Jiang, Z. Lu, Y. Niu, J. Li, and D. Zhang, "Study on the preparation and properties of high-porosity foamed concretes based on ordinary Portland cement," *Materials and Design*, 2015. 7, 20
- [27] G. Samson, *Synthèse et propriétés des mousses minérales*. PhD thesis, INSA de Rennes, 2015. 7
- [28] O. Hussein, S. A. Bernal, and J. L. Provis, "Bubble stabilisation improves strength of lightweight mortars," *37th Cement and Concrete Science Conference*, 2017. 7
- [29] G. Samson, A. Phelipot-Mardelé, and C. Lanos, "A review of thermomechanical properties of lightweight concrete," *Magazine of Concrete Research*, vol. 69, no. 4, pp. 201–216, 2016. 7, 8

- [30] G. Samson, M. Cyr, and X. X. Gao, “Thermomechanical performance of blended metakaolin - GGBS alkali-activated foam concrete,” *Construction and Building Materials*, vol. 157, pp. 982–993, 2017. [8](#)
- [31] P.-C. Aïtcin, “Entrained air in concrete: rheology and freezing resistance,” in *Science and Technology of Concrete Admixtures* (P.-C. Aïtcin and R. J. Flatt, eds.), pp. 87–95, Woodhead publishing, 2016. [8](#)
- [32] R. M. Ahmed, N. E. Takach, U. M. Khan, S. Taoutaou, S. James, A. Saasen, and R. Godoy, “Rheology of foamed cement,” *Cement and Concrete Research*, vol. 39, pp. 353–361, 2009. [8](#)
- [33] P. Aïtcin, “Phenomenology of cement hydration,” in *Science and technology of concrete admixtures* (P. Aïtcin and R. Flatt, eds.), pp. 15–25, Woodhead Publishing, 2016. [9](#)
- [34] N. Roussel, A. Lemaître, R. J. Flatt., and P. Coussot, “Steady state flow of cement suspensions: A micromechanical state of the art.,” *Cement and Concrete Research*, vol. 40, pp. 77–84, 2010. [9](#), [10](#)
- [35] N. Roussel, G. Ovarlez, S. Garrault, and C. Brumaud, “The origins of thixotropy in fresh cement pastes,” *Cement and Concrete Research*, vol. 42, pp. 148–157, 2012. [9](#), [11](#), [12](#)
- [36] F. Mahaut, S. Mokéddem, X. Chateau, N. Roussel, and G. Ovarlez, “Effect of coarse particle volume fraction on the yield stress and thixotropy of cementitious materials,” *Cement and Concrete Research*, vol. 38, pp. 1276–1285, 2008. [9](#), [11](#)
- [37] P. Coussot, *Rhéophysique - La matière dans tous ses états*. EDP Sciences/CNRS Editions, 2012. [10](#), [11](#)
- [38] R. J. Flatt and P. Bowen, “Yodel: a yield stress model for suspensions,” *Journal of the American Ceramic Society*, vol. 89, no. 4, pp. 1244–1256, 2006. [10](#)
- [39] R. J. Flatt and I. Schober, “Superplasticizer and the rheology of concrete,” in *Understanding the rheology of concrete* (N. Roussel, ed.), pp. 144–208, Woodhead publishing, 2012. [10](#)
- [40] N. Roussel, “A thixotropy model for fresh fluid concretes: Theory, validation and applications,” *Cement and Concrete Research*, vol. 36, pp. 1797–1806, 2006. [10](#)
- [41] O. H. Wallevik, D. Feys, J. E. Wallevik, and K. H. Khayat, “Avoiding inaccurate interpretations of rheological measurements for cement-based materials,” *Cement and Concrete Research*, vol. 78, pp. 100–109, 2015. [10](#), [11](#)
- [42] J. E. Wallevik, “Thixotropic investigation on cement paste: Experimental and numerical approach,” *Journal of Non-Newtonian Fluid Mechanics*, vol. 132, pp. 86–99, 2005. [11](#)

- [43] G. Gelardi, S. Mantellato, D. Marchon, M. Palacios, A. Eberhardt, and R. J. Flatt, “Chemistry of chemical admixtures,” in *Science and Technology of Concrete Admixtures* (P.-C. Aïtcin and R. J. Flatt, eds.), pp. 149–218, Woodhead publishing, 2016. [12](#), [13](#)
- [44] D. Marchon and R. J. Flatt, “Impact of chemical admixtures on cement hydration,” in *Science and Technology of Concrete Admixtures* (P.-C. Aïtcin and R. J. Flatt, eds.), pp. 414–432, Woodhead publishing, 2016. [12](#)
- [45] C. Jolicoeur, T. To, T. Nguyen, R. Hill, and M. Pagé, “Mode of action of anionic surfactants for air entrainment in cement pastes w-w/o fly ash,” in *2009 World of Coal Ash (WOCA) Conference - May 4-7, 2009 in Lexington, KY, USA*, 2009. [13](#)
- [46] E. P. Kearsley and P. J. Wainwright, “The effect of high fly ash content on the compressive strength of foamed concrete,” *Cement and Concrete Research*, vol. 31, pp. 105–112, 2001. [13](#)
- [47] H. Uchikawa, S. Hanehara, T. Shirasaka, and D. Sawaki, “Effect of admixture on hydration of cement, adsorptive behavior of admixture and fluidity and setting of fresh cement paste,” *Cement and Concrete Research*, vol. 22, pp. 1115–1129, 1992. [13](#)
- [48] T. Zhang, S. Shang, F. Yin, A. Aishah, A. Salmiah, and T. Ooi, “Adsorptive behavior of surfactants on surface of Portland cement,” *Cement and Concrete Research*, vol. 31, pp. 1009–1015, 2001. [13](#), [23](#), [24](#)
- [49] P. J. Andersen, “The effect of superplasticizers and air-entraining agents on the zeta potential of cement particles,” *Cement and Concrete Research*, vol. 16, pp. 931–940, 1986. [13](#)
- [50] E. Gueit, E. Darque-Ceretti, P. Tintiller, and M. Horgnies, “Influence de tensioactifs sur l’hydratation du ciment à l’interface béton-coffrage,” in *Matériaux 2010*, 2010. [13](#)
- [51] S. Wei, Z. Yunsheng, and M. Jones, “Using the ultrasonic wave transmission method to study the setting behavior of foamed concrete,” *Construction and Building Materials*, vol. 51, pp. 62–74, 2014. [13](#)
- [52] E. Kuzielová, L. Pach, and M. Palou, “Effect of activated foaming agent on the foam concrete properties,” *Construction and Building Materials*, vol. 125, pp. 998–1004, 2016. [13](#)
- [53] I. Cantat, S. Cohen-Addad, F. Elias, F. Graner, R. Höhler, O. Pitois, F. Rouyer, and A. Saint-Jalmes, *Foams - Structure and dynamics*. Oxford University Press, 2013. [14](#), [15](#), [16](#), [17](#), [18](#), [20](#)
- [54] P. Stevenson, ed., *Foam Engineering: Fundamentals and Applications*. John Wiley & Sons, 2012. [14](#)

- [55] B. Cabane and S. Hénon, *Liquides - Solutions, dispersions, émulsions, gels*. Belin, 2007. [14](#)
- [56] S. Tcholakova, N. D. Denkov, and A. Lips, “Comparison of solid particles, globular proteins and surfactants as emulsifiers,” *Physical Chemistry Chemical Physics*, vol. 10, pp. 1608–1627, 2008. [15](#), [19](#), [21](#), [22](#), [23](#)
- [57] A. Saint-Jalmes, “Physical chemistry in foam drainage and coarsening,” *Soft Matter*, vol. 2, pp. 836–849, 2006. [18](#), [19](#)
- [58] A.-L. Biance, A. Delbos, and O. Pitois, “How topological rearrangements and liquid fraction control liquid foam stability,” *Physical Review Letters*, vol. 106, p. 068301, 2011. [18](#)
- [59] O. Pitois, “Foam ripening,” in *Foam Engineering: Fundamentals and Applications* (P. Stevenson, ed.), pp. 59–73, John Wiley & Sons, 2012. [19](#)
- [60] A. Saint-Jalmes and J. Durian, “Vanishing elasticity for wet foams: Equivalence with emulsions and role of polydispersity,” *Journal of Rheology*, vol. 43, p. 1411, 1999. [19](#), [20](#)
- [61] S. Cohen-Addad and R. Höhler, “Rheology of foams and highly concentrated emulsions,” *Current opinion in Colloid & Interface Science*, vol. 19, pp. 536–548, 2014. [19](#), [20](#)
- [62] T. G. Mason, J. Bibette, and D. A. Weitz, “Elasticity of compressed emulsions,” *Physical Review Letters*, vol. 75, no. 10, pp. 2051–2054, 1995. [20](#)
- [63] F. Gorlier, Y. Khidas, and O. Pitois, “Elasticity of particle-loaded liquid foams,” *Soft Matter*, vol. 13, pp. 4533–4540, 2017. [20](#), [28](#), [29](#)
- [64] T. G. Mason, J. Bibette, and D. A. Weitz, “Yielding and flow of monodisperse emulsions,” *Journal of Colloid and Interface Science*, vol. 179, pp. 439–448, 1996. [20](#)
- [65] H. M. Princen and A. D. Kiss, “Rheology of foams and highly concentrated emulsions. iv an experimental study of the shear viscosity and yield stress,” *Journal of Colloid and Interface Science*, vol. 128, no. 1, pp. 176–186, 1989. [20](#)
- [66] N. D. Denkov, S. Tcholakova, K. Golemanov, K. P. Ananthapadmanabhan, and A. Lips, “Viscous friction in foams and concentrated emulsions under steady shear,” *Physical Review Letter*, vol. 100, p. 138301, 2008. [20](#)
- [67] S. Tcholakova, N. D. Denkov, K. Golemanov, K. P. Ananthapadmanabhan, and A. Lips, “Theoretical model of viscous friction inside steadily sheared foams and concentrated emulsions,” *Physical Review E*, vol. 78, p. 011405, 2008. [20](#)
- [68] F. Gorlier, Y. Khidas, and O. Pitois, “Yielding of complex liquid foams,” *Journal of Rheology*, vol. 61, pp. 919–930, 2017. [20](#), [28](#), [29](#)

- [69] G. Sang, Y. Zhu, G. Yang, and H. Zhang, "Preparation and characterization of high porosity cement-based foam material," *Construction and Building Materials*, vol. 91, pp. 133–137, 2015. [20](#)
- [70] W. Ramsden, "Separation of solids in the surface-layers of solutions and 'suspensions' - preliminary account," *Proceedings of the Royal Society of London*, vol. 72, pp. 156–164, 1904. [21](#)
- [71] S. U. Pickering, "Emulsions," *Journal of Chemical Society*, vol. 91, pp. 2001–2021, 1907. [21](#)
- [72] R. Aveyard, B. P. Binks, P. D. I. Fletcher, T. G. Peck, and C. E. Rutherford, "Aspects of aqueous foams stability in the presence of hydrocarbon oils and solid particles," *Advances in Colloid and Interface Science*, vol. 48, pp. 93–120, 1994. [21](#)
- [73] N. D. Denkov, I. B. Ivanov, and P. A. Kralchevski, "A possible mechanism of stabilization of emulsions by solid particles," *Journal of Colloids and Interface Science*, vol. 150, no. 2, pp. 589–593, 1992. [21](#), [22](#)
- [74] B. P. Binks, "Particles as surfactants - similarities and differences," *Current Opinion in Colloid & Interface Science*, vol. 7, pp. 21–41, 2002. [21](#)
- [75] Y. Timounay, E. Lorenceau, and F. Rouyer, "Opening and retraction of particulate soap films," *EPL - Europhysics Letters*, vol. 111, no. 2, 2015. [21](#)
- [76] G. Kaptay, "On the equation of the maximum capillary pressure induced by solid particles to stabilize emulsions and foams and on the emulsion stability diagrams," *Colloids and Surfaces A*, vol. 282-283, pp. 387–401, 2006. [22](#)
- [77] G. Kaptay and N. Babcsán, "Particle stabilized foams," in *Foam Engineering: Fundamentals and Applications* (P. Stevenson, ed.), pp. 121–143, John Wiley & Sons, 2012. [22](#)
- [78] F. Gautier, M. Destribats, R. Perrier-Cornet, J. Dechézelles, J. Giermanska, V. Héroguez, S. Ravaine, F. Leal-Calderon, and V. Schmitt, "Pickering emulsions with stimuable particles: from highly- to weakly-covered interfaces," *Physical Chemistry Chemical Physics*, vol. 9, no. 48, pp. 6455–6462, 2007. [22](#)
- [79] A. Stocco, E. Rio, B. Binks, and D. Langevin, "Aqueous foams stabilized solely by particles," *Soft Matter*, vol. 7, no. 4, pp. 1260–1267, 2011. [22](#), [23](#)
- [80] Z. A. Al Yousef, M. A. Almobarky, and D. S. Schechter, "The effect of particle aggregation on surfactant foam stability," *Journal of Colloid and Interface Science*, vol. 511, pp. 365–373, 2018. [22](#)
- [81] O. Pitois, M. Buisson, and X. Chateau, "On the collapse pressure of armored bubbles and drops," *European Physical Journal E*, vol. 38, p. 48, 2015. [22](#)

- [82] N. Taccoen, F. Lequeux, D. Z. Gunes, and C. N. Baroud, “Probing the mechanical strength of an armored bubble and its implication to particle-stabilized foams,” *Physical Review X*, vol. 6, no. 1, p. 011010, 2016. [22](#)
- [83] M. Abkarian, A. B. Subramaniam, S.-H. Kim, R. Larsen, S.-M. Yang, , and H. A. Stone, “Dissolution arrest and stability of armored bubbles,” *Physical Review Letters*, vol. 99, p. 188301, 2006. [22](#), [23](#)
- [84] A. Cervantes Martinez, E. Rio, G. Delon, A. Saint-Jalmes, D. Langevin, and B. Binks, “On the origin of the remarkable stability of aqueous foams stabilised by nanoparticles: link with microscopic surface properties,” *Soft Matter*, vol. 4, pp. 1531–1535, 2008. [23](#)
- [85] S. Paria and K. Khilar, “A review on experimental studies of surfactant adsorption at the hydrophilic solid-water interface,” *Advances in Colloid and Interface Science*, vol. 110, no. 3, pp. 75–95, 2004. [23](#)
- [86] P. Petit, I. Javierre, P.-H. Jézéquel, and A.-L. Biance, “Generation and stability of bubbles in a cement based slurry,” *Cement and Concrete Research*, vol. 60, pp. 37–44, 2014. [23](#), [24](#)
- [87] A. Britan, M. Liverts, G. Ben-Dor, S. Koehler, and N. Bennani, “The effect of fine particles on the drainage and coarsening of foam,” *Colloids and Surfaces A*, vol. 344, pp. 15–23, 2009. [24](#), [25](#)
- [88] B. Haffner, Y. Khidas, and O. Pitois, “The drainage of foamy granular suspensions,” *Journal of Colloid and Interface Science*, vol. 458, pp. 200–208, 2015. [24](#)
- [89] B. Haffner, Y. Khidas, and O. Pitois, “Flow and jamming of granular suspensions in foams,” *Soft Matter*, vol. 10, pp. 3277–3283, 2014. [24](#)
- [90] N. Louvet, R. Höhler, and O. Pitois, “Capture of particles in soft porous media,” *Physical Review E*, vol. 82, p. 041405, 2010. [25](#)
- [91] Y. Khidas, B. Haffner, and O. Pitois, “Capture-induced transition in foamy suspensions,” *Soft Matter*, vol. 10, pp. 4137–4141, 2014. [25](#)
- [92] R. Guillermic, A. Salonen, J. Emile, and A. Saint-Jalmes, “Surfactant foams doped with laponite: unusual behaviors induced by aging and confinement,” *Soft Matter*, vol. 5, pp. 4975–4982, 2009. [25](#)
- [93] S. Guignot, S. Faure, M. Vignes-Adler, and O. Pitois, “Liquid and particles retention in foamed suspensions,” *Chemical Engineering Science*, vol. 65, pp. 2579–2585, 2010. [25](#), [26](#)
- [94] I. Lesov, S. Tcholakova, and N. Denkov, “Factors controlling the formation and stability of foams used as precursors of porous materials,” *Journal of Colloid and Interface Science*, vol. 426, pp. 9–21, 2014. [25](#), [26](#)

- [95] J. Goyon, F. Bertrand, O. Pitois, and G. Ovarlez, “Shear induced drainage in foamy yield-stress fluids,” *Physical Review Letters*, vol. 104, p. 128301, 2010. [26](#)
- [96] L. Jossic and A. Magnin, “Drag and stability of objects in a yield stress fluid,” *AIChE Journal*, vol. 47, no. 12, pp. 2666–2672, 2001. [26](#)
- [97] F. Gorlier, Y. Khidas, and O. Pitois, “Coupled elasticity in soft solid foams,” *Journal of Colloid and Interface Science*, vol. 501, pp. 103–111, 2017. [27](#), [28](#)
- [98] Y. Khidas, B. Haffner, and O. Pitois, “Critical size effect of particles reinforcing foamed composite materials,” *Composites Science and Technology*, vol. 119, pp. 62–67, 2015. [27](#)
- [99] L. Ducloué, O. Pitois, J. Goyon, X. Chateau, and G. Ovarlez, “Rheological behaviour of suspensions of bubbles in yield stress fluids,” *Journal of Non-Newtonian Fluid Mechanics*, vol. 215, pp. 31–39, 2015. [26](#), [27](#), [28](#)
- [100] R. W. Style, R. Boltyanskiy, B. Allen, K. E. Jensen, H. P. Foote, J. S. Wettlaufer, and E. R. Dufresne, “Stiffening solids with liquid inclusions,” *Nature Physics*, vol. 11, pp. 82–87, 2015. [27](#)
- [101] T. L. Nguyen Thi, L. Ducloué, G. Ovarlez, and X. Chateau, “Rhéologie des suspensions de bulles dans un fluide à seuil,” in *21ème Congrès Français de Mécanique*, (Bordeaux, France), August 2013. [27](#), [28](#)
- [102] L. Gibson and M. Ashby, eds., *Cellular Solids: Structure and Properties*. Cambridge: Cambridge University Press, 1997. [27](#)
- [103] F. Gorlier, Y. Khidas, A. Fall, and O. Pitois, “Optimal strengthening of particle-loaded liquid foams,” *Physical Review E*, vol. 95, 2017. [29](#)

Chapter 2

Effects of surfactants on the yield stress of cement paste

Sommaire

2.1 Introduction	40
2.2 Background	40
2.2.1 Surfactant molecules in cement paste	40
2.2.2 Foam stability	42
2.2.3 Yield stress of solid suspensions	43
2.3 Materials and methods	44
2.3.1 Materials	44
2.3.1.1 Cement	44
2.3.1.2 Synthetic cement pore solution	44
2.3.1.3 Surfactants	44
2.3.1.4 Cement paste preparation	44
2.3.2 Methods	46
2.3.2.1 Surfactant compatibility with cement pore solution	46
2.3.2.2 CMC	46
2.3.2.3 Yield stress	46
2.3.2.4 Adsorption	47
2.3.2.5 Contact angle	47
2.4 Results and discussion	48
2.4.1 Surfactants in synthetic cement pore solution	48
2.4.2 Adsorption sites and surfactant distribution	50
2.4.3 Relation between yield stress and adsorbed surfactant	53
2.4.3.1 Yield stress drop at high concentration range	53
2.4.3.2 Yield stress increase at low concentration range	54

2.5 Conclusion	55
Bibliography	58
Appendix A: Additional surfactants	59
Appendix B: Compatibility with calcium hydroxide solution	61
Appendix C: Delay of hydration	62

This chapter, without the appendices, has been published as:

B. Feneuil, O. Pitois and N. Roussel, "Effect of surfactants on the yield stress of cement paste", *Cement and concrete Research*, vol. 100, pp. 32-39, 2017

2.1 Introduction

Cement foams are promising materials. Indeed, addition of air into cement paste may offer, besides substantial material savings, improved thermal properties. This is why, since several years, the study of aerated cementitious materials has become an active field of research. In order to control cement foam morphology, the destabilisation mechanisms of fresh cement foams, until cement hardening, must be stopped or slowed. Stabilisation can be achieved by monitoring rheological properties of the fresh cement paste, especially its yield stress [1, 2, 3].

Most formulations of cement foams include chemicals known as surfactants. Surfactants can either enhance air entrainment into cement paste (air entraining agents) during fast stirring of the cement slurry, or they can be used to create a pre-formed aqueous foam which is later incorporated into the cement slurry. In both processes, surfactants remain in the cement paste and may thus affect the rheological and early age properties of the cement matrix.

Besides cement foams, surfactants can be used as air entraining agents in frost-resistant concrete and as shrinkage reducing admixtures [4].

In this study, we consider the interaction of surfactants with a cement paste. We first investigate the effect of a synthetic pore solution on the foaming ability of these surfactants. Then, we measure the effect of surfactant addition on the yield stress of the cement paste. Our results show the major role played by the amounts of surfactant adsorbed at the surface of the cement grains both on fresh cement paste yield stress and on the hydrophobization of the cement grains.

2.2 Background

2.2.1 Surfactant molecules in cement paste

Surfactant molecules are composed of a hydrophilic head and a hydrophobic hydrocarbon tail. In aqueous solution, some surfactant molecules adsorb at the air-water interface, with their hydrophobic tails towards air, which reduces the liquid-air surface tension

γ [5, 6]. Above the Critical Micelle Concentration (CMC), the air-water interface becomes saturated with surfactant molecules while residual surfactant molecules in bulk solution gather into elements called micelles. As a consequence, above CMC, liquid-air surface tension does not decrease any more with increasing surfactant concentration as shown in Fig. 2.1.

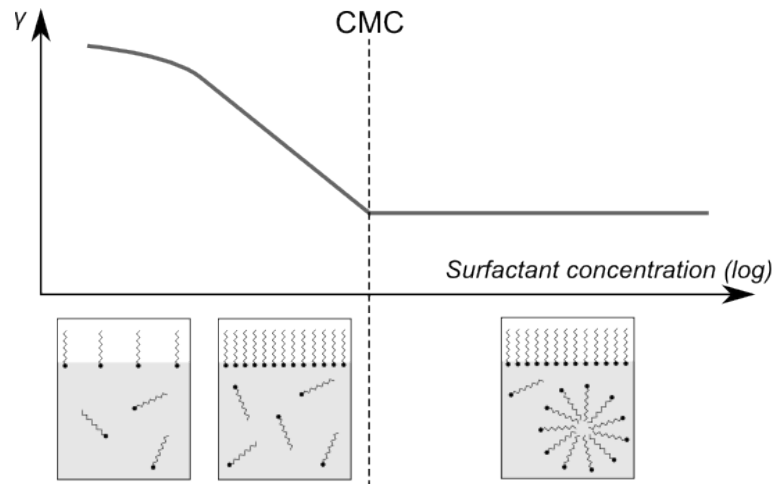


Figure 2.1: Surfactant distribution and surface tension

The hydrophilic head can either be charged (ionic surfactants) or polar (non-ionic surfactants). Ionic surfactants are said cationic if their charge is positive, anionic if their charge is negative and amphoteric when their head include both types of charge [5, 6]. Surfactants enhance foam creation and foam stability through several mechanisms. First, lowering surface tension means that less energy is needed to create air-water interface. Then, layers of surfactant on both sides of the water film separating two bubbles repel each other due to some steric interactions and, in the case of ionic surfactants, some electrostatic interaction. In addition, it was shown that micelles or other structures inside the film may contribute to its stabilisation [5]. It is worth noting that dynamics of surfactant adsorption at air-water interface is also an important aspect for foam generation and stability: to stabilize newly formed interfaces, surfactant adsorption must indeed be faster than surface formation [5]. Length of stretched hydrocarbon chain in nm is related to the number of carbon atoms n_C by [7]:

$$l = 0.1275(n_C - 1) + 0.19 + 0.23 \quad (2.1)$$

Stretched length of a 10 carbon chain is therefore 1.57 nm, which gives an idea of the size of these molecules compared to other organic compounds used as additives in the cement and concrete industry, namely around 5 nm for water reducing agents such as PCE comb copolymer coils [8, 9, 10] and around 50 nm for the coiled macromolecules used as viscosity agents [11].

Most organic additives for cement adsorb on the cement grain surfaces [12, 13]. In the case of large molecules, such as poly-carboxylic ethers, adsorption of polymer coils leads

to steric repulsion between grains and to a decrease in the yield stress of the suspension [14, 15].

Adsorption of surfactant molecules on cement grains has been reported by [6, 16, 17]. Due to their specific molecular structure, surfactant molecules may adsorb in various configurations as single molecules adsorption is reported to find its origin in either the hydrophilic head or the hydrophobic tail depending on the surface properties [12, 13]. While in 1992, Uchikawa et al. [16] made the hypothesis that hydrophilic heads were oriented towards the bulk solution, the hypothesis of electrostatic adsorption of the head was latter most common for ionic surfactants [6, 13, 17]. Zhang et al. [17] measured adsorption on cement of three surfactants - cationic, anionic and non-ionic - and compared adsorption isotherms with contact angle on compacted cement powder pastilles (see details of a similar protocol in paragraph 2.3.2.5). They observed no adsorption with the non-ionic surfactant, whereas partial adsorption of both tested ionic surfactants was measured no matter their initial concentrations. For ionic surfactants, adsorption of ionic heads on the cement particle surface is reported to lead to an hydrophobization of the grain surface and thus to an increase of the contact angle with water of the resulting hardened material up to a maximum value reached when the grain surface is saturated. At higher concentrations, hydrophobicity of the cement grains surface was noted to decrease in the case of anionic surfactant. This effect was explained by the formation of surfactant agglomerates at the surface of the grains. Recently, Petit et al. [18] also measured the above hydrophobicity maximum at intermediate concentrations for one anionic surfactant. The experimental procedure was the imbibition of cement powder by the surfactant solution. They observed no effect of cationic surfactant on cement surface properties.

2.2.2 Foam stability

Before cement setting and hardening, the initial pores structure obtained after mixing can get destabilized through three distinct mechanisms: (1) the gravity driven flow of the paste through the rising bubbles leads to an heterogeneous distribution of air within the sample, (2) difference in capillary pressure between bubbles of different sizes leads to gas exchange (ripening); it leads to bubble rearrangements and a global increase of the average bubble size R_b as a function of time, and (3) foam films breakage induces the coarsening of the bubble assembly through coalescence events. It is to note that the magnitude of the two latter mechanisms increases as the gas fraction increases, which is precisely a consequence of gravity drainage.

Bubble coalescence is generally counteracted by a significant disjoining pressure arising in thin liquid films due to the presence of surfactants at concentrations above the CMC. However, in cement pastes and more specifically in the high ionic strength interstitial fluid, the ability of common surfactants to ensure the stability of thin water films is not obvious and deserves specific investigation [6].

A relevant strategy to control the destabilizing mechanisms of a foam is to take advantage of yield stress (τ_y) properties of pastes [1, 2, 3]: basically, drainage stops as $\tau_y \sim \rho g r$,

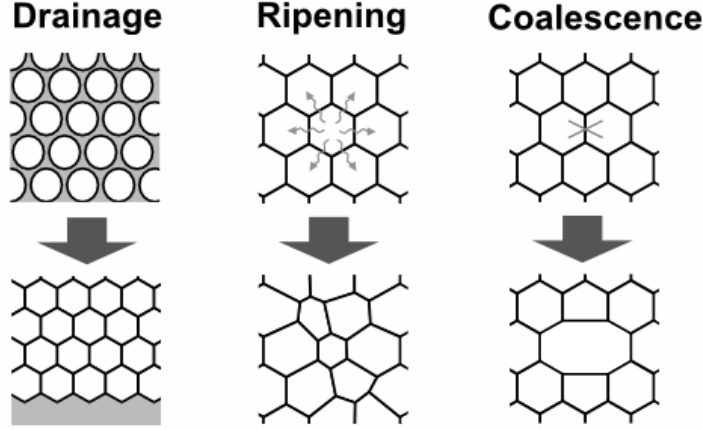


Figure 2.2: Destabilisation mechanisms in a foam

where ρ is the density of the paste and r is the typical size of interstices between the bubbles. Moreover, the ripening process is strongly dampened as $\tau_y \sim \gamma/R_b$, where γ is the surface tension of the liquid/air interface. An alternative foam stabilization strategy involves particles adsorption at the bubbles surface thanks to the in-situ hydrophobization of the particles contained in the paste to be foamed [19], [18]. No matter the strategy chosen to stabilize the foamed material, adsorption properties of surfactants at the surface of cement grains appear in all literature available as a crucial parameter.

2.2.3 Yield stress of solid suspensions

Cement paste is a suspension a solid cement grains in aqueous phase. The yield stress τ_y depends on the interaction of each solid particle with its closest neighbors. A relation between macroscopic yield stress and particle interaction has been proposed in the so-called Yodel [20]. In this model, the inter-particle force parameter $G(h)$ is defined as

$$G(h) = \frac{F_{VdW} + F_{ES} + F_{Ster}}{\tilde{a}} \quad (2.2)$$

where F_{VdW} is Van der Waals attractive force between particles, F_{ES} is the electrostatic interaction, F_{Ster} is the steric interaction and \tilde{a} refers to the radius of curvature of the particle surface. G depends on the distance h between solid grains. Flatt et al. [20] showed that the yield stress of a suspension is proportional to the maximum value of G , obtained at the minimal inter-particle distance.

Hence, to understand the change of yield stress with surfactant addition, analysis of the interactions between cement grains must be carried out. First, attraction due to the Van der Waals force is inversely proportional to the square of the interparticle distance: $F_{VdW} \propto 1/h^2$. Thus, increasing distance between the cement grains reduces the Van der Waals interaction. Secondly, for a charged surface in an electrolyte solution, the range of the electrostatic force is given by the Debye length κ^{-1} . The Debye length gives the thickness of the ions layer balancing the electrostatic close to the solid surface. In cement paste, the Debye length is rather small because of the high ionicity of the interstitial solu-

tion, i.e. $\kappa^{-1} \simeq 0.7\text{nm}$ [14]. Thirdly, steric interaction depends on the thickness of the layer of adsorbed molecules on grains surface. Adsorbed layers on grain surfaces can hardly interpenetrate. For instance, poly-carboxylate superplasticizers are polymers which adsorb on cement grain surface. The layer they form is at least 2.5nm thick. If h_{Ster} is the thickness of the layer of adsorbed molecules, steric interaction imposes $h \geq 2h_{Ster}$. The increase of the distance between the grains leads to a lowering of the attractive Van der Waals forces and thus to fluidification of the paste.

2.3 Materials and methods

2.3.1 Materials

2.3.1.1 Cement

Cement is a CEM I from Lafarge, Saint Vigor. Blaine specific surface provided by the manufacturer is $0.359 \text{ m}^2/\text{g}$. Chemical composition is given in table 2.1.

C ₃ S	C ₂ S	C ₃ A	C ₄ AF	CaO/SiO ₂	Al ₂ O ₃
62.0%	16.0%	2.1%	15.2%	3	4%
MgO	Na ₂ O +0.658 K ₂ O		SO ₃	Gypsum	L.O.I.
1.1%	0.34 %		2.58 %	2.4%	0.9%

Table 2.1: Chemical composition of CEM I cement from Lafarge, Saint-Vigor

2.3.1.2 Synthetic cement pore solution

To study the effects of ions from the cement paste on surfactants, a synthetic cement pore solution is prepared by dissolving in distilled water 1.72 g/L of $\text{CaSO}_4 \cdot 2\text{H}_2\text{O}$, 6.959 g/L of Na_2SO_4 , 4.757 g/L of K_2SO_4 and 7.12 g/L of KOH [21].

2.3.1.3 Surfactants

Surfactants are listed in table 2.2 with their charge, molar mass and active content when given by the provider. Average values are presented when necessary. All of them have been used as received from the provider. Fig. 2.3 gathers their molecular structures.

2.3.1.4 Cement paste preparation

The cement pastes studied here have a water-to-cement ratio of 0.5. They are prepared as follows:

1. A cement paste at water-to-cement ratio 0.4 is prepared by adding cement to distilled water and is mixed by hand for 1 min.

Name	Charge	Molar Mass (g/mol)	Purity $a_{\%}$	Provider
TTAB	+	336	$\geq 99\%$	Sigma-Aldrich
TEGO [®] Betain F50	+/-	343		Evonik
SDS	-	288	$\geq 98.5\%$	Sigma-Aldrich
Steol [®] 270 CIT	-	382	68-72%	Stepan
Bio-Terge [®] AS-40K	-	315	39.1%	Stepan
Triton [™] X-100 (laboratory grade)	0	625		Sigma-Aldrich
Brij 700	0	4670		Sigma-Aldrich
Tween [®] 20	0	1225	97%	Acros

Table 2.2: Surfactant properties. Molar weight is an average in the case of mixed molecules and $a_{\%}$ is the active content of the products

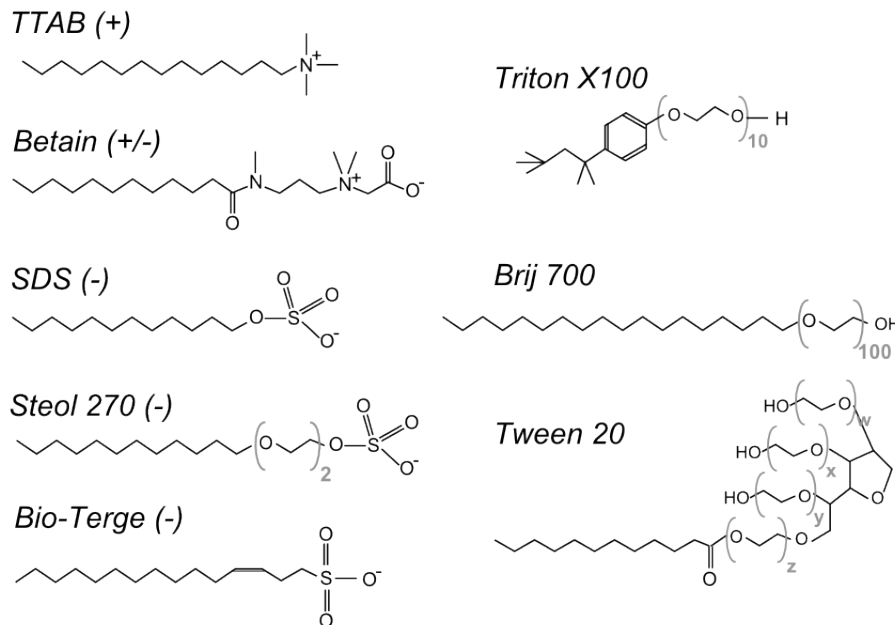


Figure 2.3: Surfactant molecular structures. Bio-Terge is a mix of several molecules close to the one drawn here.

2. The paste rests for 20 min so that first hydration products (mostly sulfo-aluminates) form [21] before surfactants are added.
3. A solution of surfactant in distilled water is added, in such a way that the final water to cement ratio reaches $W/C=0.5$. Hence, if the surfactant concentration in the added solution is C_{add} , the concentration of the surfactant in the whole amount of water contained in the cement paste is $C_i = 1/5 \times C_{add}$.
4. The paste is mixed manually and slowly to avoid any air entrainment for 5 min.

A very important point to note here is that our mixing protocol is specifically chosen

in order to avoid any air entrainment or any foaming. We focus here on the role of surfactants only and we therefore chose to prepare pastes, in which the presence of a surfactant and its concentration were the only varying parameters. For some samples, we checked a posteriori that only very few bubbles were entrained through the surfactant addition protocol either by centrifugation of the sample or by addition of small amount of the paste into distilled water. We did not visually detect any air bubbles release in these tests (results not shown here).

2.3.2 Methods

2.3.2.1 Surfactant compatibility with cement pore solution

50mL tubes are filled with 10mL of solution containing 0.1 g of surfactant. Tubes are shaken by hand during 15s, then placed vertically at rest. First, precipitation is visually assessed, then samples are classified according to their foaming capacity:

- 0 : No foam
- + : Foam volume below 20 mL
- ++ : Moderately stable foam
- +++ : The tube is filled with foam for longer than 1h

For each surfactant, a sample prepared from the synthetic cement pore solution described in paragraph 2.3.1.2 is compared to a reference sample prepared with distilled water (pH=7).

2.3.2.2 CMC

CMC in water and in cement pore solution are obtained from surface tension measurements using the Pendant Drop Method and a Teclis tensiometer (see figure 2.1). The test consists in generating a drop of solution at the lower end of a vertical needle. The surface tension is then computed from the drop profile, according to the Young-Laplace equation.

2.3.2.3 Yield stress

Yield stress is assessed using simple spread tests. Cement paste is poured on a horizontal flat surface. When flow stops, two perpendicular diameters of the paste deposit are measured. The yield stress is then computed from the average radius R , the sample volume ω and the material density ρ using the following formula [22]:

$$\tau_y = \frac{225\rho g\Omega^2}{128\pi^2 R^5} \quad (2.3)$$

Note that Eq. 2.3 is valid if the thickness of the sample is small compared to its radius and if the surface tension effects can be neglected. The second condition writes:

$$\tau_y \gg \frac{3(1 - \cos\theta)\gamma}{R} \quad (2.4)$$

Theta is here the contact angle between the cement paste and the solid surface. γ being smaller than the value for pure water, i.e. 70 mN/m, and R being higher than 5 cm for our tests, the second term of equation 2.4 is of the order of 0.1 Pa. Thus, all measured values computed from Eq. 2.3 which are below 1 Pa are taken equal to 1 Pa.

2.3.2.4 Adsorption

To measure adsorption of surfactants on cement grains, we centrifuge the cement paste to collect the interstitial liquid. This liquid is filtered through a 0.45 μm polypropylene filter and analyzed with a Total Organic Carbon analyser TOC V_{CSH} manufactured by Shimadzu.

TOC values are converted into concentration through calibration curves, which have been previously identified for each surfactant. The measured raw value is corrected by subtracting the carbon content of the cement powder due to the presence of grinding aids [21]. This gives access to the residual concentration of surfactants in the extracted interstitial liquid C_r . Adsorption value A per gram of cement is then calculated as follows: $A = (C_i - C_r) \times W/C$.

It can be noted that the relative error is large for smaller residual concentration as measured TOC values get close to the reference value due to grinding aid. Hence, all residual concentration values below 0.01 g/L have been set to 0.01g/L. As the smallest surfactant initial concentration is 0.1g/L, error on adsorption value is below 10%.

2.3.2.5 Contact angle

The contact angle of water on cement α is measured by placing a distilled water drop on a cement pastille using a tensiometer (Teclis).

To prepare the cement pastille, the cement paste is mixed as described in 2.3.1.4, then most of the water is removed either by sedimentation or by filtration. Full drying is then obtained by placing the sample in a 20°C and 30% humidity chamber for at least 30 hours. The resulting solid is ground into a fine powder, which is then compacted to prepare 2 cm diameter pastilles by applying a 210 MPa compaction stress for 15 seconds. Preliminary tests showed that increasing compaction stress from 150 to 210 MPa reduces the penetration speed of the water into the pastille; hence, 210 MPa stress has been chosen for all samples.

α is assessed from images of the water drop as shown in figure 2.4. After the drop is set on the pastille, it fully penetrates into cement in 2 to 10 seconds, even if the surface is initially hydrophobic. This may be explained by the change in surface properties due to the dissolution of adsorbed surfactant molecules into water. This specific phenomenon may lead to underestimate α . Picture is taken 1 second after drop deposition and for each sample, measurement is repeated 4 times and the average value is considered.



Figure 2.4: Example of pictures used for contact angle measurement. Left : reference sample, $\alpha = 19.6^\circ$; right : sample with initial concentration of Bio-Terge of 25 g/L, $\alpha = 103^\circ$

2.4 Results and discussion

2.4.1 Surfactants in synthetic cement pore solution

Foamability of surfactant solutions in water and in cement pore solution are summarized in table 2.3. For the latter case, the table reports whether a precipitate was observed.

Surfactant		Precipitation	Foam		Compatibility
			in water	in cement sol.	
+	TTAB	No	+++	++	YES
+/-	Betain	No	++	0	no
-	SDS	Yes	+++	0	no
	Steol 270	No	+++	+++	YES
	Bio-Terge	No	+++	+++	YES
0	Triton X100	No	++	++	YES
	Brij 700	No	+	0	no
	Tween 20	Yes	+	0	no

0 : No foam
 + : Foam volume below 20 mL
 ++ : Moderately stable foam
 +++ : Tube filled with 40 mL foam for longer than 1h

Table 2.3: Precipitation and foamability of surfactants in distilled water and synthetic cement pore solution

For some surfactants, foam could not be obtained in presence of the synthetic cement pore solution while foam could be generated with the same surfactant in distilled water. Among them, SDS and Tween 20 precipitated when added to the cement solution. This observation for SDS is in agreement with results reported by Jolicoeur [23], who noticed that there is no residual surfactant in solution when SDS is added to a cement paste, even at high surfactant dosage. Note however that air bubbles have been successfully entrained in the cement pastes containing SDS in [23, 24]. Some authors [4, 23] suggested that the insoluble surfactant - calcium salts enhance stabilization of the bubbles. Similar conclusion was obtained by Tunstall et al. [25], who observed the complexation of some

commercial air-entraining agents in their synthetic cement pore solution. Besides, Petit et al. [18] observed a modification of the surface properties of cement grains when adding SDS to a cement paste, suggesting that, at the low concentration they studied, some SDS molecules did not precipitate but adsorbed on cement grain surface.

Regarding Betain and Brij 700, even if no precipitate could be visually observed, no foam could be generated in the synthetic cement pore solution. One hypothesis to explain the incompatibility of Betain and Brij 700 with cement solution is the formation of soluble complexes with ions (calcium, sulfate...).

The other four surfactants are compatible with the cement solution: one of them is cationic (TTAB), two are anionic (Steol and Bio-Terge) and one is non ionic (Triton). In the following, we will focus on these four surfactants.

Surface tension was measured for distilled water and synthetic cement pore solution without surfactant. In both cases, it was around 71mN/m. Figure 2.5 gives the surface tension curves for all four compatible surfactants. On the X-axis, concentration refers to the total surfactant mass added to the solution whether they are under liquid or solid form, which means that it includes some water in the case of Steol and Bio-Terge solutions (see table 2.2).

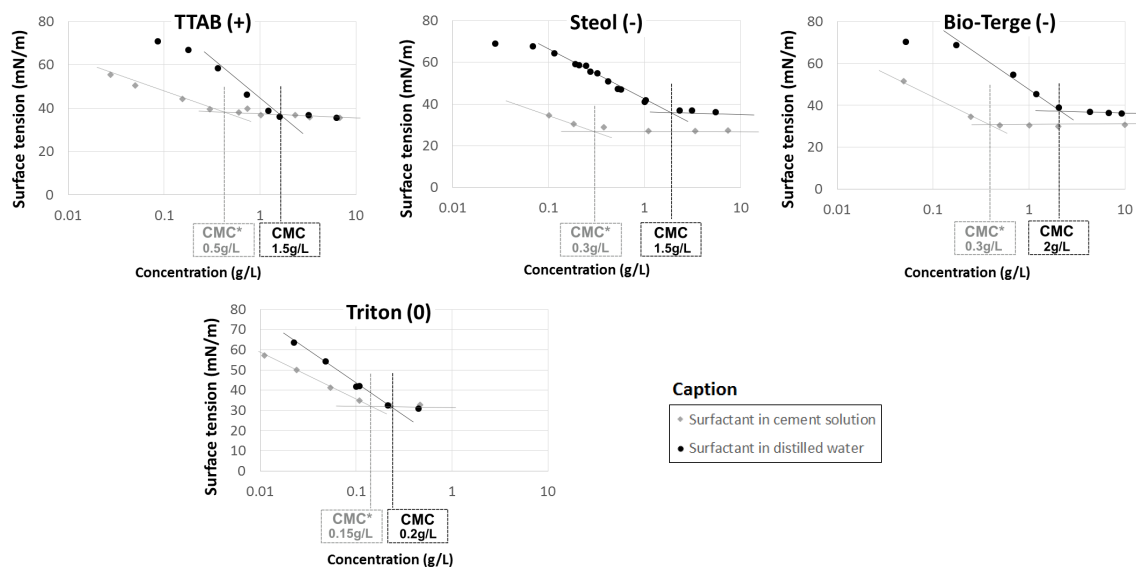


Figure 2.5: Comparison on surface tension curves of compatible surfactants in distilled water and synthetic cement pore solution

The cement solution has a strong effect on the surface tension of solutions containing ionic surfactants. Because of the high ion content, electrolyte solution reduces the range of the electrostatic repulsion between surfactant charged heads [5]. Therefore, surfactant density increases at gas-water interfaces, which leads to a decrease of the surface tension. As expected, this reduction is found to be small for non-ionic Triton. Tunstall et al. [25] observed, with some of the anionic surfactants they tested, an increase of surface tension in alkaline solutions containing calcium ions. This effect was related to the loss of surfactant molecules available to settle at air-water interface due to the formation of complexes

with calcium ions. This effect is not observed in figure 2.5 because the chosen surfactants are not affected by calcium ions.

CMC are deduced from these curves as the intersection of two straight lines, each of them being representative of the surfactant effect before and after the CMC. In the following, the CMC measured in the synthetic cement pore solution is noted CMC*. All extracted CMC in water and CMC* are given in table 2.4. For all ionic surfactants, CMCs are lower in synthetic cement pore solution than in distilled water solutions whereas it stays almost constant for the non-ionic surfactant. Indeed, reduction of the electrostatic force range favors the agglomeration of ionic surfactant molecules into micelles.

Surfactant	CMC	CMC*
TTAB (+)	1.5 g/L	0.5 g/L
Steol (-)	1.5 g/L	0.3 g/L
Bio Terge (-)	2 g/L	0.5 g/L
Triton (0)	0.2 g/L	0.15 g/L

Table 2.4: CMC in distilled water and CMC* in synthetic cement pore solution. Values give weight of the surfactants as sold by the providers.

It is worth noting that electrostatic repulsion between surfactant layers may contribute to the stabilization of liquid films in foams. As a consequence, the above screening of these forces may be at the origin of the faster destabilisation of the TTAB foam in cement solution reported in Table 3 as well as the inability of Betain to form foam with the synthetic cement solution.

2.4.2 Adsorption sites and surfactant distribution

Adsorption isotherms for the four compatible surfactants are given in figure 2.6.

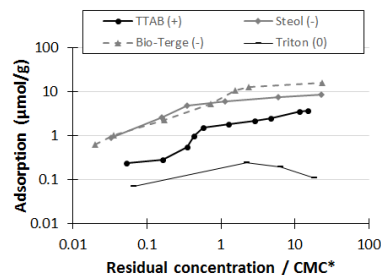


Figure 2.6: Comparison of adsorption isotherms of compatible surfactants. On Y-axis, adsorption is given in μmol per gram of cement and on X-axis, residual concentration is divided by the CMC* in synthetic cement pore solution (see table 2.4).

First, let us note the difference of maximum adsorption for the surfactants. Measured maximal adsorption is, for one gram of cement, 4.6 g of Steol and 13 g of Bio-Terge, that is to say respectively $8.5 \mu\text{mol}$ and $16 \mu\text{mol}$. Maximum adsorption of TTAB is $3.7 \mu\text{mol}$ (1.3

g) per gram of cement. As mentioned in part 2.3.1.4, surfactants are added to the cement paste 20 minutes after the first contact between cement and water. At this time, solid surfaces in solution are hydroxylate surfaces of clinker phases, mainly C_3S and C_2S , and first hydration products, C-S-H, ettringite and portlandite. In high electrolyte solution like cement pore solution, calcium ions adsorb on negatively charged silicate surfaces (C_3S , C_2S , C-S-H and portlandite), resulting in positive zeta potential [26]. On the other hand, sulfate ions adsorbed on ettringite provide for negative zeta potential [26]. The diversity of solid surfaces accounts for the different affinities of cationic and anionic surfactants.

Very low adsorption is measured for non-ionic Triton X100 (maximum 0.12 mg/g or 0.19 $\mu\text{mol/g}$), which is consistent with previous measurements of adsorption with this surfactant [17].

Isotherms of Steol, Bio-Terge and TTAB in figure 2.6 can be compared with adsorption isotherms of ionic surfactant from the literature. Such adsorption has indeed been extensively studied [27, 28, 29, 30, 31] on silica or metal oxides. Typical adsorption isotherm comprises four regimes: (1) isolated molecules adsorb "head on" thanks to electrostatic attraction, (2) adsorption rate increases due to favorable hydrophobic interactions with tails of previously adsorbed molecules, (3) starting from a residual concentration called hemimicelle concentration (HMC) surface agglomerates form by attraction of the hydrophobic tails on hydrocarbon chains of the first layer of molecules. (4) at residual concentrations close to the CMC, adsorption reaches a plateau. This plateau may have two origins: first, free molecule concentration varies slowly above CMC and micelles do not adsorb on the surface [27, 30] (pseudophase separation model), secondly, the solid surface may be saturated with surface agglomerates.

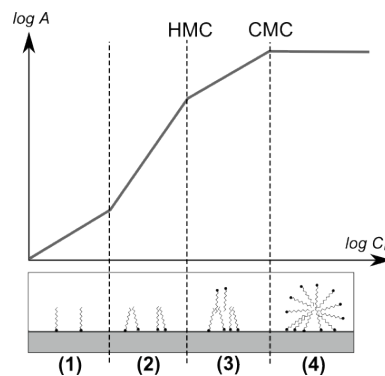


Figure 2.7: Four regimes model for adsorption of ionic surfactants on oppositely charged surfaces. Schema is adapted from [29, 30].

The above four regimes cannot be clearly identified on Steol, Bio-Terge and TTAB isotherms on figure 2.6. Main difference between cement and model systems from the literature are the diversity in potential adsorption sites in cement paste, to which one given surfactant may have different affinities, making the dissociation of adsorption regimes difficult. Though, we can observe that, for all of these three molecules, the adsorption plateau is indeed reached close to the CMC*.

Regarding cationic TTAB, at lowest concentrations, adsorption is very low so that ini-

tial slope is close to zero and adsorption isotherm has an S-shape. S-shaped adsorption isotherms have been simulated by Zhu et al. [31] for systems where the equilibrium constant of the formation of surface agglomerates is high compared to the constant related to the adsorption of one molecule. In other words, in systems simulated by Zhu et al., an adsorbed molecule hardly remains alone. This translates in a very low adsorption of single molecules at low concentrations and a brutal rise in adsorption as soon as concentration allows for the formation of agglomerates.

Contact angle of cement grain surface are plotted as a function of surfactant concentration in Fig. 2.8.

For the reference sample, measurement has been carried out on 4 different cement pastilles. The 15 obtained contact angle values range from 11° to 34° with average value 21° and standard deviation 7° (i.e. 33% of the average value).

Regarding samples containing surfactant, the drop imbibition takes more time, probably because surfactant dissolution is required prior to imbibition. For each surfactant concentration, contact angle is measured on four different drops. Error bars in Fig. 2.8 give the highest and the lowest of the four values. They provide for an estimation of the error related to the time of the measurement. Maximum relative error is 15% of the contact angle for both anionic surfactants (Steol and Bio-Terge), 20% for cationic TTAB and 30% for Triton. Relative errors are smaller when surfactant adsorption is higher, which tends to show that drop imbibition is delayed because of the surfactant desorption time.

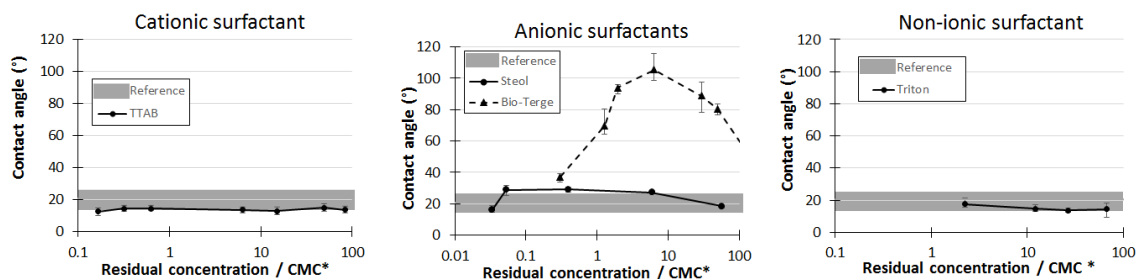


Figure 2.8: Contact angle of cement surface after surfactant adsorption

Anionic surfactants increased the contact angle up to a maximal contact angle at intermediate concentrations. No change of contact angle was observed for samples containing TTAB or Triton.

Contact angle curves for anionic surfactants are consistent with previous results from literature [17]. They confirm that surface agglomerates form at residual concentration close to CMC^* . Indeed, contact angle increases at low concentrations indicating that a monolayer of surfactant forms on cement grain surface. In this concentration range, molecules heads adsorb through electrostatic interaction and hydrocarbon chains are oriented outwards. Contact angle increases as the number of adsorbed molecules increases. In the higher concentration range, reduction of contact angle shows that orientation of the additional molecules is opposite: hydrophilic heads are oriented toward the solution.

Contact angle for TTAB cationic surfactant is constant. Eventually, contact angle measurement and adsorption isotherm shape both seem to show that during adsorption of TTAB, adsorbed molecules tend to agglomerate even at low concentrations while the amount of free molecules adsorbed at low concentrations is too low to affect contact angle.

2.4.3 Relation between yield stress and adsorbed surfactant

Yield stress measurements of the reference paste without surfactant were repeated three times. The average value was 11.9 Pa and the standard deviation was 0.6 Pa. Results for surfactant containing samples are given in the graphs of figure 2.9.

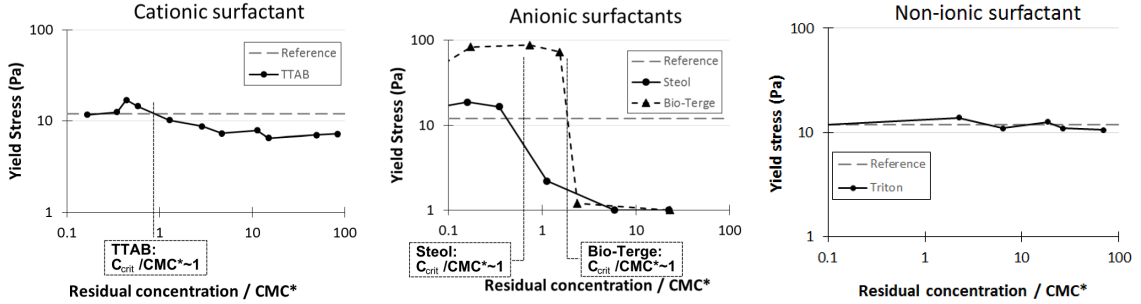


Figure 2.9: Yield stress results of compatible surfactants on cement

Results presented in figure 2.9 show a drop in yield stress down to below 1 Pa above a concentration threshold for two surfactants: Steol and Bio-Terge. A slight yield stress reduction, down to half the reference value, is also observed for TTAB. At low concentration range, a large increase in yield stress is observed for Bio-Terge, and a small increase for Steol. It remains close to the reference paste value for all other surfactants. No variation of yield stress is observed for Triton, which is consistent with the very low adsorption and the absence of contact angle variations.

We note C_{Crit} the critical residual concentration between higher yield stress regime and low yield stress regime. It is for all three ionic surfactants close to CMC^* .

2.4.3.1 Yield stress drop at high concentration range

Figure 2.9 shows that, for Steol and BioTerge, yield stress drops drastically above $C_{Crit} \approx CMC^*$ the adsorption plateau is reached and the contact angle is maximal, *i.e.* when surfactants agglomerate on cement grains surfaces. Besides, using the light scattering method, the typical diameters of Steol and Bio-Terge micelles in synthetic cement pore solution were measured to be around 10 nm. It is one order of magnitude above the Debye length $\kappa^{-1} \approx 0.7\text{nm}$ [14], which means that these adsorbed micelles are large enough to increase inter-particle distance through steric repulsive interactions. We can then suggest that drop in yield stress is due to steric repulsion between cement grains related to the agglomeration of adsorbed surfactant molecules.

Lower amounts of TTAB are adsorbed compared to anionic surfactants, so that some surfaces are not covered by TTAB. This may cause the lower reduction of yield stress ob-

served for this surfactant above $C_{Crit} \simeq CMC^*$. Besides, TTAB micelle typical size measured in synthetic cement pore solution is slightly smaller than other surfactants, i.e. 5nm.

2.4.3.2 Yield stress increase at low concentration range

Regarding concentrations below the threshold, for both anionic surfactants, the yield stress increases. A previous study showed a 40% increase of dynamic viscosity due to added anionic surfactants (SDS, sodium abietate and petroleum sulfonate) at low concentration, i.e. 0.1wt% of cement [32]. As a comparison, in the present study the yield stress drops when the initial concentrations of Steol and Bio-Terge are above respectively 0.3 and 1wt%. The present results shed new light on results from [32]: at low shear rate $\dot{\gamma}$, the apparent viscosity η of yield stress fluid is related to the yield stress by $\eta \sim \tau_y/\dot{\gamma}$, therefore, a relative increase of τ_y leads to the same relative increase of η .

We have already mentioned that, in the residual concentration regime below CMC^* , a single layer of adsorbed molecules turns the grains surface hydrophobic. Several authors have shown that hydrophobic surfaces tend to attract each other [33, 34]. This hydrophobic interaction is for instance the driving mechanism for the formation of surfactant micelles in solution [34].

The force between two hydrophobic surfaces F_H can be estimated from the radius of curvature of the surface \tilde{a} and the surface tension between water and hydrocarbons γ_H [33] at the distance h where both hydrocarbon layers are in contact :

$$F_H = 2\pi\tilde{a}\gamma_H \quad (2.5)$$

The irregular shape of cement grains makes the radius of curvature \tilde{a} difficult to estimate. Though F_H can be compared with van der Waals force, which is also proportional to \tilde{a} [20, 33, 35]:

$$F_{VdW} = \frac{1}{12}A(h)\left(\frac{\tilde{a}}{h^2}\right) \quad (2.6)$$

At separation distance of a few nanometers, Hamaker constant $A(h)$ is close to the reference value $A(0)$, which is of the order of magnitude of $10^{-20}J$ in cement pastes[35]. In addition, the order of magnitude of γ_H is $10^{-2}J/m^2$ [33]. The ratio of hydrophobic to van der Waals interactions can be roughly estimated as:

$$F_H/F_{VdW} \sim 24\pi h^2\gamma_H/A(0) \sim 10^2$$

This shows that hydrophobic attractive interaction potentially dominates van der Waals attractive forces between hydrophobic particles at separation distance above $h = 2$ nm.

Number of carbons in hydrocarbon chains of surfactant molecules are 12 for Steol and 14 to 16 for Bio-Terge. Estimation of their length with formula 2.1 gives thus 1.8nm for Steol and 2.2nm for Bio-Terge. Either this length difference or simply the higher local hydrocarbon density may explain why the yield stress increase is larger with Bio-Terge.

2.5 Conclusion

We observed in this work several distinct behaviors for surfactants when they are introduced into a cement paste:

1. precipitation, which in turn leads to loss of foamability of the molecule,
2. adsorption on cement grains surface and
3. no interaction with cement grains.

In case (2), the surfactant noticeably affect the rheology of the cement paste. At low concentration, i.e. below a critical residual concentration C_{Crit} , molecules adsorb head on. Hydrophobic forces between tails results in most cases in an increase of the yield stress with respect to the surfactant-free paste. At high concentration range, above C_{Crit} , the formation of large surface agglomerates is at the origin of a brutal decrease in yield stress due to steric hindrance.

To manufacture a cement foam, the low concentration regime $C_r < C_{Crit}$ could be promising. First, high yield stress values enhances foam stabilization. In addition, surfactant monolayer induces hydrophobization of cement grains, and hydrophobic particles are known to stabilize liquid films by setting at air-water interfaces.

Bibliography

- [1] S. Guignot, S. Faure, M. Vignes-Adler, and O. Pitois, "Liquid and particles retention in foamed suspensions," *Chemical Engineering Science*, vol. 65, pp. 2579–2585, 2010. [40](#), [42](#)
- [2] I. Lesov, S. Tcholakova, and N. Denkov, "Factors controlling the formation and stability of foams used as precursors of porous materials," *Journal of Colloid and Interface Science*, vol. 426, pp. 9–21, 2014. [40](#), [42](#)
- [3] I. Lesov, S. Tcholakova, and N. Denkov, "Drying of particle-loaded foams for production of porous materials: mechanism and theoretical modeling," *RSC Advances*, vol. 4, pp. 811–823, 2014. [40](#), [42](#)
- [4] G. Gelardi, S. Mantellato, D. Marchon, M. Palacios, A. Eberhardt, and R. J. Flatt., "Chemistry of chemical admixtures," in *Science and Technology of Concrete Admixtures* (P.-C. Aïtcin and R. J. Flatt, eds.), pp. 149–218, Woodhead publishing, 2016. [40](#), [48](#)
- [5] I. Cantat, S. Cohen-Addad, F. Elias, F. Graner, R. Höhler, O. Pitois, F. Rouyer, and A. Saint-Jalmes, *Foams - Structure and dynamics*. Oxford University Press, 2013. [41](#), [49](#)

- [6] L. Du and K. Folliard, “Mechanisms of air-entrainment in concrete,” *Cement and Concrete Research*, vol. 35, pp. 1463–1471, 2005. [41](#), [42](#)
- [7] B. Cabane and S. Hénon, eds., *Liquids : Solutions, dispersion, émusions, gels*. Belin, 2003. [41](#)
- [8] P. Borget, L. Galmiche, J. Le Meins, and F. Lafuma, “Microstructural characterisation and behaviour in different salt solutions of sodium polymethacrylate-g-peo comb copolymers,” *Colloids and Surfaces, A: Physicochemical and Engineering Aspects*, vol. 260, pp. 173–182, 2005. [41](#)
- [9] J. Hot, H. Bessaies-Bey, C. Brumaud, M. Duc, C. Castella, and N. Roussel, “Adsorbing polymers and viscosity of cement pastes,” *Cement and Concrete Research*, vol. 63, pp. 12–19, 2014. [41](#)
- [10] G. Gelardi, N. Sanson, G. Nagy, and R. J. Flatt, “Characterization of comb-shaped copolymers by multidetection sec, dls and sans,” *Polymers*, vol. 9, p. 61, 2017. [41](#)
- [11] C. Brumaud, H. Bessaies-Bey, C. Mohler, R. Baumann, M. Schmitz, M. Radler, and N. Roussel, “Cellulose ethers and water retention,” *Cement and Concrete Research*, vol. 53, pp. 176–184, 2013. [41](#)
- [12] C. Jolicoeur and M.-A. Simard, “Chemical admixture-cement interactions: Phenomenology and physico-chemical concepts,” *Cement & Concrete Composites*, vol. 20, pp. 87–101, 1998. [41](#), [42](#)
- [13] D. Marchon, S. Mantellato, and R. Eberhardt, A.B. and Flatt, “Adsorption of chemical admixtures,” in *Science and Technology of Concrete Admixtures* (P.-C. Aïtcin and R. Flatt, eds.), pp. 219–256, Woodhead publishing, 2016. [41](#), [42](#), [62](#)
- [14] R. J. Flatt and I. Schober, “Superplasticizer and the rheology of concrete,” in *Understanding the rheology of concrete* (N. Roussel, ed.), pp. 144–208, Woodhead publishing, 2012. [42](#), [44](#), [53](#)
- [15] A. Perrot, T. Lecompte, H. Khelifi, C. Brumaud, J. Hot, and N. Roussel, “Yield stress and bleeding of fresh cement pastes,” *Cement and Concrete Research*, vol. 42, pp. 937–944, 2012. [42](#)
- [16] H. Uchikawa, S. Hanehara, T. Shirasaka, and D. Sawaki, “Effect of admixture on hydration of cement, adsorptive behavior of admixture and fluidity and setting of fresh cement paste,” *Cement and Concrete Research*, vol. 22, pp. 1115–1129, 1992. [42](#)
- [17] T. Zhang, S. Shang, F. Yin, A. Aishah, A. Salmiah, and T. Ooi, “Adsorptive behavior of surfactants on surface of Portland cement,” *Cement and Concrete Research*, vol. 31, pp. 1009–1015, 2001. [42](#), [51](#), [52](#)
- [18] P. Petit, I. Javierre, P.-H. Jézéquel, and A.-L. Biance, “Generation and stability of bubbles in a cement based slurry,” *Cement and Concrete Research*, vol. 60, pp. 37–44, 2014. [42](#), [43](#), [49](#)

- [19] K. Ramamurthy, E. Kunhanandan Nambiar, and G. Indu Siva Ranjani, “A classification of studies on properties of foam concrete,” *Cement & Concrete Composites*, vol. 31, pp. 388–396, 2009. [43](#)
- [20] R. J. Flatt and P. Bowen, “Yodel: a yield stress model for suspensions,” *Journal of the American Ceramic Society*, vol. 89, no. 4, pp. 1244–1256, 2006. [43](#), [54](#)
- [21] H. Bessaies-Bey, *Polymères et propriétés rhéologiques d’une pâte de ciment : une approche physique générique*. PhD thesis, Université Paris-Est - SIE, 2015. [44](#), [45](#), [47](#)
- [22] N. Roussel and P. Coussot, “Fifty-cent rheometer for yield stress measurements: From slump to spreading flow,” *Journal of Rheology*, vol. 49, no. 3, pp. 705–718, 2005. [46](#)
- [23] C. Jolicoeur, T. To, T. Nguyen, R. Hill, and M. Pagé, “Mode of action of anionic surfactants for air entrainment in cement pastes w-w/o fly ash,” in *2009 World of Coal Ash (WOCA) Conference - May 4-7, 2009 in Lexington, KY, USA*, 2009. [48](#)
- [24] H. Atahan, J. C. Carlos, S. Chae, P. Monteiro, and J. Bastacky, “The morphology of entrained air voids in hardened cement paste generated with different anionic surfactants,” *Cement & Concrete Composites*, vol. 30, pp. 566–575, 2008. [48](#)
- [25] L. Tunstall, G. Scherer, and R. Prud’homme, “Studying AEA interaction in cement systems using tensiometry,” *Cement and concrete research*, vol. 92, pp. 29–36, 2017. [48](#), [49](#)
- [26] A. Zingg, F. Winnefeld, L. Holzer, J. Pakusch, S. Becker, and L. Gauckler, “Adsorption of polyelectrolytes and its influence on the rheology, zeta potential, and microstructure of various cement and hydrate phases,” *Journal of Colloid and Interface Science*, vol. 323, pp. 301–312, 2008. [51](#)
- [27] F. J. Scamehorn, R. S. Schechter, and W. H. Wade, “Adsorption of surfactants on mineral oxide surfaces from aqueous solutions,” *Journal of Colloid and Interface Science*, vol. 85, no. 2, pp. 463–478, 1982. [51](#)
- [28] L. Koopal, E. Lee, and M. Böhmer, “Adsorption of cationic and anionic surfactants on charged metal oxide surfaces,” *Journal of Colloid and Interface Science*, vol. 170, pp. 85–97, 1995. [51](#)
- [29] R. Atkin, V. Craig, E. Wanless, and S. Biggs, “Mechanism of cationic surfactant adsorption at the solid-aqueous interface,” *Advances in Colloid and Interface Science*, vol. 103, pp. 219–304, 2003. [51](#)
- [30] S. Paria and K. Khilar, “A review on experimental studies of surfactant adsorption at the hydrophilic solid-water interface,” *Advances in Colloid and Interface Science*, vol. 110, no. 3, pp. 75–95, 2004. [51](#)

- [31] B. Y. Zhu and T. Gu, "Surfactant adsorption at solid-liquid interfaces," *Advances in Colloid and Interface Science*, vol. 37, pp. 1–32, 1991. [51](#), [52](#)
- [32] R. Rixom and N. Mailvaganam, *Chemical Admixtures for Concrete*. E. & F.N. Spon Ltd, 3rd ed. ed., 1999. p106+. [54](#)
- [33] J. N. Israelachvili and R. M. Pashley, "Measurement of the hydrophobic interaction between two hydrophobic surfaces in aqueous electrolyte solutions," *Journal of Colloid and Interface Science*, vol. 98, no. 2, 1984. [54](#)
- [34] E. Meyer, K. Rosenberg, and J. Israelachvili, "Recent progress in understanding hydrophobic interactions," *PNAS*, vol. 103, no. 43, pp. 15739–15746, 2006. [54](#)
- [35] R. J. Flatt, "Dispersion forces in cement suspensions," *Cement and Concrete Research*, vol. 34, pp. 399–408, 2004. [54](#)
- [36] C. Dame, *Étude des relations entre la stabilité des mousses de décontamination nucléaire et leurs propriétés physico-chimiques*. PhD thesis, Université Paul Cézanne, 2006. [60](#)

Appendix 2A: Additional surfactants

Materials

Alpha Foamer[®] is an anionic surfactant provided by Stepan. It is an ammonium alkyl ether sulfate; average molar mass according to the manufacturer is 277 g/mol and purity 52 %. Chemical formula is not given, but as molar weight of sulfate group, 96 g/mol, and each ether group 48 g/mol, we can assume that the average length of the hydrophobic chain is below $(277-96-48)/16=8$ carbons. Hydrocarbon chain is therefore shorter than in the case of Steol 270 (12 carbons) and Bio-Terge (14 to 16).

Glucopon[®] 225 DK is an anionic surfactant provided by BASF. It is a mix of several molecules of average molar mass 420 g/mol and its purity is 70%. Carbon chain length of the molecules is comprised between 8 and 10 and chemical formulas are close to the one drawn in Fig. 2.10.

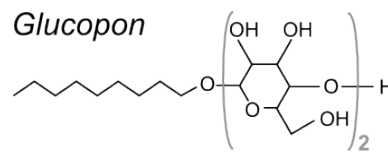


Figure 2.10: Example of chemical formula of a molecule contained in Glucopon non-ionic surfactant. Glucopon is a mix of molecules with carbon chain length between 8 and 10, and number of glucoside group may vary.

As shown in Appendix B, they are both compatible with synthetic cement pore solution.

Surface tension measurements

Effect of synthetic cement pore solution on surface tension curves is very similar to other surfactants: cement solution reduces the CMC and the surface tension at given surfactant concentration. This effect is smaller for the non-ionic surfactant than for the anionic surfactant.

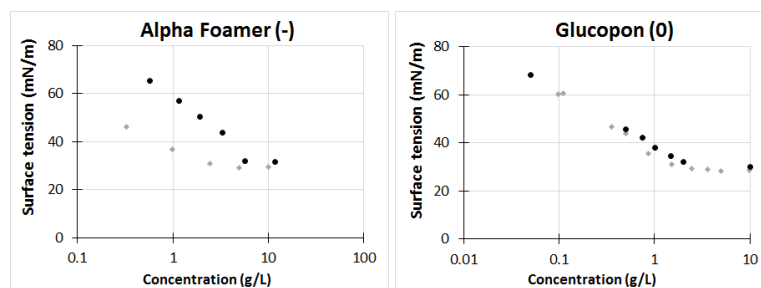


Figure 2.11: Comparison on surface tension curves of Alpha Foamer and Glucopon in distilled water and synthetic cement pore solution. Black dots refer to surface tension measurements in water and grey diamonds, in synthetic cement pore solution.

Surfactant	CMC	CMC*
Alpha Foamer (-)	6 g/L	2.5 g/L
Glucopon (0)	2 g/L	1.5 g/L

Table 2.5: CMC in distilled water and CMC* in synthetic cement pore solution. Values give weight of the surfactants as sold by the providers.

Surfactants in cement paste

Adsorption, contact angle and yield stress results are given for Alpha Foamer and Glucopon in Fig. 2.12.

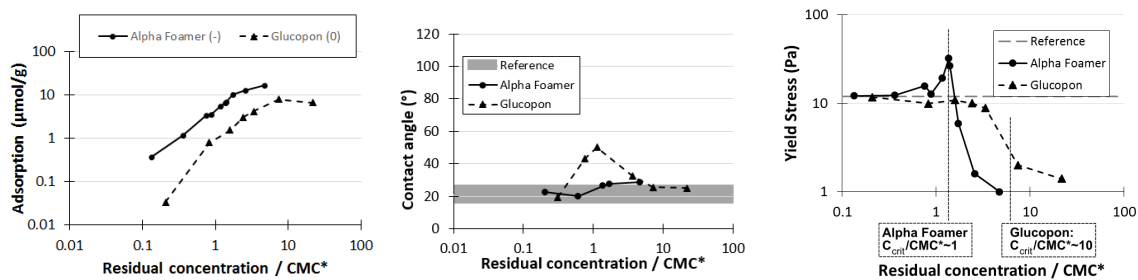


Figure 2.12: Left: Adsorption isotherms of Alpha Foamer (-) and Glucopon (0); on Y-axis, adsorption is given in μmol per gram of cement and on X-axis, residual concentration is divided by the CMC* in synthetic cement pore solution (see table 2.5). Center: Contact angle of cement surface after surfactant adsorption. Right: Yield stress of cement pastes containing surfactant.

Results for Alpha Foamer are very similar to other anionic surfactants. It has a strong affinity onto cement grains surfaces. Adsorption isotherms reaches a plateau value close to 10 μmol per gram of cement when residual concentration overcomes the CMC*. Effect on contact angle is minor, but large increase of yield stress appears before the CMC* and yield stress drop after CMC* is noticeable.

Glucopon exhibits a more complex behavior. It is non-ionic and is not expected to adsorb on cement grains, though, large adsorption amount have been measured, as well as change of contact angle and a yield stress drop at high surfactant concentration. In addition, adsorption plateau and yield stress drop occur at residual concentration $C_{Crit} \sim 10CMC^*$. Studies on molecules similar to Glucopon showed that the micelles can be negatively charged [36]. We can therefore assume that individual molecules are not charged and hardly adsorb onto cement surface, whereas micelles adsorb. Second hypothesis is that molecules become charged in highly alkaline solution and that the high value of C_{Crit} is a consequence of the fact that Glucopon is a mix of different molecules. Indeed, if molecules have different affinity from cement grains and different CMC*, some of them can adsorb on cement grains and form agglomerates while the others remain in solution, which makes the residual concentration higher than if only high-affinity molecules were present.

Appendix 2B: Compatibility with calcium hydroxide solution

Table 2.6 gives foamability results including surfactants studied in Appendix A. In addition to compatibility with synthetic cement pore solution, effect of a calcium hydroxide solution at 0.85 g/L has been studied.

Surfactant		Precipitation in...		Foam in...		
		Ca(OH) ₂	cement sol.	water	Ca(OH) ₂	cement sol.
+	TTAB	No	No	+++	++	++
+/-	Betain	No	No	++	0	0
-	SDS	No	YES	+++	++	0
	Steol 270	No	No	+++	+++	+++
	Bio-Terge	No	No	+++	+++	+++
	Alpha Foamer	No	No	+++	+++	++
0	Triton X100	No	No	++	++	++
	Brij 700	No	No	+	+	0
	Tween 20	YES	YES	+	0	0
	Glucopon	No	No	+++	+++	+++
				0 : No foam + : Foam volume below 20 mL ++ : moderately stable foam +++ : Tube filled with 40 mL foam for longer than 1h		

Table 2.6: Results of foaming tests in synthetic cement pore solution and calcium hydroxide solution.

Effect of Ca(OH)₂ solution is the same as synthetic cement pore solution for all surfactants but SDS, which does not precipitate in calcium hydroxide. SDS precipitation in cement pore solution is therefore not caused by complexation with calcium ions. Additional tests for SDS at 10 g/L in solutions containing only some of the constituents of a synthetic cement pore solution have been carried out.

- 7.12 g/L of KOH
- 1.72 g/L of CaSO₄ · 2H₂O, 6.959 g/L of Na₂SO₄ and 4.757 g/L of K₂SO₄
- 1.72 g/L of CaSO₄ · 2H₂O and 6.959 g/L of Na₂SO₄

We note that in all three cases, precipitation occurs.

Appendix 2C: Delay of hydration

Method

Effect of surfactants on cement paste setting time is assessed by monitoring temperature in the samples with a thermocouple. Samples are casted in 2.8 cm diameter 5.5 cm high cylinder and are thermally insulated. Initial temperature is about 25°. For all samples, temperature is constant for some hours, then it increases, reaches a maximal value around 32° and finally decreases down to the initial value. Setting time is the time between the start of the temperature measurement and the peak.

Results

Results are presented in Fig. 2.13 for TTAB (+), Steol and Bio-Terge (-) and Triton and Glucopon (0). Setting time for reference sample with no surfactant is 12 h.

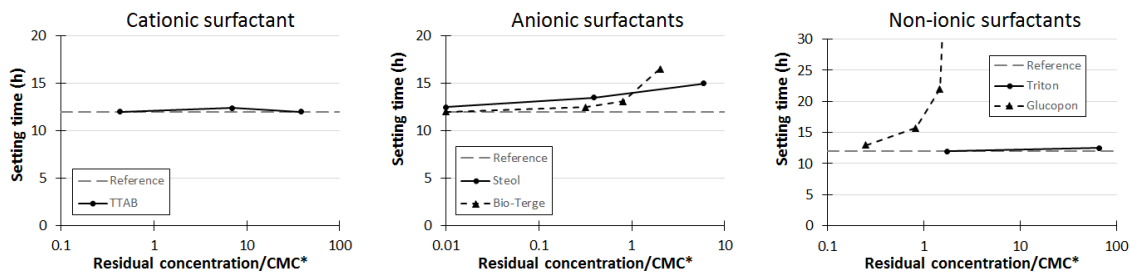


Figure 2.13: Effect of surfactants on cement paste setting time.

TTAB and Triton, i.e. the surfactants which have low or no affinity to cement grains have no effect on setting time. Both anionic surfactant delay slightly hydration. We can compare this retarding effect for similar observations made with several superplasticizers. The reasons why superplasticizer tend to delay hydration are not fully understood. First proposed mechanism is the complexation with calcium ions. In addition, coverage of cement grains due to adsorption prevents the dissolution of ions and the nucleation of hydrates on the solid surfaces [13]. Glucopon strongly delays hydration. At the highest added amount, cement paste does not harden three days after casting. The structure of Glucopon hydrophilic head is similar to sugars, which are known as efficient retarders for cement setting [13].

Chapter 3

Yield stress of aerated cement paste

Sommaire

3.1 Introduction	63
3.2 Materials and methods	65
3.2.1 Materials	65
3.2.2 Method	65
3.2.2.1 Preparation of aerated and reference cement paste	65
3.2.2.2 Foam generation	66
3.2.2.3 Samples	67
3.2.2.4 Yield stress measurement	67
3.3 Results	68
3.3.1 Reference yield stress	68
3.3.2 Aerated cement paste	69
3.4 Discussion	70
3.4.1 Reference yield stress with surfactant	70
3.4.1.1 Reference yield stress with TTAB	71
3.4.1.2 Reference yield stress with Bio-Terge	72
3.4.2 Dimensionless yield stress	72
3.4.3 Bare bubbles (TTAB)	73
3.4.4 Particle covered bubbles	75
3.5 Conclusion	77
Bibliography	80

3.1 Introduction

Yield stress of a cement paste, mortar or concrete is a crucial property. For instance, sufficient yield stress can stop bleeding [1]. When material is poured in a formwork, yield

stress can have negative effects when it prevents proper filling of the mold [1] but it helps to reduce the lateral formwork pressure [2]. In the case of sprayed mortar, yield stress dictates the maximum thickness of the sprayed layer [3].

Among cementitious materials, aerated materials raise growing interest. Entrainment of air bubbles into concrete, up to 10% by volume, is known to improve its durability in environments exposed to freeze-thaw cycles [4]. At higher air content, aerated construction materials are promising for various industrial applications thanks to their low densities, low raw material needs, and improved thermal and acoustic properties.

The goal of this paper is to understand the effect of air bubbles on the yield stress of cement pastes containing air below 40% by volume. These materials will be referred to as "aerated cement paste" or "bubbles suspensions in cement paste" as the word "foams" usually refers to materials with higher air volume content, above 64% [5], where bubbles are densely packed and deformed by their neighbors. In foams, bubble interactions enhance the rheological properties, therefore the results described in this paper are not applicable.

Various observations have been reported in the literature concerning aerated cement pastes or mortars. *Aïtcin* [4] notes that entrained bubbles improve workability of concrete whereas *Rixom and Mailvaganam* [6] reports a large increase of viscosity with the amount of entrained air. These opposite results may arise from the different experimental protocols and the different paste formulations. To quantify the effect of air inclusions on the cement paste yield stress independently from the paste composition, we study the yield stress of the aerated material, τ_y , normalized by the yield stress of the suspending paste τ_{ref} . Micromechanical analysis shows that the normalized yield stress is a function of air volume content Φ and of the ability of the suspending fluid to deform the bubbles [7, 8]. Deformability of the bubbles can be characterized by the Bingham capillary number Ca_y , which compares the suspending fluid yield stress τ_{ref} and the bubble capillary pressure $2\gamma/R$:

$$Ca_y = \frac{\tau_{ref}}{2\gamma/R} \quad (3.1)$$

where γ is the air-liquid surface tension and R is the bubble radius. These curves have been confirmed experimentally when $Ca_y \rightarrow \infty$ and $Ca_y \rightarrow 0$ [9] for model yield stress fluids.

In the case of aerated cement paste, comparison with the theoretical model requires an accurate determination of the yield stress τ_{ref} of the suspending paste. Indeed, this yield stress depends on the water-to-cement ratio [10] and is affected by the presence of additives, for instance water reducing agents.

In this study we prepare aerated cement paste by incorporating a precursor aqueous foam, stabilized by surfactant molecules, into a cement paste. Consequences of addition of aqueous foam into cement paste is an increase of water-to-cement ratio and possible interaction between surfactant and cement. We will first study how these two effects af-

fect τ_{ref} . Afterwards, we will focus on dimensionless yield stress of aerated cement paste $\tau_y(\Phi)/\tau_{ref}$ for two types of surfactant.

3.2 Materials and methods

3.2.1 Materials

We use a CEM I cement from Lafarge, Saint Vigor. Specific surface area is $0.359 \text{ m}^2/\text{g}$ and chemical composition is given in Table 3.1.

C_3S	C_2S	C_3A	C_4AF	CaO/SiO_2	Al_2O_3
62.0%	16.0%	2.1%	15.2%	3	4%
MgO	$\text{Na}_2\text{O} + 0.658 \text{ K}_2\text{O}$	SO_3	Gypsum	L.O.I.	
1.1%	0.34 %	2.58 %	2.4%	0.9%	

Table 3.1: Chemical composition of CEM I cement from Lafarge, Saint-Vigor

Surfactants are TTAB and Bio-Terge[®]. TTAB (tetradecyltrimethylammonium bromide) is a cationic surfactant provided by Sigma-Aldrich, its molar mass is 336 g/mol. Bio-Terge[®] is an anionic surfactant provided by Stepan, its molar mass is 315 g/mol. Chemical formulas for both molecules are given in Fig. 3.1.

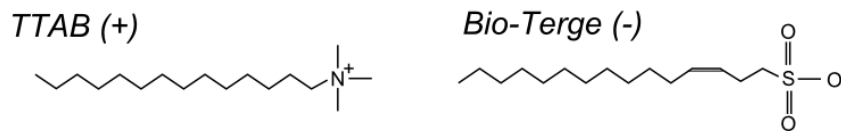


Figure 3.1: Chemical formulas of studied surfactants (reproduced from [11])

Cement and both surfactants are the same as in reference [11].

3.2.2 Method

3.2.2.1 Preparation of aerated and reference cement paste

As the yield stress of cementitious material depends on their history, the same time schedule has been followed for all the samples. It is given in Table 3.2.

Reference samples have been made with no foam. In these cases, the same procedure was followed and surfactant solution was added 28 minutes after addition of cement to mixing water.

We measure the weight of added foam in cement paste. Amount of water added to the cement paste with the foam is then taken into account to calculate the final water-to-cement ratio W/C_f of the aerated paste. Final air content Φ is assessed by weighting the aerated paste in the rheometer cup. By weighting reference samples, whose density can

0:00	Addition of cement to water; water to cement ratio is W/C_i
0:30 - 1:00	Mixing of the paste 200 rpm
1:00 - 1:30	Mixing of the paste 800 rpm
1:30 - 3:30	Mixing of the paste 2000 rpm
21:00 - 21:30	Mixing of the paste 2000 rpm
24:00 - 28:30	Addition of foam on cement paste
29:00 - 30:30	Careful mixing of cement paste and foam by hand
30:30 - 31:30	Filling rheometer cup
31:30	Start of rheometer sequence

Table 3.2: Sample preparation protocol

be calculated from the water-to-cement ratio, we note that the maximum error between theoretical and measured density was 4%. Therefore, we can assume that maximal error on Φ is 4%.

Note that in the chosen procedure, foam or surfactant solution is added more than 20 minutes after first mixing of cement and water so that surfactant cannot interfere in the formation of first hydration products [12].

3.2.2.2 Foam generation

Aqueous foam is generated with the device schematized in Fig. 3.2. Bubbles are created with a small T junction with two inputs: surfactant solution and nitrogen. Bubble diameter depends on the size of the T junction and the flow rates of liquid and gas. All the bubbles are the same size for each sample. After generation, bubbles are collected in a column and foam is wetted from the top to prevent it from drying and breaking.

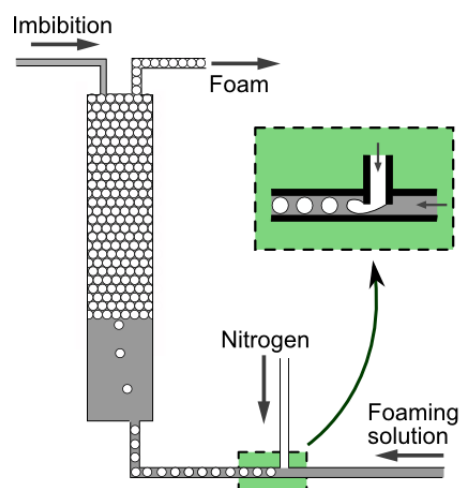


Figure 3.2: Foam generation. All the bubbles are the same size and are generated by small T junction through with constant rates of surfactant solution and nitrogen flow.

Once foam is ready to use, it is pushed from the column at constant flow rate.

3.2.2.3 Samples

We study seven sets of samples. For each of them, water-to-cement ratio before addition of foam, and foam characteristics (surfactant and bubble size) are kept constant.

	Surfactant	Surfactant concentration	Bubble diameter	Initial W/C
Set T1	TTAB	4.5 g/L	475 +/- 10 μm	0.382
Set T2	TTAB	4.5 g/L	270 μm	0.335
Set T3	TTAB	4.5 g/L	475 +/- 10 μm	0.325
Set T4	TTAB	4.5 g/L	475 +/- 10 μm	0.305
Set T5	TTAB	4.5 g/L	780 +/- 20 μm	0.335
Set B1	Bio-Terge	30 g/L	440 +/- 5 μm	0.329
Set B2	Bio-Terge	8 g/L	590 +/- 10 μm	0.335

Table 3.3: Characteristics of each set of experiments on bubble suspension in cement paste

Sets of reference samples are prepared to match with each set of bubble suspensions. Their properties are given in Table 3. Same reference data R_T2 is used for T2 and T5 sets. In addition, reference set R_0 refers to yield stress measurement on pastes where no surfactant solution is added.

	Surfactant	Surfactant concentration	Initial W/C
Reference set R_0	-	-	0.305 to 0.405
Reference set R_T1	TTAB	4.5 g/L	0.382
Reference set R_T2	TTAB	4.5 g/L	0.335
Reference set R_T3	TTAB	4.5 g/L	0.325
Reference set R_T4	TTAB	4.5 g/L	0.305
Reference set R_B1	Bio-Terge	30 g/L	0.329
Reference set R_B2	Bio-Terge	8 g/L	0.335

Table 3.4: Characteristics of each set of experiments on reference cement paste

3.2.2.4 Yield stress measurement

Yield stress measurement are carried out with a vane-in-cup geometry in Ultra+ Kinexus Rheometer from Malvern. The six-blade vane tool is 5 cm high and 25 mm wide. We use striated cup to avoid wall slip, diameter is 37 mm and height 62.5 mm. Rheometer cup is filled with aerated or non-aerated cement paste with a spoon, then vane tool is slowly inserted in the paste. No pre-shear is carried out prior to yield stress measurement. This method is chosen to avoid material flow before the measurement in order to prevent bubble migration due to shear rate heterogeneities [13] and gravity. Indeed, bubble rise

in sheared yield stress fluid [14] and particle migration to low shear rate zones [2, 13] are phenomena which are known to lead to distorted rheological measurements.

Yield stress is measured with a start of flow sequence: shear rate is constant and equal to 0.01 s^{-1} for 10 minutes. This shear rate value was chosen by *Mahaut et al.* [15] to measure the yield stress of particle suspension in cement paste. For all the samples, stress increases up to the yield stress and then decreases. Maximum is reached when shear strain of the sample is between 40 and 45%. Ovarlez et al. [16] showed that this value is low enough to enable correct measurement of yield stress with a vane tool.

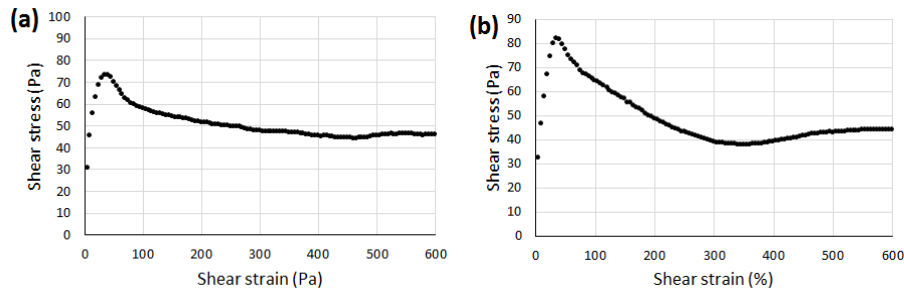


Figure 3.3: Start of flow curves for yield stress measurement of an aerated cement paste (a) and the corresponding reference paste (b). Examples are from set T3 with air content 31% and set R_T3.

3.3 Results

3.3.1 Reference yield stress

Yield stresses for reference samples are plotted in Fig. 3.4. As expected, when no surfactant is added (crosses on the graph), yield stress decreases when water-to-cement ratio increases. For each reference data set containing surfactant, yield stress decreases when the amount of added TTAB solution increases. Same trend is observed with Bio-Terge solution at the smaller concentration (R_B2), even if the decrease is smaller than for TTAB. On the contrary, when 30 g/L Bio-Terge surfactant solution is used (R_B1), yield stress increases with added solution amount.

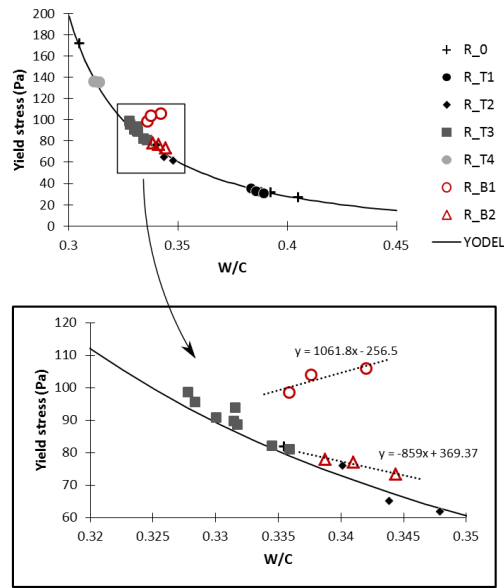


Figure 3.4: Yield stress of cement paste without air. Final water-to-cement ratio is calculated from both initial water and added surfactant solution. Yield stresses for pastes with no surfactant (R_0) or TTAB surfactant (R_T1 to R_T4) are fitted with equation (1) with $\Phi_{perc} = 0.32$, $\Phi_{max} = 0.545$ and $m_1 = 65 \text{ Pa}$. In the case of Bio-Terge surfactant, linear regressions for each set of data are plotted with dotted lines

3.3.2 Aerated cement paste

Yield stresses measured for each data set at different air contents are given in Figs. 3.5 and 3.6.

Evolution of yield stress with increasing foam content is not the same for all data sets: it is constant in set T1, it decreases in sets T2 to T5 and increases for B1 and B2.

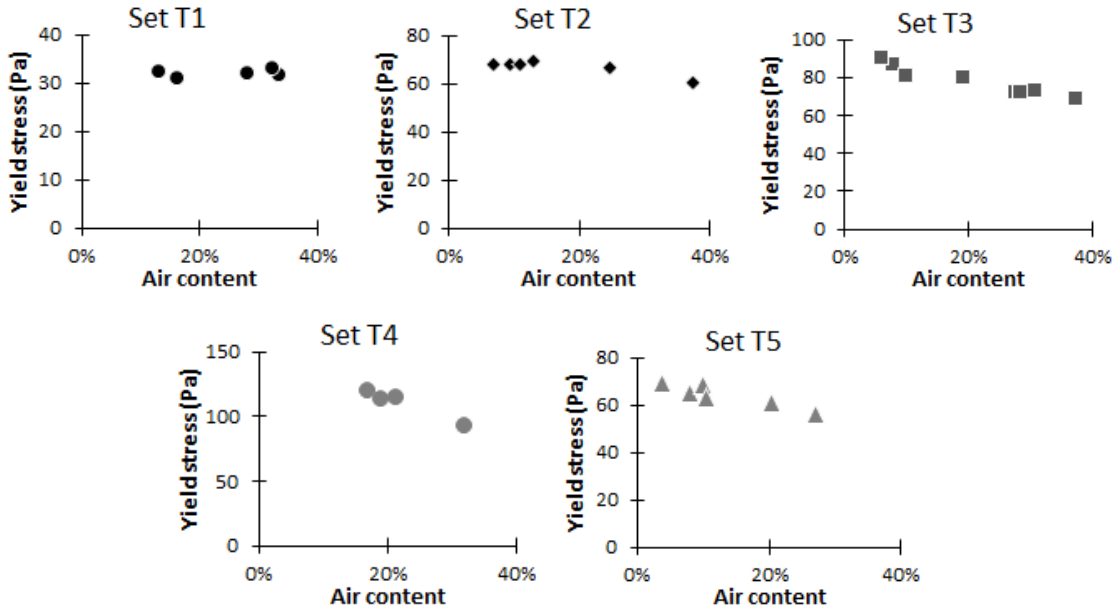


Figure 3.5: Yield stresses of cement pastes mixed with TTAB foams. Bubble diameter is $475 \mu\text{m}$ for T1, T3 and T4, $270 \mu\text{m}$ for T2 and $780 \mu\text{m}$ for T5. Initial water-to-cement ratio is 0.382 for T1, 0.335 for T2 and T5, 0.325 for T3 and 0.305 for T4.

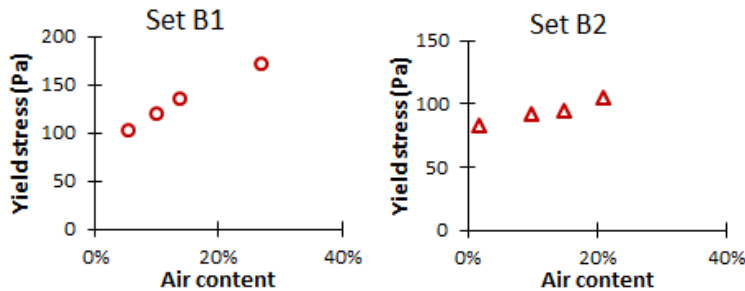


Figure 3.6: Yield stresses of cement pastes mixed with Bio-Terge foams. Bubble diameter is $440 \mu\text{m}$ for B1 and $590 \mu\text{m}$ for B2. Initial water-to-cement ratio is 0.329 for B1 and 0.335 for B2.

3.4 Discussion

3.4.1 Reference yield stress with surfactant

We showed in a previous study that ionic surfactants, mainly anionic, can strongly affect yield stress when they are added to a cement paste (see chapter 2 [11]). At low concentration, adsorbed surfactant monolayer tends to make the cement grain surface hydrophobic and creates hydrophobic attraction between cement grains. At macroscopic scale, increase of yield stress has been measured. At high surfactant concentration, surfactant agglomeration on the solid surfaces leads to steric repulsion between cement grains and a drop of the paste yield stress. In Fig. 3.7, yield stress for cement paste containing TTAB and Bio-Terge are given as a function of surfactant concentration for cement pastes at $W/C_f = 0.5$ prepared as in reference [11]. Even if W/C is not the same in the present study, we can

use these curves to estimate the concentration regime for both surfactants.

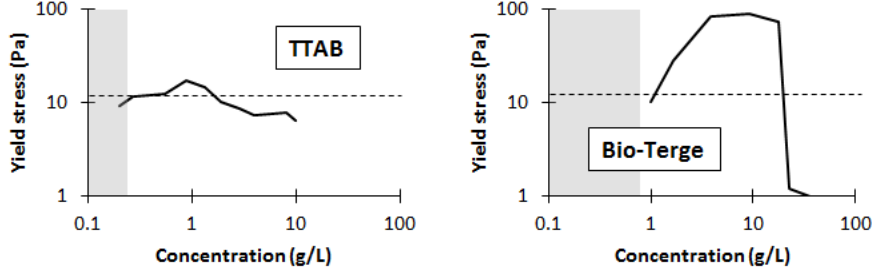


Figure 3.7: Effect of surfactant concentration on the yield stress of cement pastes at $W/C_f = 0.5$ prepared following the protocol described in [11]. Dotted line shows yield stress of the paste with no surfactant (12 Pa). Grey areas show the surfactant concentrations used in the present chapter.

Let us calculate the final surfactant concentrations $C_{TA,f}$ after mixing foam and cement paste. They depend on the concentration in the foaming solution $C_{TA,i}$, on the initial water-to-cement ratio of precursor cement paste W/C_i and the final water-to-cement ratio W/C_f .

$$C_{TA,f} = C_{TA,i} \frac{W/C_f - W/C_i}{W/C_f} \quad (3.2)$$

Surfactant concentrations range from 0.03 to 0.2 g/L for samples containing TTAB and between 0.08 and 0.8 g/L for Bio-Terge. We can see in Fig. 3.7 that for both surfactants, these concentrations well below the concentrations at which maximum yield stresses are expected. Surfactants are therefore in the low concentration regime, where yield stress can be enhanced by hydrophobic interactions, but due to the very low concentrations used, we can expect this effect to be minor. Further analysis is made below for each surfactant.

3.4.1.1 Reference yield stress with TTAB

In Fig. 3.4, all reference yield stresses, when no surfactant is added or when TTAB is added, seem to follow a single curve. First of all, this shows that TTAB, at the concentrations we use here, has no effect on yield stress. In addition, yield stress depends only on the water content of the cement paste, including both initial mixing water and foaming solution added later.

We choose to fit TTAB reference curve with equation 3.3 from the Yodel [10]:

$$\tau_{ref} = m_1 \frac{\Phi_p^2 (\Phi_p - \Phi_{perc})}{\Phi_{max} (\Phi_{max} - \Phi_p)} \quad (3.3)$$

In this equation, m_1 accounts for the intensity of the interactions between cement grains, whose major components are Van der Waals, electrostatic and steric forces [10]. Φ_p is the solid volume fraction and is related to the water-to-cement ratio and to the densities of water ρ_w and cement ρ_c :

$$\Phi_p = 1/(1 + \rho_c/\rho_w W/C) \quad (3.4)$$

Φ_{perc} is the percolation threshold, Φ_{max} is the maximal solid fraction .

This curve is shown in Figure 4 by a solid line with parameters $\Phi_{perc} = 0.32$, $\Phi_{max} = 0.545$ and $m_1 = 65 \text{ Pa}$.

3.4.1.2 Reference yield stress with Bio-Terge

When Bio-Terge solution is added to cement paste, yield stress is higher than for samples containing TTAB or no surfactant at the same water-to-cement ratio. In fact, addition of Bio-Terge solutions into cement pastes has two consequences: solid fraction Φ_p decreases and the intensity of of the attractive forces between cement grains increases. Therefore, reference yield stress τ_{ref} cannot be fitted by an equation like 3.3. We choose to use linear regressions:

$$\tau_{ref} = 1062 W/C - 257 \text{ for experiment set B1} \quad (3.5)$$

$$\tau_{ref} = 369 - 859 W/C \text{ for experiment set B2} \quad (3.6)$$

3.4.2 Dimensionless yield stress

Results normalized with reference yield stresses from equations 3.3, 3.6 and 3.6 are shown in Fig. 3.8.

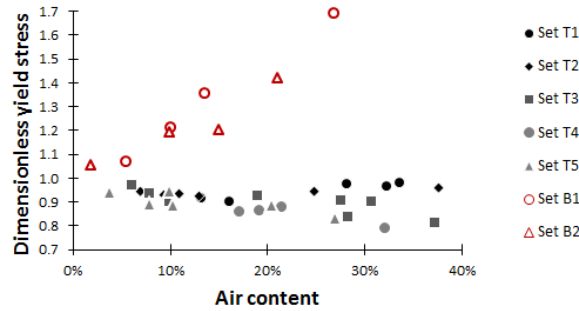


Figure 3.8: Dimensionless yield stress for all samples. For samples made with TTAB, bubble diameter is $475 \mu\text{m}$ for T1, T3 and T4, $270 \mu\text{m}$ for T2 and $780 \mu\text{m}$ for T5; initial water-to-cement ratio is 0.382 for T1, 0.335 for T2 and T5, 0.325 for T3 and 0.305 for T4. For samples made with Bio-Terge, bubble diameter is $440 \mu\text{m}$ for B1 and $590 \mu\text{m}$ for B2. Initial water-to-cement ratio is 0.329 for B1 and 0.335 for B2.

The dimensionless yield stresses of bubble suspensions in cement paste exhibit different behaviors depending on the surfactant. In the case of cationic surfactant TTAB, it is smaller than 1, that is to say that addition of air inclusions reduce the yield stress. On the other hand, in the case of Bio-Terge (anionic), air inclusions enhance yield stress.

Observation of bubbles shows that bubble surface aspect is very different in the TTAB and Bio-Terge samples. In Fig. 3.9, picture on the right shows that bubbles in Bio-Terge sample are covered with a layer of cement grains. We can see that as bubbles rise in the paste, the grain layer cracks. On the contrary, no layer of cement grain is visible around the bubbles stabilized by TTAB (Fig. 3.9, left). Observation of bubbles in samples containing TTAB is difficult because they tend to break as soon as they reach the sample surface. On the contrary, in samples from set B1, only few bubbles break.

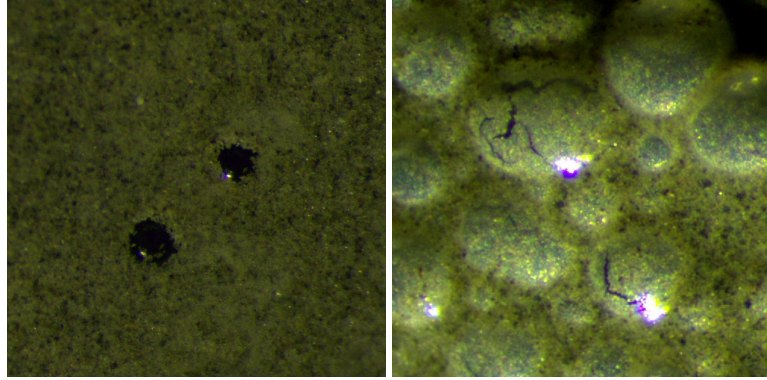


Figure 3.9: Left: sample from set T1 containing TTAB. Right: sample from set B1 containing Bio-Terge. Note that bubbles tend to break rapidly when exposed to air, especially for samples containing TTAB, so that the number of the bubbles on each picture is not representative of the air content. Width for each image is 1.5 mm.

The different effect of bubble incorporation on cement paste yield stress is presumably related to the different aspects of bubble surface. In the following we compare the dimensionless yield stress with theoretical models for each of the surfactants.

3.4.3 Bare bubbles (TTAB)

In order to compare TTAB data sets with the micromechanical model from [7, 8], we need to calculate the capillary numbers $Ca_y = \tau_{y,ref}R/(2\gamma)$. As mentioned previously, reference yield stress $\tau_{y,ref}$ decreases with increasing liquid content as shown by equation 3.3. Besides, at low surfactant concentration, surface tension γ decreases when concentration increases. Its variation for cement paste interstitial fluid containing TTAB is reported in [11] and illustrated in Fig. 3.10 as a function of TTAB residual concentration C_{res} , i.e. concentration of TTAB molecules in solution. In concentration range 0.02-0.2 g/L, we can assume, for γ in mN/m and C_{res} in g/L that $\gamma = 31 - 6.8 * \ln(C_{res})$.

We assume that the amount of adsorbed TTAB molecules is small compared to the residual molecules in solution, so $C_{res} \approx C_{CA,f}$. Therefore, Bingham capillary numbers for each set of results are given in Table 3.5.

Theoretical dimensionless yield stress for non-deformable bubbles $Ca_y \rightarrow 0$, is indicated by a full line in Fig. 3.11 and is given by [7, 8]:

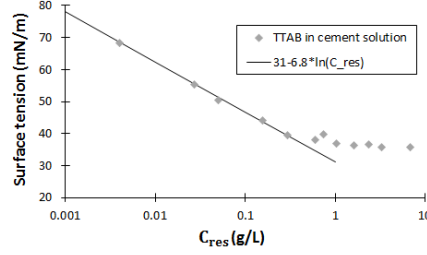


Figure 3.10: Surface tension of TTAB solution in cement paste interstitial fluid used to calculate Bingham capillary numbers. Grey dots are measurements taken from [11].

Set	Ca_y
T1	0.08
T2	0.10
T3	0.21 - 0.23
T4	0.34 - 0.36
T5	0.28 - 0.30

Table 3.5: Bingham capillary numbers for experiments with TTAB

$$\tau_y/\tau_{ref} = \sqrt{(1 - \Phi) \frac{5 + 3\Phi}{5 - 2\Phi}} \text{ when } Ca_y \rightarrow 0 \quad (3.7)$$

When the bubble are fully deformable ($Ca_y \rightarrow \infty$), the relation becomes:

$$\tau_y/\tau_{ref} = \sqrt{(1 - \Phi) \frac{3 - 3\Phi}{3 + \Phi}} \text{ when } Ca_y \rightarrow \infty \quad (3.8)$$

This is shown by the dotted line in Fig. 3.11.

Both curves have also been obtained experimentally for bubble suspensions in a model yield stress fluid (concentrated oil-in-water emulsion) by *Ducloué et al.* [9]. Experimental results fitted with equation 3.7 for $0.0069 \leq Ca_y \leq 0.11$ and with equation 3.8 for $Ca_y = 0.57$.

In Fig. 3.11, dimensionless yield stress results of aerated cement paste with TTAB have been plotted and can be compared with both theoretical curves.

At low air content, dimensionless yield stresses obtained from our measurement seems to tend toward a value smaller than 1. This behavior must be an experimental artifact and shows that despite all our effort to keep the same preparation protocol for aerated and reference samples, shearing of the paste during hand mixing may be influenced by the presence of bubbles.

However, all the results are located as expected between the two theoretical curves. Moreover, dimensionless yield stress depends only on the capillary number (it does not depend on the reference yield stress or the bubble size) as sets T1 and T2 follow the same curve, and sets T4 and T5 are very close. This can be seen mainly at high air content. The higher the capillary number, the lower the dimensionless yield stress.

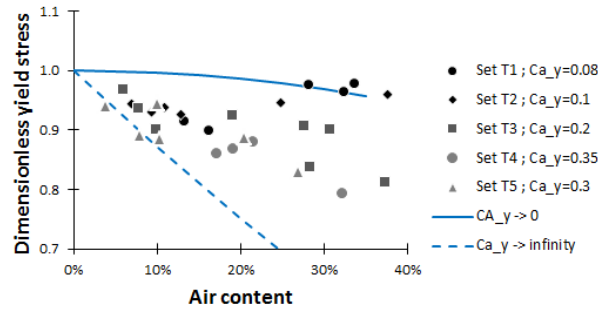


Figure 3.11: Dimensionless yield stress for samples made with TTAB. Theoretical curves, which have been observed experimentally on model yield stress fluid by Ducloué [17], are indicated for non-deformable bubbles (full line) and fully deformable bubbles (dotted line).

3.4.4 Particle covered bubbles

Surface tension of Bio-Terge in interstitial solution of cement paste can be approximated by 30 mN/m if $C_{res} > 0.3$ and $18 - 12 \ln(C_{res})$ at lower concentrations (see Fig. 3.12).

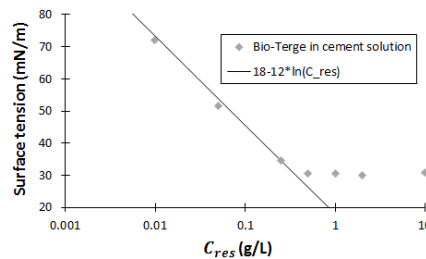


Figure 3.12: Surface tension of Bio-Terge solution in cement paste interstitial fluid used to calculate capillary numbers. Grey dots are measurements taken from [11].

Bingham capillary numbers calculated following the same method as for TTAB are between 0.32 and 0.38 for B1 and between 0.24 and 0.30 for B2. Note that the assumption $C_{res} \approx C_{f,TA}$ may not be valid for Bio-Terge because of its high affinity to cement grain surface. We probably overestimate of C_{res} and thus overestimate the capillary numbers. However, the values are the same order of magnitude as the capillary numbers calculated for TTAB. Thus, the specific behavior of Bio-Terge bubbles cannot be related to the capillary number.

The particle layer on the bubble surface suggests that the behavior in the case of Bio-Terge lies in the modified surface properties of the bubbles. Particle covered interfaces have first been reported by Ramsden [18] and Pickering [19]. Afterwards, particles covered films, bubbles and foams have raised a lot of attention due to their increased life time compared to surfactant stabilized systems [20, 21, 22, 23, 24]. First requirement to allow solid particle adsorption at air-water or oil-water interface is that the particles must be partially hydrophobic. Then, the elastostic barrier to particle adsorption must be low enough [25].

Increase of contact angle of water on cement grains has been observed in the presence of low amount of Bio-Terge, so that we can assume that the first point is fulfilled. Cement grains have size comprised between a few and 100 μm with average value close to 10 μm [15]. Due to their irregular shape, radius of curvature of the edges is several orders of magnitude below the grain size [26], which decreases the adsorption barrier [25]. In addition, cement solution contains a high concentration of dissolved ions [12], and this high electrolyte content is known to reduce electrostatic repulsion between charged particles and interface, which also reduces the adsorption barrier [25]. All these aspects show that cement particles covered by a monolayer of Bio-Terge molecules are good candidates to adsorb at air-water interfaces.

Once partially hydrophobic solid particles are adsorbed at interfaces, energy required to remove them is very high. Desorption energy E_{Des} for spheres is given by the formula [27]:

$$E_{Des} = \gamma a^2 \pi (1 - |\cos \theta|)^2 \quad (3.9)$$

Where a is the radius of the particles and θ the contact angle. Note that in the case of irregularly shaped particles, desorption energy is higher than in the case of spheres because anisotropic particles tend to settle at the interface with the orientation which maximizes the desorption energy [28]. In the case of cement, calculation with $\pi\gamma \sim 100 \text{ mN/m}$ and $a \sim 10 \mu\text{m}$ gives $E_{Des} \sim 10^{-11} \text{ J}$ if $\theta=90^\circ$ and $E_{Des} \sim 10^{-12} \text{ J}$ if $\theta=60^\circ$.

To evaluate if shearing of the cement paste can desorb the cement grains, we can compare this value to the shear energy. For simple shear, energy per unit volume is $\tau \cdot \epsilon$, where the shear stress τ is of the order of magnitude of the yield stress $\tau_{y,ref} \sim 100 \text{ Pa}$ and the deformation ϵ is about 1 in our experiments. Integration on the particle volume a^3 gives $E_{shear} \sim 10^{-13} \text{ J}$.

Therefore, the Bio-Terge covered cement grains cannot not desorb from bubbles surface during yield stress measurement.

To understand the effect of the cement particle shell on the grain surface, we can compare Bio-Terge results with dimensionless yield stress of solid particle suspensions in cement paste. Procedure followed for the tests is the same as described in paragraph 3.2.2.1; at 27 minutes after preparation of the cement paste, we added to the paste 500 μm diameter polystyrene beads or 2 mm diameter glass beads. These additional samples contain no surfactant, so reference yield stress is given by equation 3.3.

Like for bubbles, micromechanical analysis provides a theoretical curve for undeformable solid particles. This theoretical analysis requires that the yield stress fluid is continuous and homogeneous compared to the beads. In the case of cement paste, this means that the beads must be much bigger than the cement grains. Moreover, it assumes no slip condition at the bead surface [7]. Dimensionless yield stress of a bead suspension in a yield stress fluid is :

$$\tau_y / \tau_{ref} = \sqrt{\frac{(1 - \Phi)}{(1 - \Phi / \Phi_m)^{2.5\Phi_m}}} \quad (3.10)$$

where Φ_m is the maximal packing fraction of the beads when material is sheared. This curve has been experimentally validated in model yield stress materials [13] and in cement paste [15]. Φ_m value measured in cement paste is 0.56. In Fig. 3.13, our experimental results for Bio-Terge bubbles and for beads can be compared with the bead theoretical curve.

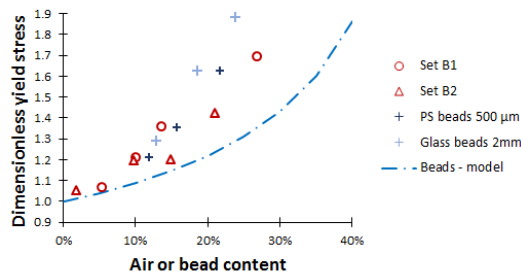


Figure 3.13: Dimensionless yield stress for samples made with Bio-Terge. Dotted line correspond to the theoretical curve for a suspension of solid spheres with maximal solid fraction 0.56. Crosses correspond to measurements carried out with 500 μm polystyrene beads or 2 mm glass beads.

Similarly to the theoretical curve, our bead experimental results show that dimensionless yield stress increases when the volume fraction of inclusions increases. In addition, no dependence on the bead size can be seen. However, experimental points are above the expected values. This must be related to our experimental method and the difficulty to follow accurately the same protocol for cement paste with and without inclusions.

No major effect of Bio-Terge concentration is observed on the dimensionless yield stress. During preparation however, we note incorporating aqueous foam in cement paste was more difficult for B2 measurements, where Bio-Terge concentration is lower, because the bubbles tend to break during hand mixing.

The main observation is that Bio-Terge data points coincide with experimental measurements with polystyrene and glass beads. That is to say that the armored bubbles behave like solid inclusions. Our hypothesis is that adsorbed particles provide to the bubbles a surface solid layer with roughness which prevents the slipping of the continuous phase during shearing.

Striking point is that the armored bubbles behave like indeformable objects, even if Bingham capillary number the Bio-Terge sets of experiments are below 0.38, a value corresponding to partially deformable bubbles in the case of TTAB. Evaluation of deformability by Bingham capillary number may not be relevant in the case of armored bubbles because the adsorbed particle layer increases the surface elasticity of the bubbles [24] which opposes deformation.

3.5 Conclusion

We have investigated the effect of added bubbles of chosen size on the yield stress of aerated cement paste. Bubbles are stabilized with two surfactants, which are known to have

different affinities to cement grains.

Behavior of the bubbles is strongly affected by the surfactant. When surfactant has low affinity to cement grains, dimensionless yield stress depends on Bingham capillary number, which accounts for the deformability of the bubbles. While non-deformable bubbles ($Ca_y \sim 0.1$) do not change the yield stress, dimensionless yield stress decreases with air volume content for deformable bubbles ($Ca_y \gtrsim 0.2$).

Totally different behavior is observed when surfactant adsorbs on cement grains. Effect of bubbles is comparable to solid inclusions, and no effect of bubble size and surfactant amount can be seen. We attribute this effect to the irreversible adsorption of hydrobobic cement particles at the bubbles surface which change the surface properties of the bubbles.

Bibliography

- [1] N. Massoussi, E. Keita, and N. Roussel, “The heterogeneous nature of bleeding in cement pastes,” *Cement and Concrete Research*, vol. 95, pp. 108–116, 2017. [63](#), [64](#)
- [2] G. Ovarlez, F. Bertrand, and S. Rodts, “Local determination of the constitutive law of a dense suspension of noncolloidal particles through magnetic resonance imaging,” *Journal of Rheology*, vol. 50, pp. 259–292, 2006. [64](#), [68](#)
- [3] F. Gorlier, Y. Khidas, and O. Pitois, “Yielding of complex liquid foams,” *Journal of Rheology*, vol. 61, pp. 919–930, 2017. [64](#)
- [4] P.-C. Aïtcin, “Entrained air in concrete: rheology and freezing resistance,” in *Science and Technology of Concrete Admixtures* (P.-C. Aïtcin and R. J. Flatt, eds.), pp. 87–95, Woodhead publishing, 2016. [64](#)
- [5] I. Cantat, S. Cohen-Addad, F. Elias, F. Graner, R. Höhler, O. Pitois, F. Rouyer, and A. Saint-Jalmes, *Foams - Structure and dynamics*. Oxford University Press, 2013. [64](#)
- [6] R. Rixom and N. Mailvaganam, *Chemical Admixtures for Concrete*. E. & F.N. Spon Ltd, 3rd ed. ed., 1999. p106+. [64](#)
- [7] X. Chateau, G. Ovarlez, and K. Trung, “Homogenization approach to the behavior of suspensions of noncolloidal particles in yield stress fluids,” *Journal of rheology*, vol. 52, no. 2, pp. 489–506, 2008. [64](#), [73](#), [76](#)
- [8] T. L. Nguyen Thi, L. Ducloué, G. Ovarlez, and X. Chateau, “Rhéologie des suspensions de bulles dans un fluide à seuil,” in *21ème Congrès Français de Mécanique*, (Bordeaux, France), August 2013. [64](#), [73](#)
- [9] L. Ducloué, O. Pitois, J. Goyon, X. Chateau, and G. Ovarlez, “Rheological behaviour of suspensions of bubbles in yield stress fluids,” *Journal of Non-Newtonian Fluid Mechanics*, vol. 215, pp. 31–39, 2015. [64](#), [74](#)

- [10] R. J. Flatt and P. Bowen, “Yodel: a yield stress model for suspensions,” *Journal of the American Ceramic Society*, vol. 89, no. 4, pp. 1244–1256, 2006. [64](#), [71](#)
- [11] B. Feneuil, O. Pitois, and N. Roussel, “Effect of surfactants on the yield stress of cement paste,” *Cement and Concrete Research*, vol. 100, pp. 32–39, 2017. [65](#), [70](#), [71](#), [73](#), [74](#), [75](#)
- [12] H. Bessaies-Bey, *Polymères et propriétés rhéologiques d'une pâte de ciment : une approche physique générique*. PhD thesis, Université Paris-Est - SIE, 2015. [66](#), [76](#)
- [13] F. Mahaut, X. Chateau, P. Coussot, and G. Ovarlez, “Yield stress and elastic modulus of suspensions of non-colloidal particles in yield stress fluids,” *Journal of Rheology*, vol. 52, pp. 287–313, 2008. [67](#), [68](#), [77](#)
- [14] J. Goyon, F. Bertrand, O. Pitois, and G. Ovarlez, “Shear induced drainage in foamy yield-stress fluids,” *Physical Review Letters*, vol. 104, p. 128301, 2010. [68](#)
- [15] F. Mahaut, S. Mokéddem, X. Chateau, N. Roussel, and G. Ovarlez, “Effect of coarse particle volume fraction on the yield stress and thixotropy of cementitious materials,” *Cement and Concrete Research*, vol. 38, pp. 1276–1285, 2008. [68](#), [76](#), [77](#)
- [16] G. Ovarlez, F. Mahaut, F. Bertrand, and X. Chateau, “Flows and heterogeneities with a vane tool: Magnetic resonance imaging measurements,” *Journal of rheology*, vol. 55, pp. 197–223, 2011. [68](#)
- [17] L. Ducloué, *Comportement rhéologique des fluides à seuil aérés*. PhD thesis, Université Paris Est, 2014. [75](#)
- [18] W. Ramsden, “Separation of solids in the surface-layers of solutions and ‘suspensions’ - preliminary account,” *Proceedings of the Royal Society of London*, vol. 72, pp. 156–164, 1904. [75](#)
- [19] S. U. Pickering, “Emulsions,” *Journal of Chemical Society*, vol. 91, pp. 2001–2021, 1907. [75](#)
- [20] B. P. Binks, “Particles as surfactants - similarities and differences,” *Current Opinion in Colloid & Interface Science*, vol. 7, pp. 21–41, 2002. [75](#)
- [21] M. Abkarian, A. B. Subramaniam, S.-H. Kim, R. Larsen, S.-M. Yang, , and H. A. Stone, “Dissolution arrest and stability of armored bubbles,” *Physical Review Letters*, vol. 99, p. 188301, 2006. [75](#)
- [22] O. Pitois, M. Buisson, and X. Chateau, “On the collapse pressure of armored bubbles and drops,” *European Physical Journal E*, vol. 38, p. 48, 2015. [75](#)
- [23] N. Taccoen, F. Lequeux, D. Z. Gunes, and C. N. Baroud, “Probing the mechanical strength of an armored bubble and its implication to particle-stabilized foams,” *Physical Review X*, vol. 6, no. 1, p. 011010, 2016. [75](#)

- [24] A. Stocco, E. Rio, B. Binks, and D. Langevin, “Aqueous foams stabilized solely by particles,” *Soft Matter*, vol. 7, no. 4, pp. 1260–1267, 2011. [75](#), [77](#)
- [25] S. Tcholakova, N. D. Denkov, and A. Lips, “Comparison of solid particles, globular proteins and surfactants as emulsifiers,” *Physical Chemistry Chemical Physics*, vol. 10, pp. 1608–1627, 2008. [75](#), [76](#)
- [26] N. Roussel, A. Lemaître, R. J. Flatt., and P. Coussot, “Steady state flow of cement suspensions: A micromechanical state of the art.,” *Cement and Concrete Research*, vol. 40, pp. 77–84, 2010. [76](#)
- [27] N. D. Denkov, I. B. Ivanov, and P. A. Kralchevski, “A possible mechanism of stabilization of emulsions by solid particles,” *Journal of Colloids and Interface Science*, vol. 150, no. 2, pp. 589–593, 1992. [76](#)
- [28] N. Ballard and S. A. F. Bon, “Equilibrium orientations of non-spherical and chemically anisotropic particles at liquid-liquid interfaces and the effect on emulsion stability,” *Journal of Colloid and Interface Science*, vol. 448, pp. 533–544, 2015. [76](#)

Chapter 4

Optimal cement paste yield stress for the production of stable cement foams

Sommaire

4.1 Introduction	82
4.2 Materials and methods	83
4.2.1 Materials	83
4.2.2 Methods	84
4.2.2.1 Protocol	84
4.2.2.2 Precursor foam	84
4.2.2.3 Mixing	84
4.2.2.4 Final stability	85
4.2.2.5 Rheological measurement	86
4.2.2.6 Water suction out of the cement pastes	86
4.2.3 Cement paste yield stress	86
4.3 Results	88
4.3.1 Stability	88
4.3.2 Rheological measurements	90
4.3.2.1 Foam yield stress	90
4.3.2.2 Elasticity	90
4.3.3 Water suction	91
4.4 Discussion	92
4.4.1 Comparison with aqueous foams	92
4.4.2 Early age rheological properties	93
4.4.3 Time evolution of rheological properties	95
4.4.4 Stability loss at very high surfactant content	97
4.5 Conclusion	98

4.1 Introduction

Cement foams are highly porous materials which offer interesting thermal insulation properties. When cement foam density decreases, thermal resistance is improved but mechanical strength decreases [1]. Control of bubble morphology is a crucial issue to optimize all macroscopic properties at a given density. For example, bubble size and pore connections are control parameters for acoustic absorption [2] and flow permeability [3].

Several foam production methods have been reported in the literature, including chemical foaming, air entrainment and mixing with aqueous precursor foam. In the precursor foam method, cement slurry and aqueous foam are prepared separately before being mixed together. Resulting cement foam morphology depends on (1) the precursor foam morphology, (2) the capacity of the mixing process to preserve the precursor foam bubble sizes and (3) the bubble size evolution in the sample at rest until cement hydration. Third point is challenging. As long as the material embedding the bubbles is not solid, foam destabilization occurs through three mechanisms [4]: drainage is caused by specific gravity difference between air bubbles and cement paste, ripening is a gas transfer from smaller bubbles to bigger bubbles, and coalescence refers to thin film breakage between two neighbor bubbles. Both drainage and ripening are affected by the consistency of the suspending fluid. Promising method to stop or slow them down is to increase the fluid yield stress in order to counteract bubble rise and deformation processes [5, 6, 7].

In the case of cement foams, yield stress results from attractive interaction between cement grains. It depends on both the intensity of these interparticle forces and the particle volume content [8]. Particle volume content is related to the water-to-cement ratio and interparticle forces can be tuned by additives. For instance, superplasticizers adsorb on cement grains, which causes steric repulsion between cement grains and decrease of yield stress [9]. In a cement foam made from precursor aqueous foam, surfactants are needed to reduce air-fluid surface tension and stabilize the films separating the bubbles. Some of them, mainly anionic surfactants, have been shown to have a strong affinity towards cement grains and change the yield stress (see chapter 2 [10]). When they are added in small amount in cement paste, adsorbed molecules form an hydrophobic layer on cement grains. Resulting hydrophobic attraction between cement grains leads to an increase of the macroscopic yield stress. On the other hand, when large amount of anionic surfactant is added to cement paste, surfactant molecules agglomerate into micelles on cement grains surface and leads to steric repulsion and a strong decrease of yield stress.

In this paper we investigate the effect of yield stress on the stability of cement foams. Yield stress is controlled by using additives, either superplasticizer or large amount of anionic surfactant. Additionally, in order to assess the rheological behavior of the cement paste as confined between the bubbles, we perform rheological measurements on cement foams.

4.2 Materials and methods

4.2.1 Materials

Cement is a CEM I from Lafarge, from Lagerdorf factory. Specific surface provided by the manufacturer is $0.433 \text{ m}^2/\text{g}$. Chemical composition is given in table 4.1.

C ₃ S	C ₂ S	C ₃ A	C ₄ AF	CaO/SiO ₂	MgO	Na ₂ O +0.658 K ₂ O	SO ₃	Gypsum
60%	13%	2%	13%	3	0.8%	0.5 %	2.5%	4%

Table 4.1: Chemical composition of CEM I cement from Lafarge, Lagerdorf

Two different surfactants are used. Steol[®] 270 CIT is an anionic surfactant provided by Stepan. Its molar mass indicated by the manufacturer is 382 g/mol and active content 68-72%. Steol Critical Micelle Concentration (CMC) is 1.5 g/L in water and 0.3 g/L in cement pore solution [10]. Triton[™] X-100 (laboratory grade) is a non-ionic surfactant provided by Sigma-Aldrich; molar mass is 625 g/mol and CMC is 0.2 g/L in water and 0.15 g/L in cement pore solution.

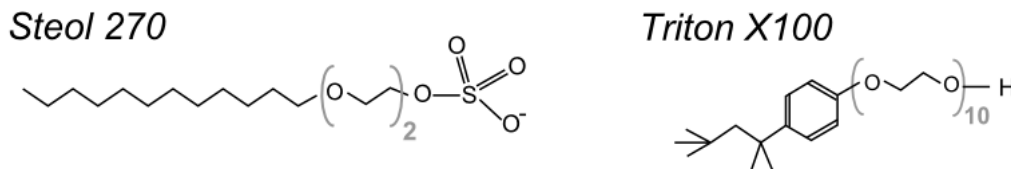


Figure 4.1: Chemical formula of surfactants : Steol is anionic and Triton is non-ionic

When added into cement paste, Steol 270 has a strong affinity with cement grains surface [10] and can either increase the cement paste yield stress at low concentration or act as a deflocculant at high concentration. On the contrary, non-ionic Triton has very low affinity with cement grains [10, 11] and does not change the yield stress.

SIKA Tempo 12 superplasticizer has been used to modify cement paste yield stress in cement foam samples containing non-ionic surfactant. It has been checked that Tempo 12 does not alter stability of aqueous foam made with Triton: we have compared the foam volume obtained by shaking tubes containing a Triton solution with and without superplasticizer. Details about the experimental method can be found in [10]. Results are not shown here.

In paragraph 4.2.3, we give the yield stress of cement paste containing either Steol 270 or Superplasticizer and Triton, prepared with the same protocol as the cement foam described in paragraph 4.2.2.1.

4.2.2 Methods

4.2.2.1 Protocol

In order to remove any effect of cement paste age on results, all cement foams are prepared following the same time schedule, from initial water and cement mixing to sample casting or rheometry measurement.

Water is mixed with cement paste at initial water-to-cement ratio $W/C_i=0.35$ or 0.32 and then left at rest for 20 minutes to allow the formation of sulfo-aluminate phases. Then, a deflocculant is added. Deflocculant is either Steol surfactant added in large quantity or SIKA Tempo 12 superplasticizer. Cement paste is then mixed with precursor foam. This procedure is schematized in Fig. 4.2.

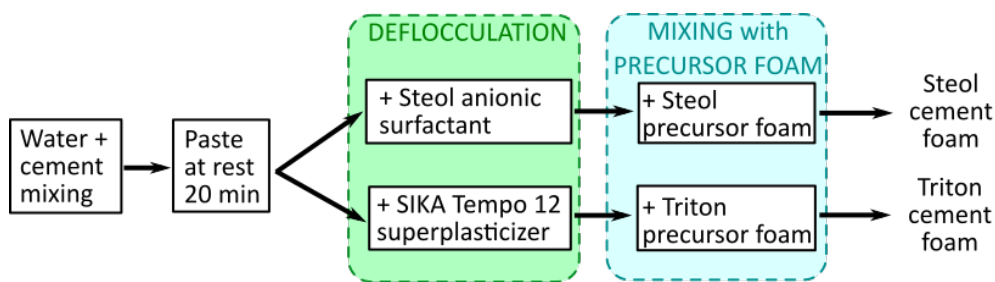


Figure 4.2: Preparation protocol of cement foams made with Steol anionic surfactant and Triton non-ionic surfactant.

4.2.2.2 Precursor foam

Precursor aqueous foam generator is schematized in figure 4.3. Nitrogen and surfactant solution (concentration 1 g/L for both surfactants) flow in T-junction. Characteristic length of the T-junction is $l_T = 100 \mu\text{m}$. The capillary pressure P_C depends on the gas-liquid surface tension $\gamma \sim 10 \text{ mN/m}$ and is $P_C \sim \gamma/l_T \sim 10^2 \text{ Pa}$. The hydrostatic pressure P_H depends on the liquid density $\rho_{liq} \sim 1000 \text{ kg/m}^3$: $P_H = \rho_{liq} g l_T \sim 1 \text{ Pa}$. Therefore, as $P_C \gg P_H$, capillary effects dominate gravity effects, and liquid and gas pass alternately, which leads to the formation of bubbles. Bubble diameter depends on the flow rates of surfactant solution and nitrogen respectively, and on the T junction size.

Then, created bubbles are collected in a vertical column. Imbibition flow at the foam top compensates liquid loss due to drainage and is used to tune the precursor foam liquid fraction. Precursor foam is mixed with cement paste about 40 minutes after the beginning of the generation, when ripening has not started to occur in the column.

Bubble radius for all precursor foams is $R = 390 \pm 20 \mu\text{m}$ and liquid fraction $1.4 \pm 0.1\%$.

4.2.2.3 Mixing

To mix precursor foam and cement paste, we use a convergent mixing device schematized in Fig. 4.3, right. Cement paste flows in a conic tube, which length is $L = 4 \text{ cm}$, smaller diameter at cone exit 2 mm and cone angle 3° . Then, mixing of paste and precursor foam

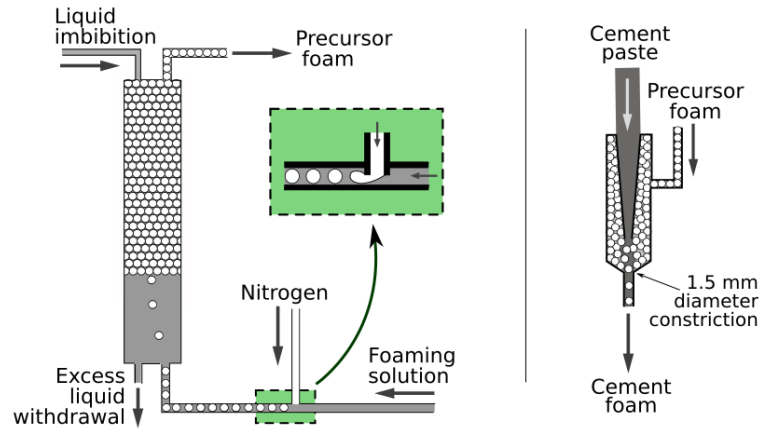


Figure 4.3: Schema of precursor foam generation (left) and mixing device (right)

takes place thanks to a 1.5 mm diameter constriction. Input flow rates are chosen so that final air content is $\Phi = 83\% \pm 1\%$. Note that this mixing method involves the flow of the precursor cement paste in small tubes, which requires moderate cement paste yield stress (below a few 10 Pa). For each cement foam sample, we first fill the rheometer cup for yield stress or elasticity measurement and then a mold for stability assessment.

4.2.2.4 Final stability

Samples are casted in 6 cm high 2.6 cm-diameter air-tight plastic cylinders. We checked that foams do no break when they are in contact with the mold walls. Samples are demolded 7 days after casting. Cement foam stability is visually assessed and samples are classified within the five categories illustrated in Fig. 4.4:

- 3: fully stable sample
- 2: large stable area
- 1: small stable area(s)
- 0: no stable area
- -1: sample collapse



Figure 4.4: Example of samples illustrating each stability class. Sample height is 6 cm.

It can be noted that the final stability is the result of many competing phenomena including the intrinsic stability of the foam and the time during which the foam is exposed to destabilisation. This time relates to the setting time of the system.

4.2.2.5 Rheological measurement

To measure rheological properties of cement foams, we use stress controlled Kinexus Ultra+ rheometer from Malvern with a Vane geometry. Cup is striated to avoid wall-slip, height is 6 cm and diameter 37 mm. Six-blade Vane tool is 5 cm high and 25 mm large. Each measurement sequence starts with stress relaxation during 30 s. Then, either yield stress is measured with a start of flow curve at flow rate $\dot{\epsilon} = 0.01 \text{ s}^{-1}$, or elastic modulus is monitored with 10^{-5} amplitude oscillations at 1 Hz.

In the elastic regime, energy balance shows that local deformation ϵ_l in the foam skeleton is related to the macroscopic deformation ϵ by the relation $\epsilon_l = \epsilon\sqrt{1-\Phi}$ [12] where Φ is the volume air content. Therefore, local strain amplitude during elastic measurements is $4 \cdot 10^{-6}$. This value is well below both critical strains related to flocculation and formation of CSH bridges between cement grains [13]. Therefore, we expect that elasticity measurement does not affect material thixotropic behavior and is, as such, a non-destructive measurement.

4.2.2.6 Water suction out of the cement pastes

Cement paste containing surfactant (and superplasticizer in the case of Triton) are prepared as described in paragraph 4.2.2.1, but here only surfactant solution at 1 g/L is added instead of foam. We call free cement paste this bulk paste whose composition is expected to be the same as the foam interstitial paste.

We measure free cement paste ability to release water with the experimental device schematized in Fig. 4.5. A 1.6-cm thick layer of cement paste containing Steol surfactant is placed on one side of a U-shaped tube filled with water. A filter (0.45 μm) separates the cement paste and the tube. It can be crossed by the water but not by the cement grains. Surface of water in the other branch of the tube is free to move. When the cement paste is raised above the free water surface at height h , pressure difference $\Delta P = \rho_{liq}gh$ is created at the bottom of the cement paste. Volume of extracted water can then be deduced from the displacement of the free water surface. Note that h decreases during the time of the experiment because water extraction makes the free water surface rise. For each experiment, pressure is $\Delta P_0 = 440 \text{ Pa}$ and decreases to a value comprised between 400 and 375 Pa after 10 minutes. The value chosen for ΔP_0 accounts for the hydrostatic pressure in the continuous phase in the 6-cm high foam samples which varies between 0 and 600 Pa.

4.2.3 Cement paste yield stress

In the following we will correlate the foam properties with the yield stress of the free cement paste. To measure free cement paste yield stress, paste is poured on a flat surface

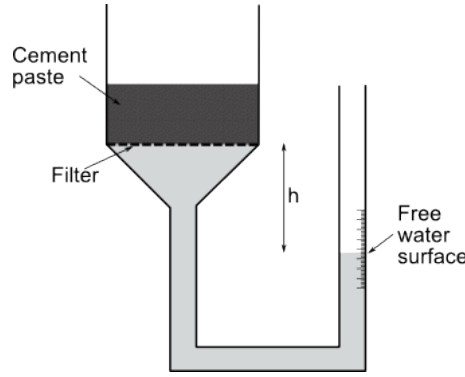


Figure 4.5: Experimental device used to measure the water volume extracted from the free cement pastes at $\Delta P \approx 440$ Pa.

and average radius R_{spread} is measured. Yield stress τ_y is then obtained from the paste density ρ and the poured volume Ω with the following formula [14]:

$$\tau_y = \frac{225\rho g\Omega^2}{128\pi^2 R_{spread}^5} \quad (4.1)$$

Equation 4.1 is valid at intermediate yield stress values. On the one hand, it must be high compared to capillary forces and on the other hand, the spread height h_{spread} must be small compared to the radius. As already discussed in [10], capillary forces can be neglected when yield stress is above 1 Pa. We choose to set all the values measured below 1 Pa to 1 Pa. Regarding the second condition, maximal measured value is $\tau_y \approx 100$ Pa, in this case, if poured volume is 30 mL, we obtain $R_{spread}/h_{spread} \approx 3$.

Measured free cement paste yield stresses are given in figure 4.6. Two water-to-cement ratios $W/C_f = 0.38$ and 0.41 have been studied in the case of Steol surfactant whereas only $W/C_f = 0.36$ has been considered in the case of Tempo 12 and Triton mixes.

Exponential fit correlates well with each of the curves. Therefore, in the following, we will use equations 4.2, 4.3 and 4.4 to estimate the free cement paste yield stress τ_y from the Steol or Tempo 12 concentrations C_{Steol} or $C_{Tempo 12}$ (with yield stresses in Pa and concentrations in g/L):

$$\tau_y = 6.87 \cdot 10^9 e^{-1.89 C_{Steol}} \quad \text{with Steol and } W/C_f=0.41 \quad (4.2)$$

$$\tau_y = 8.30 \cdot 10^{12} e^{-1.97 C_{Steol}} \quad \text{with Steol and } W/C_f=0.38 \quad (4.3)$$

$$\tau_y = 137 e^{-0.191 C_{Tempo 12}} \quad \text{with Tempo 12 and Triton} \quad (4.4)$$

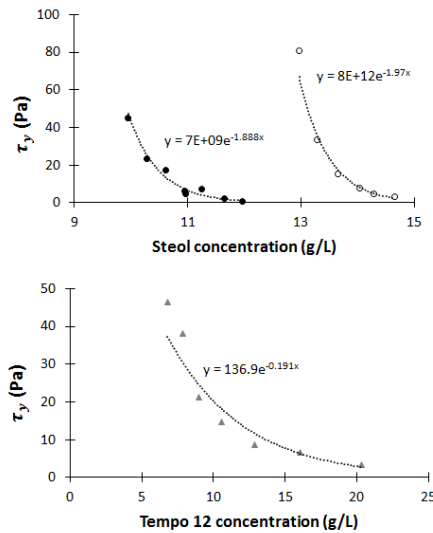


Figure 4.6: Yield stress of cement pastes prepared following the same protocol as cement foam. Top: pastes containing Steol anionic surfactant with $W/C_f=0.38$ (empty dots) and $W/C_f =0.41$ (full dots). Bottom: superplasticizer and Triton non-ionic surfactant with $W/C_f =0.36$.

4.3 Results

4.3.1 Stability

Fig. 4.7 illustrates a typical evolution of the morphology of an unstable foam with time. Pictures of the sample are taken through the transparent mold. Cement paste appears in light grey whereas air voids are black. Note that we can see only the morphology of the side of the sample against the mold walls, where the movement of the bubbles deposes a cement layer. Therefore, the apparent morphology after foam destabilization may not be representative of the bulk morphology of the foam. However, we can neatly see that major change of the foam structure takes place before 30 min after sample preparation.

The stability of cement foams samples containing either anionic or non-ionic surfactant is plotted in figure 4.8 as a function of the yield stress of the corresponding free cement paste.

In all cases, best foam stability is obtained at moderately low free cement paste yield stress. On the one hand, foams are unstable at high τ_y , i.e. above a critical value $\tau_y^* \simeq 10$ Pa. Increase of free yield stress above τ_y^* leads consistently to unstable foams. This behavior is particularly noticeable in Tempo 12 - Triton foams, where foam collapse was observed for yield stress close to 25 Pa. On the other hand, very low free yield stress values, below $\tau_y^{**} \simeq 2$ Pa also lead to unstable foams. In this very low yield stress regime, reproductibility of the results is poor, foams with the same formulation can sometimes have different stability behavior.

These stability results are unexpected, because, as mentioned before, high interstitial yield stress is expected to contribute to stopping drainage and ripening. These puzzling results can be due to several effects including:

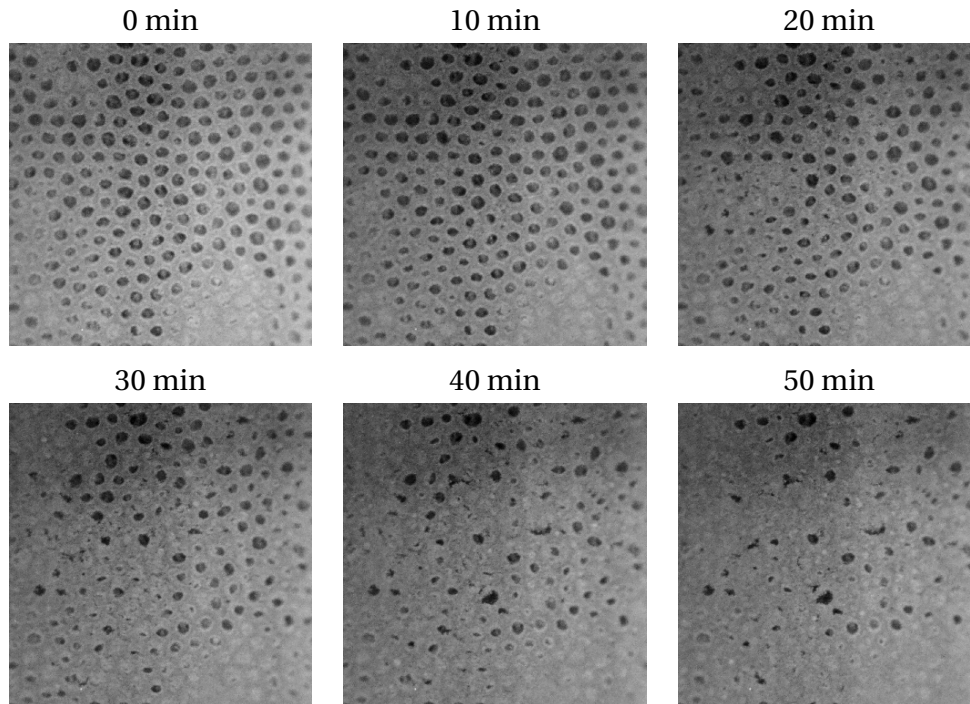


Figure 4.7: Example of the evolution of the morphology of an unstable cement foam ($W/C_f = 0.41$, 10.2 g/L of Steol, $\tau_y = 18 \text{ Pa}$). Foam on the pictures is seen through the transparent mold ; note that the movement of the bubbles deposes a cement layer on the mold walls and that apparent morphology after foam destabilization may not be representative of the bulk morphology of the foam. Cement paste is in light grey and bubbles are black. Picture width is 1 cm.

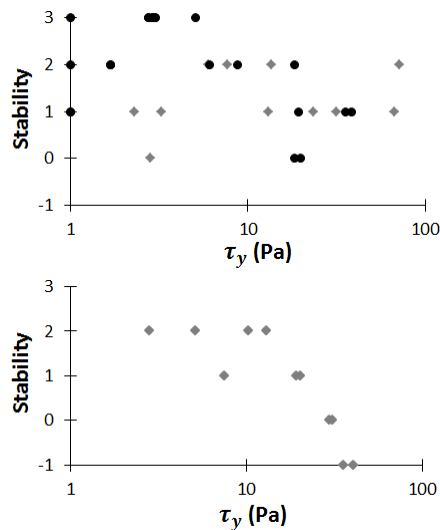


Figure 4.8: Top: Stability of cement foams containing Steol anionic surfactant. Grey diamonds correspond to foams made with initial $W/C_f=0.38$ and black dots to foams with $W/C_f=0.41$. Bottom: Stability of cement foams containing superplasticizer and Triton.

- The cement paste inside the foam structure may have different behavior than the free cement paste.

- Time related effects, i.e. thixotropy and hydration kinetics, may play a dominant role.
- Segregation of water and cement grains and water in the foam may occur.

Rheological investigation will be used to elucidate the first two points. Yield stress measurement at foam early age is used to assess the behavior of the interstitial cement paste. Then, as a non-destructive measurement, elastic modulus is monitored to evaluate the evolution of the paste rheological properties with time.

Segregation of water and cement grains are then measured by the water suction experiment.

4.3.2 Rheological measurements

4.3.2.1 Foam yield stress

We notice that two types of start-of-flow curve shape of fresh cement foams were obtained. For some samples, the stress increases up to a plateau value. For other samples, plateau value is lower than the yield stress and the curve exhibits an overshoot. In both cases, yield stress $\tau_{y,foam}$ is obtained for deformation between 40 and 75%. Examples for both curve shapes are shown in figure 4.9.

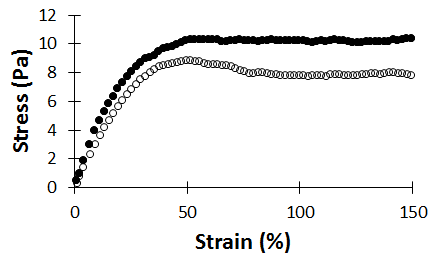


Figure 4.9: Examples of the two types of start-of-flow curves. Both curves were obtained for samples with $W/C_f=0.41$, for two different Steol concentrations. Curve with overshoot (empty circles) is obtained with 11.4 g/L of Steol and $\tau_y = 3$ Pa, and curve without overshoot (black dots), with 10.4 g/L of Steol and $\tau_y = 18$ Pa.

$\tau_{y,foam}$ for all the samples are plotted as a function of the yield stress of the free cement paste in figure 4.10. Presence of overshoot is indicated by empty dots and diamonds.

For the three sets of results, $\tau_{y,foam}$ increases with τ_y but foam yield stress variation is limited: while τ_y ranges from about 1 to 100 Pa, $5.7 \text{ Pa} \leq \tau_{y,foam} \leq 14 \text{ Pa}$. Besides, overshoot occurs when $\tau_y \leq \tau_y^*$.

4.3.2.2 Elasticity

Two different types of elastic modulus evolution are shown in figure 4.11. Curve slope can either be constant during 50 min or decrease with time.

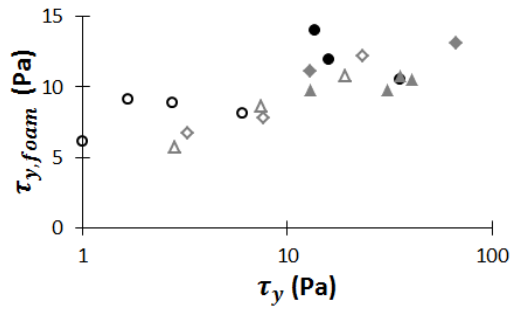


Figure 4.10: Macroscopic yield stress of fresh cement foam. Black dots refer to cement pastes containing anionic surfactant at $W/C_f = 0.41$ and grey diamonds at $W/C_f = 0.38$. Grey triangles refer to samples with superplasticizer and non-ionic surfactant. Empty symbols refer to curves where an overshoot was measured.

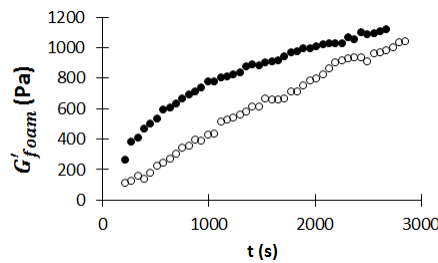


Figure 4.11: Examples of the two possible shapes of elastic modulus curves. Both curves were obtained for samples containing Steol surfactant with $W/C_f=0.41$. Linear curve (empty circles) is obtained with 11.4 g/L of Steol and $\tau_y = 3$ Pa, and non-linear curve (black dots), with 10.4 g/L of Steol and $\tau_y = 18$ Pa.

Elastic modulus at $t=0$ and $t=40$ min are plotted as a function of τ_y in Fig. 4.12. As expected, the higher τ_y , the higher the initial elastic modulus. When free yield stress increases by two decades, elastic modulus is increased by a factor 4. However, 40 minutes after the start of the oscillation test, elastic modulus hardly increases with yield stress anymore.

In addition, foams where G' evolution is linear are shown by empty symbols in Fig. 4.12. We note that for the low free yield stresses, elastic modulus increases linearly with time whereas for the higher free yield stresses, elastic modulus slope decreases.

4.3.3 Water suction

Percentage of extracted water from free cement paste containing Steol whose $W/C_f = 0.41$ are shown on Fig. 4.13. We note that the amount of extracted water decreases when τ_y increases, mainly when $\tau_y > \tau_y^*$

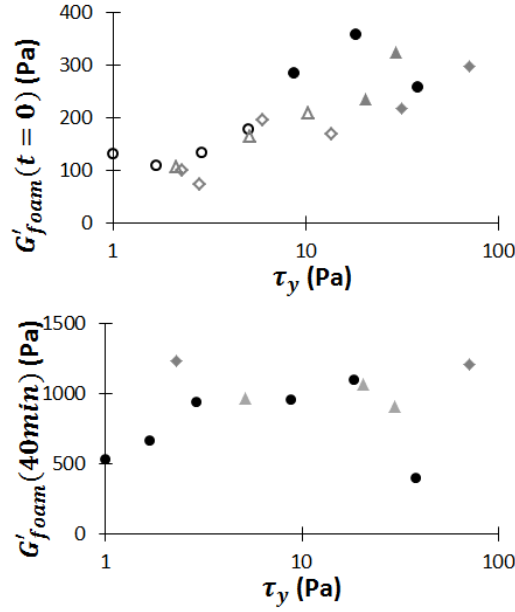


Figure 4.12: Elastic modulus of fresh cement foam at $t=0$ and $t=40$ min. Black dots refer to cement pastes containing anionic surfactant at $W/C_f = 0.41$ and grey diamonds at $W/C_f = 0.38$. Grey triangles refer to samples with superplasticizer and non-ionic surfactant. In first graph, empty symbols refer to linear elastic modulus curves.

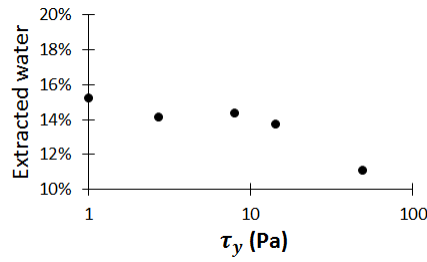


Figure 4.13: Ratio of extracted water from free cement pastes at $W/C_f = 0.41$ containing Steol surfactant after 10 minutes at $\Delta P \approx 400$ Pa

4.4 Discussion

4.4.1 Comparison with aqueous foams

Aqueous foams are known to behave like an elastic solid at small deformations and to exhibit a yield stress at higher deformation. Rheological properties depend on the bubble radius R , the surface tension γ and the air volume content Φ . Yield stress is given by equation 4.5 [15, 16] and elastic modulus by equation 4.6 [4].

$$\tau_{y,aq}(\Phi) = 0.6 \frac{\gamma}{R} (\Phi - \Phi_c)^2 \quad (4.5)$$

$$G'_{aq}(\Phi) = 1.4 \frac{\gamma}{R} \Phi (\Phi - \Phi_c) \quad (4.6)$$

where Φ_c is the critical packing fraction above which there are films between the bubbles and equals 0.64 in the case of disordered monodisperse foam.

Surface tension value depends on the surfactant and its concentration. After incorporation of precursor foam in cement paste, Triton concentration in cement foam is 0.11 g/L. Surface tension of Triton solution in cement pore solution at this concentration is 35 mN/m [10]. Regarding Steol, surface tension in cement pore solution for concentrations above CMC is 27 mN/m [10]. As low yield stress is achieved when anionic surfactant residual concentration is above CMC [10], we can assume that for both surfactants, when cement paste yield stress is the lowest, surface tension is below 35 mN/m.

Therefore, aqueous foam yield stress for both surfactants is $\tau_{y,aq}(83\%) \simeq 2$ Pa and elastic modulus is $G'_{aq}(83\%) \simeq 20$ Pa. Both are below the values measured on the cement foams samples for all τ_y . This means that the interstitial cement paste strongly enhances the foam rheological properties, even when τ_y is very low.

4.4.2 Early age rheological properties

Let us first discuss the fact that in low-yield stress regime, an overshoot appears on the start-of-flow curve. This overshoot is not expected to result directly from thixotropy effects in the cement paste, as they appear only for low yield stress cement paste, that is to say, for the highest concentrations of anionic surfactant or superplasticizer. Indeed, we recall that apparent thixotropy in cement paste arises from two effects: creation of a percolated network of colloidal cement grains during the first seconds after high shear mixing, then nucleation and growth of CSH bond between the grains [13]. Our yield stress measurements are carried out only a few minutes after foam production, so the major contribution to the measured yield stress is the colloidal percolation network. As attraction forces between cement grains are reduced in the presence of high amount of Steol [10] or superplasticizer [9] due to steric repulsion, colloidal network is not expected to be stronger or to form faster in the case of deflocculated pastes.

We stress that start-of-flow curve of granular material exhibits overshoot when grains are densely packed [17, 18]. Moreover, *Gorlier et al.* [19] studied start-of-flow curves of complex fluid foams. They showed that there is no overshoot when interstitial fluid is a simple yield stress fluid (i.e. concentrated emulsion for example), whereas overshoot appears when aqueous foam is mixed with small beads suspension, even if the corresponding unconfined granular suspension does not exhibit yield stress properties; that is to say that yield stress results from the confinement of the beads by the bubbles. Authors analyzed the stresses at stake in the granular foam and concluded that small particles packed in the foam structure behave as dense granular matter.

Yield stress of emulsion foams and small-particle foams can both be fitted by equation 4.7. This equation has been empirically determined for samples where $\tau_{y,int}R/\gamma < 0.5$ [19].

$$\frac{\tau_{y,foam}(\Phi)}{\tau_{y,aq}(\Phi)} = 1 + c(1 - \Phi)^{4/3} \left(\frac{\tau_{y,int}R}{\gamma} \right)^{2/3} \quad (4.7)$$

Where $c = 110$ is a fitting parameter, and $\tau_{y,int}$ is the yield stress of the interstitial fluid. Using equation 4.7, we deduce from foam macroscopic yield stress $\tau_{y,foam}(\Phi)$ (plotted in Fig. 4.10) the yield stress of the interstitial cement paste $\tau_{y,int}$. It is compared in Fig. 4.14 with τ_y , that is to say with the yield stress of the cement paste with the same composition and prepared following the same protocol, but not confined in the foam. This graph shows that when cement paste yield stress is high, above 20 Pa, interstitial yield stress is equal to free paste yield stress. When free yield stress is lower, yield stress is strongly enhanced, up to a factor 10.

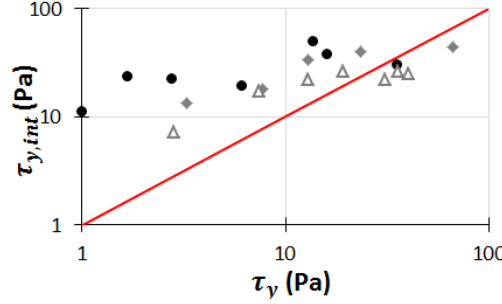


Figure 4.14: Comparison of yield stress of identical cement pastes when they are confined in the foam $\tau_{y,int}$ and with no foam τ_y . Black dots refer to cement pastes containing anionic surfactant at $W/C_f = 0.41$ and grey diamonds at $W/C_f = 0.38$. Grey triangles refer to samples with superplasticizer and non-ionic surfactant.

To summarize, start-of-flow curve shape (Fig. 4.9) and estimations of interstitial yield stress (Fig. 4.14) allow us to identify two cement paste rheological behaviors:

- When $\tau_y > \tau_y^*$, cement paste acts as yield stress fluid because of the high Van der Waals attraction between cement grains and rearrangement of grains cannot occur. Interstitial yield stress is similar to the yield stress of the free cement paste. In this regime, that we call *yield stress regime*, cement foams are unstable within our experimental conditions.
- When $\tau_y < \tau_y^*$, cement paste behaves in part as a confined granular material. An overshoot appears on the start-of-flow curve and interstitial yield stress is significantly increased with respect to free paste yield stress. This regime, that we call *granular regime* because it is reminiscent of the behavior of confined granular packing, allows significant foam stability. The stability loss at the lower free yield stresses will be discussed in part 4.4.4.

In the *granular regime*, the formation of a network of cement grains in contact requires the removal of the excess water from the interstitial cement paste. Let us estimate the amount of water which must be removed. After the mix of cement paste and foam, the maximal water-to-cement ratio is 0.41. Corresponding solid volume content in the cement paste is given by $\phi_p = (1 + \rho_c / \rho_w W/C)^{-1}$; we obtain $\phi_p = 44\%$. Random loose packing fraction is $0.8 * 60\% = 48\%$ [20]; this corresponds to $W/C=0.34$. Water loss is therefore

$(0.48 - 0.44)/0.48 = 8\%$ of the paste volume and less than 2% of the foam volume, which cannot be visually observed with our samples.

Experimental estimation of the water-to-cement ratio 10 min after the foam production is given by the water extraction curve. In graph in Fig. 4.15, we observe that when $\tau_y < \tau_y^*$, W/C reaches nearly 0.35 while it remains above 0.36 in the yield stress regime. This observation tends to confirm that a denser granular network can be set up, thanks to grains rearrangement, when $\tau_y < \tau_y^*$ but not when $\tau_y > \tau_y^*$.

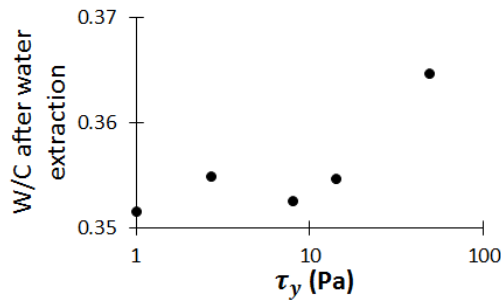


Figure 4.15: Ratio of extracted water from free cement pastes at $W/C_f = 0.41$ containing Steol surfactant after 10 minutes at $\Delta P \approx 400$ Pa

Note that $\tau_{y,int}$ in the *granular regime* is lower than the 120 Pa value obtained for foams made with monodisperse spherical particles [19]. This suggests that the ideal *granular regime* is not fully achieved in cement foams. In fact several effects could be considered for explaining this deviation. (1) The large particle polydispersity in our case with respect to the monodisperse particles assemblies studied in [19]. It has been shown in [19] that confinement effect is strongly dependent on particles size: large ones, i.e. $> 40 \mu\text{m}$, and small ones, i.e. $< 1 \mu\text{m}$, are not expected to contribute to that effect. (2) The effective friction coefficient is $\mu = 0.3$ in the case of solid spheres. The yield stress of a granular material, under confinement pressure P , is given by $\tau_y = \mu P$. Friction coefficient is however not known for polymer (or surfactant) covered cement grains.

Granular effect can account for the increase of yield stress of the interstitial cement paste due to the confinement provided by the bubble interface when $\tau_y < \tau_y^*$. However, interstitial yield stress is still smaller in *granular regime* than in *yield stress regime* and cannot account for the remarkable stability of the foams. One hypothesis to explain this stability is that the time evolution of the interstitial cement paste rheological properties may play a role on foam stability. Therefore, to understand the stability of cement foams, we will focus in the next paragraph on the evolution of the rheological properties upon aging.

4.4.3 Time evolution of rheological properties

Elastic modulus curves allow us to assess the evolution of the interstitial cement paste with time. For foams in the *granular regime*, slope of foam elastic modulus curve is constant. This linear increase at low amplitude oscillations is a typical evolution in cement

pastes and it is known to result from the constant volume formation rate of hydrates between cement grains [13]. In the *yield stress regime*, however, elastic modulus slope becomes smaller with time. We can assume that the slow shearing induced by the bubbles deformation during destabilization leads to a partial rejuvenation of the cement paste and partially compensates the increase of elasticity caused by thixotropy.

Similarly to what we have done with yield stress, we can estimate the interstitial elastic modulus from the measured value of the foam elastic modulus. Foam modulus is the sum of the contribution of aqueous foam G'_{aq} , and a contribution which depends on the interstitial elastic modulus G'_{int} [21, 22] :

$$G'_{foam} = G'_{aq} + G'_{int}(1 - \Phi)^2 \left(1 + 15(2\Phi - 1) \left(\frac{\Upsilon}{RG'_{int}} \right)^{2/3} \right) \quad (4.8)$$

Equations 4.6 and 4.8 allow us to assess G'_{int} at several times. Results are shown in Fig. 4.16 for $t=40$ min.

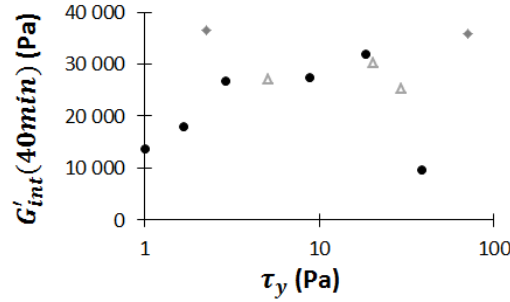


Figure 4.16: Interstitial elastic modulus at time $t=40$ min. Black dots refer to cement pastes containing anionic surfactant at $W/C_f = 0.41$ and grey diamonds at $W/C_f = 0.38$. Grey triangles refer to samples with superplasticizer and non-ionic surfactant.

We see that rigidity increase is faster in the *granular regime* than in the *yield stress regime*. Though, elastic modulus remains higher in most of the colloidal-type foams than in the *granular regime* until 40 minutes. At this time, as shown in Fig. 4.7, ripening has already started to occur in unstable foams. Therefore, the values of interstitial elasticity up to 40 minutes after foam production cannot account for the better stability observed in the *granular regime*.

In order to further investigate the effect of foam aging, we measured the evolution of yield stress with time. Whereas elastic modulus is measured at low deformation, below 0.1%, yield stress is obtained at high shear strain. Therefore, elasticity and yield stress measured in cement paste have different origins [13]: elasticity is caused only by the hydrates bonds between cement grains, whereas yield stress results from both colloidal interaction and hydrate bonds. Second consequence of the high sample deformation during start-of-flow experiment is that this measurement is destructive: yield stress for each age must be measured with a different sample. Each sample is prepared following the same protocol as described in 4.2.2.1 and placed in the rheometer geometry. Then a resting time between 0 and 45 min is chosen before the start of the yield stress measurement.

Measured yield stresses are shown in Fig. 4.17. Curve shape in *yield stress regime* is typical from cement paste [13] and exhibits a two-regime behavior with two different slopes: in the first regime, yield stress is governed by colloidal interaction between cement grains, and in the second regime, formation of hydrates bonds become predominant. For the stable foam in the *granular regime*, very fast increase of yield stress in the first 15 minutes of rest supports the hypothesis of the formation of a dense structure of cement grains in contact. Both interstitial yield stress curves have the same slope after 15 minutes, which shows that there is no major difference of hydration kinetics between these two types of samples.

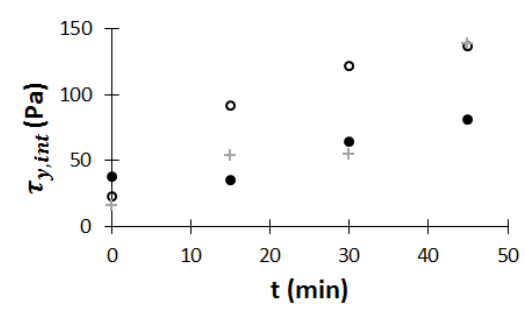


Figure 4.17: Increase of interstitial yield stress with time for cement foams $W/C_i = 0.35$ containing Steol. Full dots to foams in the *yield stress regime* (Steol concentration 10.4 g/L, $\tau_y = 18$ Pa), empty dots refer to very stable foams in the *granular regime* (Steol concentration 11.4 g/L, $\tau_y = 3$ Pa) and grey crosses to less stable foams in the *granular regime* (Steol concentration 12.3 g/L, $\tau_y < 1$ Pa)

We can therefore assume that the origin of stability of cement foams in the *granular regime* lies in the formation of a dense cement grain structure, where dominant interactions are frictional contacts. 15 minutes after the start of the experiment, this dense structure exhibits a yield stress two times larger than the value obtained in the *yield stress regime* and it appears to be able to stop foam destabilisation.

4.4.4 Stability loss at very high surfactant content

Last point that remains to be elucidated is the stability loss of Steol in the *granular regime* when free cement paste yield stress is very low, i.e. $\tau_y < \tau_y^{**}$. Interstitial yield stress evolution for a foam corresponding to a free cement paste below 1 Pa is plotted in Fig. 4.17. The increase of interstitial yield stress before 15 min is smaller than in the stable foam, but higher than in the case $\tau_y > \tau_y^*$.

The most probable explanation for the observed unstability is that at very low yield stress, drainage of the cement paste can occur between the bubbles. Indeed, a layer of cement can often be seen at the bottom of the highly deflocculated cement foam sample. Flow of a yield stress fluid in the foam channels, called Plateau borders, and nodes can be compared to the flow of a fluid in a porous media. Flow of a yield stress fluid in a porous medium under gravity is expected to occur if the yield stress is below a critical value $\tau_{c,d}$ with depends on the pore radius a [23].

$$\tau_{c,d} = \rho g a \quad (4.9)$$

In the case of a foam, we can assume that the equivalent pore size is of the order of magnitude of the bigger spheres which can pass in the plateau borders. This radius is given by [24]:

$$r_{PB} = R \frac{0.27\sqrt{1-\Phi} + 3.17(1-\Phi)^{2.75}}{1 + 0.57(1-\Phi)^{0.27}} \quad (4.10)$$

When $R=390 \mu\text{m}$ and $\Phi = 83\%$, equation 4.10 gives $r_{PB}=40 \mu\text{m}$. Therefore, $\tau_{c,d} \sim 1 \text{ Pa} \sim \tau_y^{**}$, which explains that the drainage occurs when $\tau_y < \tau_y^{**}$.

Note that drainage in the Plateau borders and nodes may induce a segregation of cement grains in the very deflocculated cement pastes. Diameter of the bigger spheres that can pass in the Plateau borders is $2r_{PB}=80 \mu\text{m}$, which is close to the size of the bigger cement grains. Therefore, while bigger cement grains are potentially retained by the foam nodes and channels, small grains can escape the structure and settle at the sample bottom.

Hydration kinetics may also play a role on foam stability. Though, as mentioned in the previous paragraph, the influence must be minor compared to the early age structuration of the cement paste into a dense granular packing or colloidal network. We can note however that high amount of surfactant can delay hydration: this effect has been observed by other authors [25] and is confirmed for Steol in Fig. 4.18.

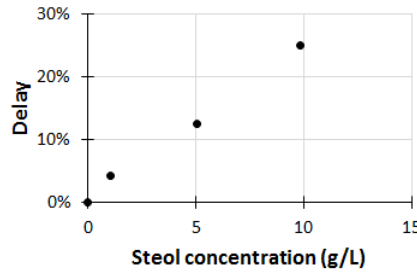


Figure 4.18: Delay of the temperature peak of cement pastes containing Steol (W/C=0.5, CEM I cement from St Vigor factory, Lafarge): $(t_{peak} - t_{peak,ref})/t_{peak,ref}$ where $t_{peak,ref} = 12 \text{ h}$ is the reference time in sample containing no surfactant.

4.5 Conclusion

We have studied the capacity of cement pastes for producing morphology-controlled cement foams. By using two distinct additives, our experimental approach allowed us to tune finely the paste yield stress τ_y while keeping constant several control parameters, namely the W/C ratio, the bubble size and the gas volume fraction. Our results reveal that appropriate morphological control can be achieved, for each studied system, when $\tau_y^{**} < \tau_y < \tau_y^*$.

This result is attributed to the additives-induced reduction of attractive van der Waals interactions: weak attractive forces allow densification of the cement grains within the foam network as well as the simultaneous drainage of the excess interstitial pore solution. Within this regime, the partially flocculated state of cement grains allows for these particles to be retained within the foam skeleton. Combination of these effects has been proved to enhance drastically the effective yield stress property of the bubble-embedded cement paste, resulting in efficient immobilization of fresh foams, without resorting to set accelerators. Such a mechanical behavior is reminiscent of aqueous foams made with granular matter, i.e. grains without any other interaction than contacts, as studied recently by *Gorlier et al.* [19]. We anticipate that the drainage of the excess interstitial pore solution could be critical if the drained volume is large, i.e. for large W/C ratios.

For $\tau_y > \tau_y^*$, cement foams were found to evolve significantly before setting, leading to uncontrolled final morphology. In contrast to the above-described regime, attractive van der Waals forces are strong enough to prevent cement particles from being reorganized within a denser structure between the bubbles, and in the same time, pore cement solution is hardly squeezed out through the interstitial cement paste. As a result, the interstitial cement paste behaves as a “classical” yield stress material with yield stress equal to τ_y . Within our experimental conditions, studied $\tau_y < 100$ Pa values were not found to allow morphology control. However, we anticipate that larger τ_y and/or larger bubble size should allow for such a control.

Finally, we show that fresh cement foams with $\tau_y < \tau_y^{**}$ do not allow foam morphology to be controlled. This result is attributed to the deflocculated state of cement colloidal particles in this regime: deflocculated small cement particles exit the foam skeleton along with the draining pore solution so the above-described densification mechanism is prevented from occurring.

Bibliography

- [1] G. Samson, A. Phelipot-Mardelé, and C. Lanos, “Thermal and mechanical properties of gypsum-cement foam concrete: effects of surfactant,” *Journal of Environmental and Civil Engineering*, vol. 21, no. 12, pp. 1502–1521, 2016. [82](#)
- [2] M. T. Hoang and C. Perrot, “Solid films and transports in cellular foams,” *Journal of Applied Physics*, vol. 112, p. 054911, 2012. [82](#)
- [3] V. Langlois, V. H. Trinh, C. Lusso, C. Perrot, X. Chateau, Y. Khidas, and O. Pitois, “Permeability of solid foam: Effect of pore connections,” *Physical Review E*, vol. 97, p. 053111, 2018. [82](#)
- [4] I. Cantat, S. Cohen-Addad, F. Elias, F. Graner, R. Höhler, O. Pitois, F. Rouyer, and A. Saint-Jalmes, *Foams - Structure and dynamics*. Oxford University Press, 2013. [82](#), [92](#)
- [5] S. Guignot, S. Faure, M. Vignes-Adler, and O. Pitois, “Liquid and particles retention

- in foamed suspensions,” *Chemical Engineering Science*, vol. 65, pp. 2579–2585, 2010. [82](#)
- [6] I. Lesov, S. Tcholakova, and N. Denkov, “Factors controlling the formation and stability of foams used as precursors of porous materials,” *Journal of Colloid and Interface Science*, vol. 426, pp. 9–21, 2014. [82](#)
- [7] I. Lesov, S. Tcholakova, and N. Denkov, “Drying of particle-loaded foams for production of porous materials: mechanism and theoretical modeling,” *RSC Advances*, vol. 4, pp. 811–823, 2014. [82](#)
- [8] R. J. Flatt and P. Bowen, “Yodel: a yield stress model for suspensions,” *Journal of the American Ceramic Society*, vol. 89, no. 4, pp. 1244–1256, 2006. [82](#)
- [9] R. J. Flatt and I. Schöber, “Superplasticizer and the rheology of concrete,” in *Understanding the rheology of concrete* (N. Roussel, ed.), pp. 144–208, Woodhead publishing, 2012. [82](#), [93](#)
- [10] B. Feneuil, O. Pitois, and N. Roussel, “Effect of surfactants on the yield stress of cement paste,” *Cement and Concrete Research*, vol. 100, pp. 32–39, 2017. [82](#), [83](#), [87](#), [93](#)
- [11] T. Zhang, S. Shang, F. Yin, A. Aishah, A. Salmiah, and T. Ooi, “Adsorptive behavior of surfactants on surface of Portland cement,” *Cement and Concrete Research*, vol. 31, pp. 1009–1015, 2001. [83](#)
- [12] F. Gorlier, Y. Khidas, A. Fall, and O. Pitois, “Optimal strengthening of particle-loaded liquid foams,” *Physical Review E*, vol. 95, 2017. [86](#)
- [13] N. Roussel, G. Ovarlez, S. Garrault, and C. Brumaud, “The origins of thixotropy in fresh cement pastes,” *Cement and Concrete Research*, vol. 42, pp. 148–157, 2012. [86](#), [93](#), [96](#), [97](#)
- [14] N. Roussel and P. Coussot, “Fifty-cent rheometer for yield stress measurements: From slump to spreading flow,” *Journal of Rheology*, vol. 49, no. 3, pp. 705–718, 2005. [87](#)
- [15] T. G. Mason, J. Bibette, and D. A. Weitz, “Yielding and flow of monodisperse emulsions,” *Journal of Colloid and Interface Science*, vol. 179, pp. 439–448, 1996. [92](#)
- [16] A. Saint-Jalmes and J. Durian, “Vanishing elasticity for wet foams: Equivalence with emulsions and role of polydispersity,” *Journal of Rheology*, vol. 43, p. 1411, 1999. [92](#)
- [17] M. D. Bolton, “The strength and dilatancy of sands,” *Géotechnique*, vol. 36, no. 1, pp. 65–78, 1986. [93](#)
- [18] A. Fall, G. Ovarlez, D. Hautemayou, C. Mézière, J.-N. Roux, and F. Chevoir, “Dry granular flows: Rheological measurements of the $\mu(i)$ -rheology,” *Journal of rheology*, vol. 59, no. 4, pp. 1065–1080, 2015. [93](#)

- [19] F. Gorlier, Y. Khidas, and O. Pitois, “Yielding of complex liquid foams,” *Journal of Rheology*, vol. 61, pp. 919–930, 2017. [93](#), [95](#), [99](#)
- [20] N. Roussel, A. Lemaître, R. J. Flatt., and P. Coussot, “Steady state flow of cement suspensions: A micromechanical state of the art.,” *Cement and Concrete Research*, vol. 40, pp. 77–84, 2010. [94](#)
- [21] L. Gibson and M. Ashby, eds., *Cellular Solids: Structure and Properties*. Cambridge: Cambridge University Press, 1997. [96](#)
- [22] F. Gorlier, Y. Khidas, and O. Pitois, “Coupled elasticity in soft solid foams,” *Journal of Colloid and Interface Science*, vol. 501, pp. 103–111, 2017. [96](#)
- [23] V. Chaplain, P. Mills, G. Guiffant, and P. Cerasi, “Model for the flow of a yield fluid through a porous medium,” *Journal de Physique II*, vol. 2, pp. 2145–2158, 1992. [97](#)
- [24] N. Louvet, R. Höhler, and O. Pitois, “Capture of particles in soft porous media,” *Physical Review E*, vol. 82, p. 041405, 2010. [98](#)
- [25] S. Wei, Z. Yunsheng, and M. Jones, “Using the ultrasonic wave transmission method to study the setting behavior of foamed concrete,” *Construction and Building Materials*, vol. 51, pp. 62–74, 2014. [98](#)

Chapter 5

Stability criterion for fresh cement foams

Sommaire

5.1 Introduction	104
5.2 Materials and methods	105
5.2.1 Materials	105
5.2.1.1 Cement	105
5.2.1.2 Surfactants	105
5.2.2 Methods	106
5.2.2.1 Precursor foam and mixing	106
5.2.2.2 Protocol	106
5.2.2.3 Observation of stability	107
5.2.2.4 Stability of aqueous foam	107
5.2.2.5 X-ray tomography	108
5.2.3 Properties of cement paste	108
5.2.3.1 Yield stress of cement paste	108
5.2.3.2 Surface tension of cement paste	109
5.3 Results	110
5.3.1 Stability of aqueous foams	110
5.3.2 Drainage and ripening	110
5.3.2.1 Smaller bubbles ($R \lesssim 500 \mu\text{m}$)	110
5.3.2.2 Bigger bubbles ($R \gtrsim 500 \mu\text{m}$)	114
5.3.3 Influence of initial yield stress and bubbles size	116
5.4 Discussion	117
5.4.1 Destabilization mechanisms	117
5.4.2 Characteristic destabilization times	118
5.4.3 Effect of Bingham capillary number	119
5.4.4 15 min interstitial Bingham capillary number	121

5.5 Conclusion 122
 Bibliography 124
 Appendix A: aqueous foam stability 125

5.1 Introduction

When it is unconstrained, a bubble has a spherical shape because of the air-liquid surface tension. Though, in a foam, bubbles are deformed by their neighbors. The structure of a foam was studied in 1873 by Joseph Plateau, who stated three laws known as Plateau's laws [1]: (1) two bubbles are separated by a soap film of constant average curvature, (2) three films join in a channel, called Plateau border, forming 120° angles, (3) four Plateau borders join into a node at angle 109.5°. The resulting morphology of the foam tends to evolve with time due to downward flow of interstitial fluid due to gravity (drainage), air exchange between bubbles (ripening) and film breakage (coalescence), as shown in Fig. 5.1.

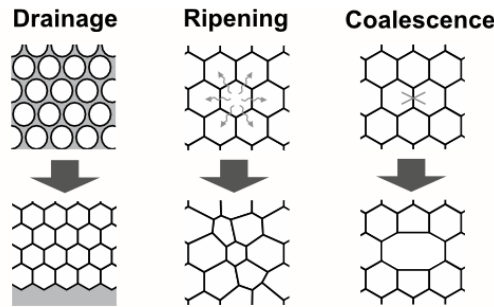


Figure 5.1: Destabilisation mechanisms in a foam (taken from [2])

In cement foams, these destabilization mechanisms can occur until cement paste hardening. Thus, to control the bubble size and air distribution in the foam, we have to stop or slow down these three mechanisms. In this study, we want to define a stability criterion for cement foams. The first step is to select the relevant foam characteristics which should be included in such a criterion.

All destabilization mechanisms are affected by bubble size. Increasing bubble radius R leads to large film areas between the bubbles, which enhances coalescence. It also increases the Plateau borders and nodes width, which favors drainage [1]. Ripening, on the contrary, is reduced when bubble size increases. Indeed, it is caused by the capillary pressure inside the bubbles $P_c = \gamma/R$, where γ is the air-liquid surface tension.

Consistency of the continuous phase, i.e. of cement paste, is also expected to play a major role in foam stability. High yield stress can stop drainage and ripening [3, 4]. However, we have shown in chapter 4 that for foams at given bubble size, air fraction and water-to-cement ratio, best cement foam stability is obtained at intermediate cement paste yield stress: on the one hand, it should be high enough to stop drainage and on the

other hand it should be low enough to allow cement grains confined by the bubbles to reorganize into a dense structure.

To avoid coalescence, liquid film must be stabilized by molecules or partially hydrophobic particles which adsorb at air-water interfaces. The molecules, called surfactants, must be compatible with the highly alkaline cement solution and be present in sufficiently high amount [1].

In the materials and methods, we describe how we prepare cement foams with controlled morphology. The goal of this paper is to investigate the factors controlling the stability of these cement foams. First, the leading destabilization mechanism is identified. Then, effect of bubble size and cement paste yield stress are investigated. Finally, a cement foam stability criteria will be defined, independently from the composition of the foam.

5.2 Materials and methods

5.2.1 Materials

5.2.1.1 Cement

We use two cements. The first will be referred to as C1, it is manufactured by Lafarge, in Saint-Vigor factory and C2 is a CEM I cement from Lafarge, Lagerdorf. Their compositions and physical properties are specified in Table 5.1.

	C1	C2
CaO/SiO ₂	3	3
MgO	1.1%	0.8%
Na ₂ O + 0.658 K ₂ O	0.34%	0.5%
SO ₃	2.58%	2.5 %
Cl ⁻	0.03%	0.04 %
Gypsum	2.4%	4%
Density (g/cm ³)	3.21	3.15
SSB (cm ² /g)	3586	4330

Table 5.1: Chemical and physical properties of cements. C1 refers to CEM I cement from Lafarge, Saint-Vigor and C2 to CEM I cement from Lafarge, Lagerdorf.

5.2.1.2 Surfactants

Two surfactants are used to produce the precursor foam. Tetradecyltrimethyl ammonium bromide (TTAB) is a cationic surfactant at purity above 99% provided by Sigma-Aldrich. Its molar mass is 336 g/mol. Steol[®] 270 CIT is an anionic surfactant provided by Stepan. Its molar mass indicated by the manufacturer is 382 g/mol and active content 68-72%. Surfactant chemical formulas are given in figure 5.2.

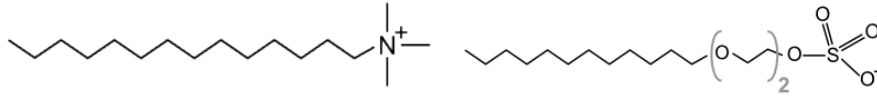


Figure 5.2: Chemical formulas of TTAB and Steol 270 surfactants

Previous study showed that both surfactants are able to form stable foam in a highly alkaline model solution of interstitial cement paste [2].

5.2.2 Methods

5.2.2.1 Precursor foam and mixing

Cement foams are prepared by mixing precursor aqueous foam and cement paste. Precursor foams are generated with the method described in chapter 4. They are monodisperse, i.e. they contain bubbles of the same size. Bubbles are generated with a $\sim 100 \mu\text{m}$ diameter T junction, their radius depends on the entrance rates of the gas (nitrogen) and the foaming liquid (water and surfactant). Bubbles are collected in a column, where liquid fraction is controlled thank to addition of foaming liquid from the top of the foam. Bubble radius are comprised between $200 \mu\text{m}$ and $900 \mu\text{m}$. In TTAB precursor foams, concentration is 10 g/L and liquid fraction is between 0.5 and 2% . In Steol precursor foams, Steol concentration is 1 g/L and liquid fraction, $1.6 \pm 1\%$ when bubble radius is below $350 \mu\text{m}$ and $1.4 \pm 1\%$ otherwise.

Mixing of cement paste and precursor foam is carried with a flow focusing device as described in chapter 4. The main advantage of this method is that bubbles are not broken during the mixing process. Flow rates of the precursor foam and the cement paste are chosen so that the final air content of cement foam is $83\% \pm 2\%$. Note however that flow focusing method requires the flow of the cement paste in small channels (2 mm diameter) and that therefore, yield stress of the paste must be limited to a few tens of Pascals to avoid jamming in the channels.

Mold is filled by deposition of successive cement foam layers. Therefore, cement foam does not undergo strong shearing after its preparation, and bubbles are not broken during sample production.

5.2.2.2 Protocol

All cement foam samples, for each surfactant, are prepared using the same mixing procedure, from water and cement mixing to casting. In the case of Steol samples, surfactant is added to cement paste 20 minutes after cement paste preparation in large amount to make consistency of the paste decrease (see chapter 4). For both surfactants, precursor foam and cement paste are mixed 30 min after cement paste preparation. Protocol is schematized in Fig. 5.3.

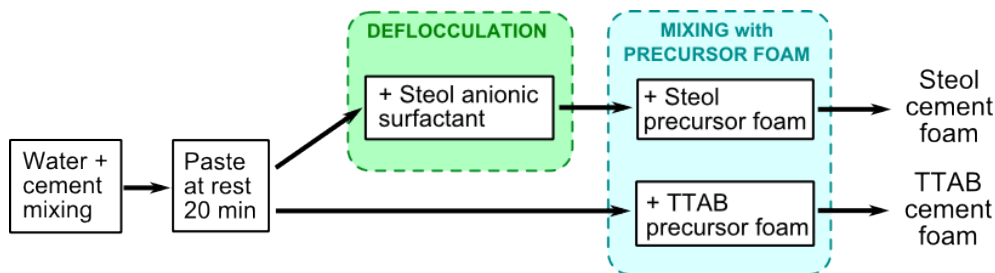


Figure 5.3: Preparation protocol of cement foams made with Steol anionic surfactant and TTAB cationic surfactant.

5.2.2.3 Observation of stability

Samples are cast in 6-cm-high and 2.6-cm-diameter air-tight transparent tubes. They are demolded one week after casting and the stability is visually assessed from the final morphology of the cement foam. Sample stability is assessed as in chapter 4, according to the scale described below. In this study, no cement foam has collapsed, the height of the hardened samples is always 6 cm.

- 3: fully stable sample
- 2: large stable area
- 1: small stable area(s)
- 0: no stable area

We can also observe the evolution of the bubble morphology of fresh cement foams across the transparent molds. Note however that shape of the bubbles that we can see are affected by the presence of the mold wall and are not necessarily representative of the bubbles in the foam volume. In particular, Plateau borders are larger. For samples with big bubble size or low cement paste yield stress, this leads to the full coverage of the mold walls by cement paste. Obtained images are analyzed with ImageJ software to calculate the apparent radius of the bubbles.

Besides, our experimental setup allows us to prevent one or two destabilization mechanisms in some of the samples. To prevent ripening, we use perfluorohexane saturated nitrogen instead of pure nitrogen [1, 5]. Chemical formula of perfluorohexane is C_6F_{14} and it has very low solubility in water, so that it can hardly cross the liquid films between the bubbles. In addition, we can also stop drainage: we make sample rotate at 10 rpm, for several hours after preparation, around a horizontal axis.

5.2.2.4 Stability of aqueous foam

To check the ability of surfactant to stabilize the liquid films during several hours, we prepare an initial height $h_0=11\text{cm}$ of aqueous foam from surfactant solution. Generation method is the same as described in part 5.2.2.1, with initial bubble size $R \approx 300 \mu\text{m}$. Foams with and without C_6F_{14} were tested. At time $t=0$, wetting of the foam by imbibition is

stopped and we record the evolution of the height $h(t)$ of the foam. Both surfactants (TTAB at concentration 5 g/L and Steol at 1 g/L) were tested in distilled water and in a synthetic cement pore solution containing 1.72 g/L of $CaSO_4 \cdot 2H_2O$, 6.959 g/L of Na_2SO_4 , 4.757 g/L of K_2SO_4 and 7.12 g/L of KOH [6].

5.2.2.5 X-ray tomography

Some stable cement foams have been studied by X-ray tomography one or two months after the preparation.

Two types of experiments are performed. Laboratory tomograph gives images of the whole 2.6-cm-diameter and 6-cm-high samples. One 11-cm-high sample has also been prepared and studied. Resolution for the obtained images is 16.3 μm . On the other hand, synchrotron provides high resolution images with voxel size 0.65 μm , on a few millimeter wide pieces of the samples.

5.2.3 Properties of cement paste

5.2.3.1 Yield stress of cement paste

Cement foams prepared with TTAB surfactant are made with C1 cement and those with Steol contain C2 surfactant. In both cases, we estimate the yield stress of the cement pastes corresponding to cement foams, i.e. prepared following the protocol described in 5.2.2.2 with addition of foaming solution (without bubbles) instead of foam. Yield stresses of these pastes are measured by spread tests: paste is poured on a flat horizontal surface and yield stress is obtained by the following formula [7]:

$$\tau_y = \frac{225\rho g\Omega^2}{128\pi^2 R_{spread}^5} \quad (5.1)$$

where Ω and R_{spread} are respectively the volume and the average radius of the spread cement paste and ρ its density. Note that this formula requires that $1 Pa \lesssim \tau_y \lesssim 100 Pa$ [2, 7].

In the case of TTAB, we have seen in a previous study [2] that TTAB partially adsorbs on C1 and has only a low effect on cement paste yield stress. Therefore, paste yield stress depends mainly on the final water-to-cement ratio of the cement foam, W/C_f . Water-to-cement ratio of the precursor cement paste is $W/C_i=0.37$. As air content of the cement foam is constant, W/C_f and final TTAB concentration in cement foam both depend only on the liquid content of the precursor foam. Measured yield stress is given as a function of W/C_f in Fig. 5.4. Yield stress of a solid suspension can be described by the Yodel [8], which states that it is a product of the contribution of the intensity of the forces between two neighboring solid particles m_1 and a function of the solid volume fraction Φ_p :

$$\tau_y = m_1 \frac{\Phi_p^2 (\Phi_p - \Phi_{perc})}{\Phi_{max} (\Phi_{max} - \Phi_p)} \quad (5.2)$$

where Φ_{perc} is the percolation threshold and Φ_{max} is the maximal solid fraction. In cement pastes, Φ_p is related to the water to cement ratio $\Phi_p = 1/(1 + \rho_c/\rho_w W/C_f)$. TTAB hardly affects interparticle interaction between cement grains, therefore, we choose to use equation 5.2 to fit the yield stress of cement pastes containing TTAB. Obtained fitting parameters are $m_1 = 15 \text{ Pa}$, $\Phi_{perc} = 0.32$ and $\Phi_{max} = 0.46$.

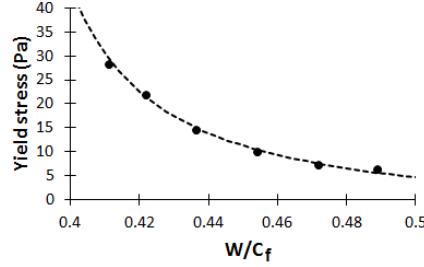


Figure 5.4: Yield stress of cement pastes containing TTAB cationic surfactant (Fit with Yodel, equation 5.2 with $m_1 = 15 \text{ Pa}$, $\Phi_{perc} = 0.32$ and $\Phi_{max} = 0.46$)

Regarding Steol surfactant, we have observed that it has a strong affinity with cement grain surface [2]. Steol adsorption onto cement grains changes the interaction between the particles and modifies the yield stress of the cement paste. At low Steol concentration, yield stress increases due to hydrophobic interaction between cement grains. At high concentration, adsorbed Steol micelles create a steric repulsion between cement grains and reduces the yield stress. For the present study, we choose to use two Steol concentrations in the precursor cement paste: 11.4 and 12.4 g/L. In both cases, the addition of Steol into cement paste makes the yield stress drop to very low values, respectively 4 Pa and 1 Pa. Addition of Steol foaming solution at 1 g/L leads at the same time to an increase of W/C and to a decrease of the final Steol concentration. We measured in chapter 4 that after mixing with foam at liquid content 1.4%, the final water-to-cement ratio is $W/C_f = 0.41$, Steol concentration drops to 10.4 and 11.4 g/L and $\tau_y = 18 \text{ Pa}$ and 3 Pa. When liquid content in the precursor foam is higher, for instance 1.6%, W/C_f increases and Steol concentration decreases, which have opposite effect on the yield stress. Therefore, we will assume that paste yield stress in this case is also $\tau_y = 18 \text{ Pa}$ and 3 Pa.

5.2.3.2 Surface tension of cement paste

For TTAB surfactant, concentration after mixing of the precursor foam into the paste is between 0.7 and 2.4 g/L. Adsorption isotherms measured on pastes at $W/C_f=0.5$ showed that partial adsorption on cement grains leaves a residual concentration in solution between 0.2 and 1 g/L [2]. Surface tension of TTAB at these concentrations in synthetic cement pore solution is comprised between 37 and 42 mN/m [2], so that we can assume for TTAB cement foams $\gamma_{TTAB} \approx 40 \text{ mN/m}$.

For Steol surfactant, both yield stress values are smaller than the yield stress of the same cement paste without surfactant. Therefore, they are both in the high Steol con-

centration regime, and residual concentration is above Critical Micelle Concentration [2], therefore, the surface tension of the cement pastes is $\gamma_{Steol} = 27 \text{ mN/m}$.

5.3 Results

5.3.1 Stability of aqueous foams

Height of aqueous foams was monitored for at least one day. Note that the presence of perfluorohexane tends to make the foam swell. Indeed, there is C_6F_{14} in the bubbles but not in the air in the column above the foam. Difference in C_6F_{14} chemical potentials leads to gas transfer from the air above the foam to the bubbles. This swelling is however not reported on the graphs.

During the six experiments presented in Fig. 5.5, we observe that the foam becomes more and more dry and that the size of air bubbles increases. However, the height of the foam did not decrease for 10 hours in all cases. Foams made with synthetic cement pore solution are less stable than in distilled water, and the absence of C_6F_{14} also increases destabilization speed; however, both these effects can be seen only after 10 hours.

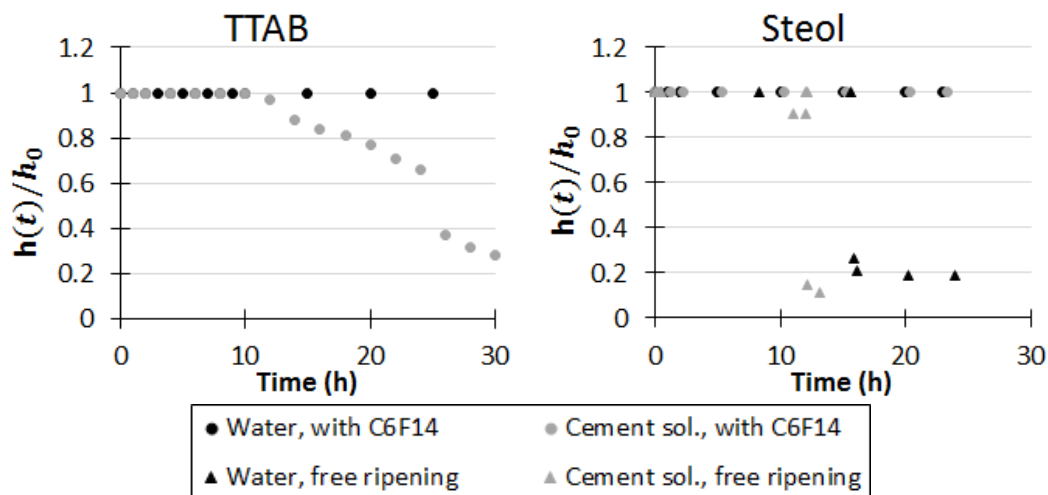


Figure 5.5: Evolution of the height of aqueous foams with time made with TTAB solutions at 5 g/L (left) and Steol solutions at 1 g/L. Black dots or triangles refers to surfactant solutions in distilled water and grey signs to synthetic cement paste solutions. Dots refers to foams containing C_6F_{14} to slow down ripening and triangles to foams made of nitrogen only.

5.3.2 Drainage and ripening

5.3.2.1 Smaller bubbles ($R \lesssim 500 \mu\text{m}$)

All the samples presented in Table 5.2 are unstable if none of the destabilisation mechanism is artificially counteracted. For all of them, preventing drainage by a rotation of the samples does not stop destabilisation, whereas samples containing perfluorohexane are stable.

R (μm)	Free drainage and ripening	No drainage Free ripening	No ripening Free drainage	No ripening No drainage
TTAB - C1, W/C_f from 0.39 to 0.5				
≈ 300	Unstable	Unstable	STABLE	STABLE
≈ 400	Unstable	Unstable	STABLE	STABLE
Steol - C2, $\tau_y = 18 \text{ Pa}$				
≈ 200	Unstable	Unstable	STABLE	STABLE
≈ 300	Unstable	Unstable	STABLE	STABLE
≈ 400	Unstable	Unstable	STABLE	STABLE
Steol - C2, $\tau_y = 3 \text{ Pa}$				
≈ 200	Unstable	Unstable	STABLE	STABLE

Table 5.2: Effect of slowing down ripening and drainage on sample stability.

When W/C_f is further increased above 0.5 for TTAB samples containing perfluorohexane, we sometimes notice a segregation of cement grains at the bottom of the samples as illustrated in Fig. 5.6 for a TTAB sample at $W/C_f=0.69$ (i.e. a yield stress deduced for equation 5.2 below 1 Pa) where $R = 300 \mu\text{m}$. Bubble size after cement hardening in these samples is kept unchanged, except at the bottom of the sample.



Figure 5.6: Bottom of cement foam sample 15 minutes after production containing TTAB, $R = 300 \mu\text{m}$, $W/C_f=0.69$ with perfluorohexane ($\tau_y < 1 \text{ Pa}$). Sample diameter is 2.6 cm.

Some pictures of the samples after cement hardening are shown as examples in Fig. 5.7. Each bubble is connected with its neighbors; the size of the opening between two bubbles depends on the bubble size. Just after sample production and during several hours, the bubbles are separated by a liquid film containing no cement particle. When the samples are demolded after 7 days, the liquid film has already disappeared.

Note that for the smaller bubbles, mixing of cement paste and foam is sometimes not fully homogeneous at the bubble scale: small volumes of cement paste only are surrounded by foam of higher air content than the average value (see Fig. 5.8, top). For instance structure of foams in pictures (c) and (d) in Fig. 5.7 should be the same, but mixing was more inhomogeneous in sample (c). However, the quality of the mixing does not change the fact that samples are stable only if ripening is prevented: the bubble size distribution measured from the tomography images after cement hardening is narrow around

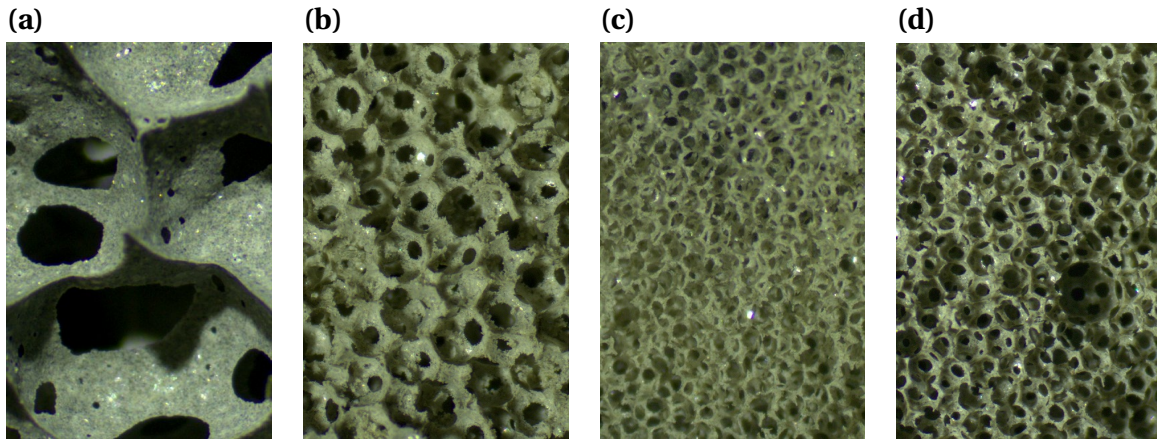


Figure 5.7: Pictures of hardened cement foams. From left to right: (a) sample containing TTAB, initial bubble size $400\ \mu\text{m}$, with no control of destabilisation mechanisms; (b) sample containing Steol (18 Pa), initial bubble size $300\ \mu\text{m}$, with perfluorohexane; (c) sample containing Steol (18 Pa), initial bubble size $200\ \mu\text{m}$, with perfluorohexane; (d) sample containing Steol (3 Pa), initial bubble size $200\ \mu\text{m}$, with perfluorohexane. Height for all pictures is 5 mm.

the average value (see Fig. 5.8, bottom).

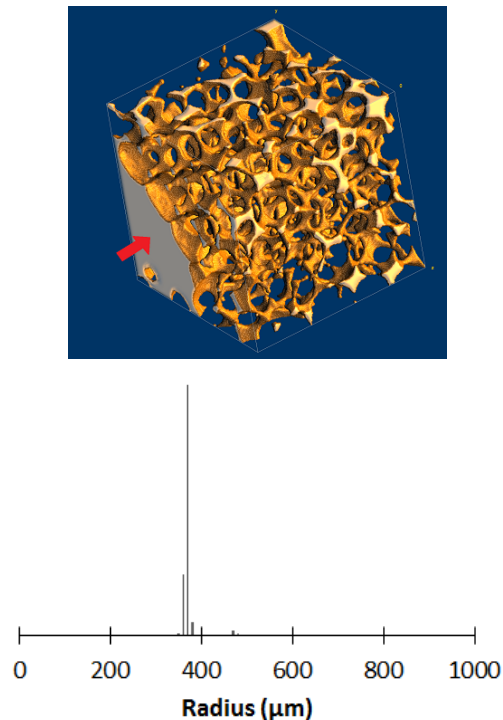


Figure 5.8: Top : 3D reconstruction from tomography experiment on a TTAB cement foam, $R=370\ \mu\text{m}$ and $W/C_f=0.42$, stabilized by perfluorohexane. Red arrow indicates an area without bubbles. Cube size is 3 mm. Bottom: Bubble size distribution by volume (arbitrary unit on vertical axis), statistics on a 1.5 cm cube in the middle of the sample (about 10 000 bubbles).

An example of the evolution of the morphology of a TTAB cement foam with $R =$

365 μm is shown in Fig. 5.9. The average radius of the bubbles and the radius of the bigger bubbles (i.e. average of the bigger three radius) are given in Fig. 5.10 for two TTAB samples with different initial bubble sizes. Note that fast variations for the default size curves are due to the image analysis process: some of the bubbles cannot be identified on all the pictures because of unclean sample walls.

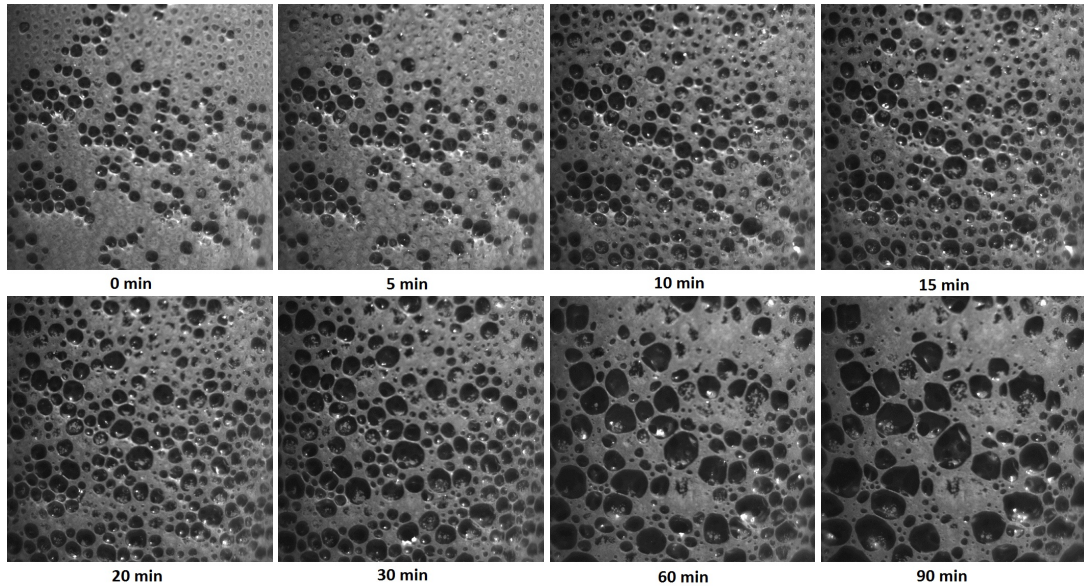


Figure 5.9: Evolution of morphology of fresh cement foam. Example of sample with initial bubble radius 365 μm , $W/C=0.41$ and 83% air content containing TTAB surfactant. Picture width is 1.5 cm.

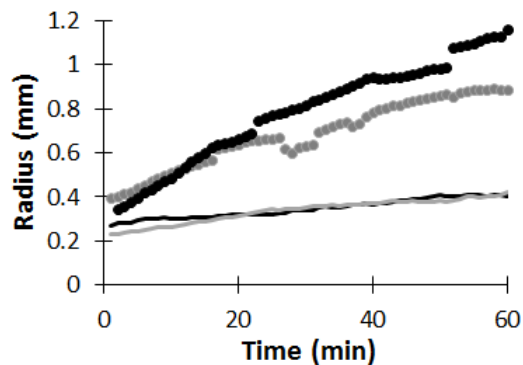


Figure 5.10: Evolution of bubble radius with time for the TTAB samples with initial bubble radius 365 μm , $W/C_f=0.41$ (grey curves) and 270 μm , $W/C_f=0.42$. Lines correspond to average value of all the bubbles and dots show the size of the defaults (average of the bigger three radius).

For both samples, the maximal radius and the average radius of the apparent bubbles start to increase just after sample preparation. We can notice that the apparent radius are below the radius of the bubbles of the precursor foam due to the width of the Plateau borders on the pictures. Bubble size increases faster when the initial bubble size is smaller. Time for the bigger bubbles to reach twice their initial size is about 20 minutes after foam

preparation when $R = 270 \mu\text{m}$ and $W/C_f = 0.42$, and 40 minutes after foam preparation when $R = 365 \mu\text{m}$, $W/C_f = 0.41$

5.3.2.2 Bigger bubbles ($R \gtrsim 500 \mu\text{m}$)

In samples containing bigger bubbles, air fraction often increases from the bottom to the top of the sample when drainage is not prevented through rotation. Examples of slices obtained by X-ray tomography of a 11 cm high sample are shown in Fig. 5.11. Air fraction has been calculated by image analysis of the tomography slices, and is plotted at the bottom of Fig. 5.11 as a function of the height. It increases from 80% at the bottom of the sample to 85% at the top of the 11 cm high sample. This curve additionally shows oscillations of the air fraction over a length scale close to $1300 \mu\text{m}$, i.e. the diameter of the bubbles (see inset). This is a signature of the organization of the monodisperse bubbles into a crystalline structure. When the curve is averaged over a height bigger than the bubble size (black curve), some local minima and maxima are still present. The local variations may be created during the mixing of cement paste and precursor foam or appear later during the drainage of the sample. In Fig. 5.12, a 3D reconstruction drawn from the tomography images is shown. In addition, the volume size distribution of the bubbles is plotted and confirms the narrow distribution around the average bubble radius

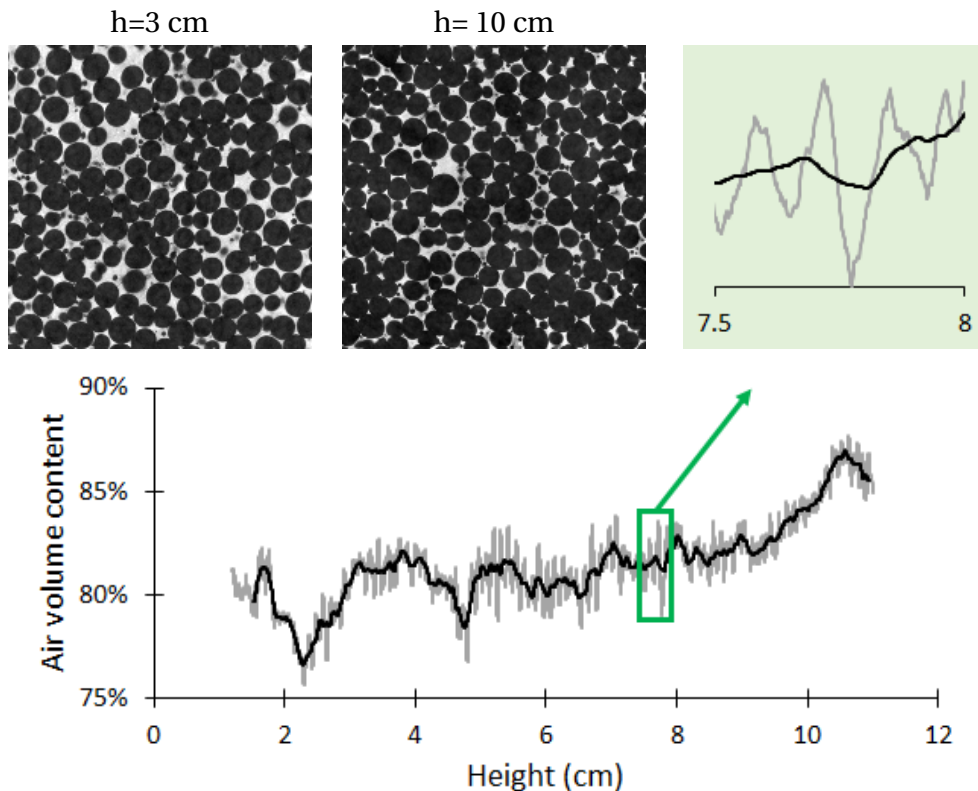


Figure 5.11: Steol sample ($\tau_y=3 \text{ Pa}$, $R=685 \mu\text{m}$). Top: Slices of cement foam sample obtained by X-ray tomography at different height, bubbles appear in black and cement paste is grey. Bottom : evolution of air fraction with sample height. Grey curve is raw data, black curve is the data average over $2000 \mu\text{m}$

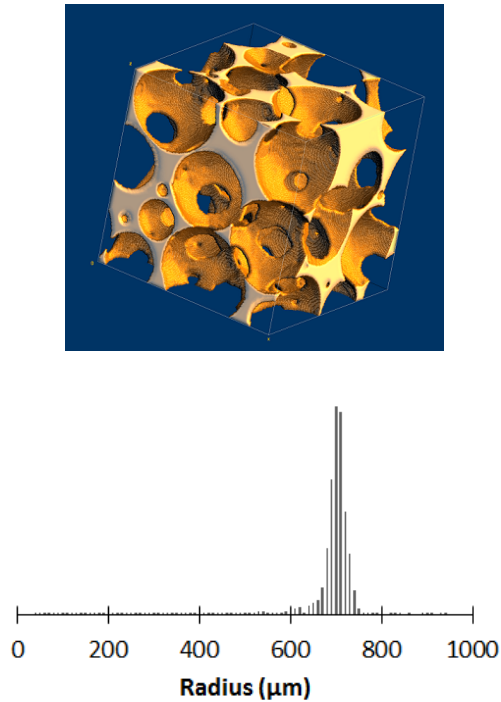


Figure 5.12: Top: 3D reconstruction from tomography experiment on a Steol sample ($\tau_y = 3$ Pa, $R = 685$ μm). Cube size is 3 mm. Bottom: Bubble size distribution by volume (arbitrary unit on vertical axis), statistics on a 1.5 cm cube in the middle of the sample (about 2000 bubbles).

In addition, drainage sometimes leads to a strong destabilization of bubbles at the bottom of the sample (see Fig. 5.13, left). Preventing drainage by sample rotation makes the sample more homogeneous (see Fig. 5.13, center) but often leads to weak samples, that break when they are demolded (see Fig. 5.13, center). This occurs when cement paste in the foam sample moves when sample rotates, which is often the case when τ_y is too low.



Figure 5.13: Comparison of samples with big bubble size (TTAB, $\Phi=0.87\%$, $R=1000$ μm) after free drainage ($W/C_f=0.44$, left) and when drainage has been prevented by rotation (center and right). Rotation sometimes leads to weak samples that break when they are demolded ($W/C_f=0.49$, right). Sample height is 6 cm.

5.3.3 Influence of initial yield stress and bubbles size

In the following we do not consider the destabilization of the bottom the foam samples due to drainage. A sample is considered as instable when a major change of bubble size has occurred in the whole sample. Cement foam stability for samples are gathered in Figs. 5.14 and 5.15. For Steol, each point correspond to at least two experiments. In some of the cases, identical foams have different stability behavior.

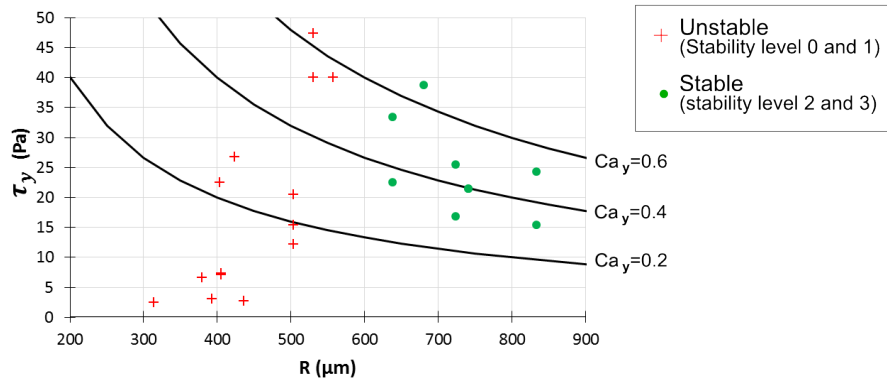


Figure 5.14: Stability of TTAB-C1 cement foam samples. Black lines show constant Bingham capillary number with $\gamma_{TTAB} = 40 mN/m$

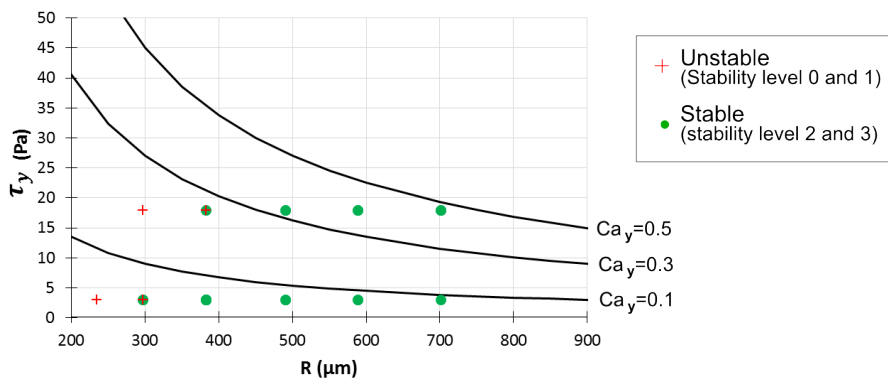


Figure 5.15: Stability of Steol-C2 cement foam samples. Black lines show constant Bingham capillary number with $\gamma_{Steol} = 27 mN/m$

We observe for both surfactants a large effect of bubble size: all samples are stable when R is high and unstable at very low R . Minimum radius for stable foams depends however on the composition of the foams: $600 \mu m$ for TTAB and C1, and respectively $400 \mu m$ and $200 \mu m$ for Steol and C2 when $\tau_y = 18 Pa$ and $3 Pa$. On the contrary, increase of yield stress does not improve stability in the studied range, i.e. below $50 Pa$. Higher yield stresses can not be achieved with our mixing device.

5.4 Discussion

5.4.1 Destabilization mechanisms

First, volume of aqueous foams for both surfactants was constant for more than 10 hours with C_6F_{14} and without. Stability of a liquid film depends on the ability of the surfactant layers on both interfaces to repel each other. Film breakage occurs when the disjoining pressure Π_d , i.e. the pressure in the liquid film due to the repulsion on the air-liquid interfaces, reaches a critical value $\Pi_{d,crit}$. In an aqueous foam in equilibrium, disjoining pressure is maximal at the top of the foam and $\Pi_d = \rho_l g h$ where ρ_l is the liquid density. Our results show that TTAB and Steol are able to prevent coalescence, even in the highly alkaline conditions in cement paste, at $\Pi_d = 1000 \text{ Pa}$. In foams, coalescence can take place even if $\Pi_d < \rho g h_{crit}$, because bubble rearrangement can lead to film breakage due to dynamics, if liquid volume content is very low [9]. Rearrangements can for instance be a consequence of the evolution of bubble shape due to ripening. This explains why coalescence occurs after a few hours in Steol aqueous foams containing perfluoroexane whereas the sample foams with perfluorohexane were stable for 30 hours.

These observations on aqueous foams show that coalescence is not expected to be the leading destabilisation mechanism in cement foam samples when their height is below 11 cm. Let us now investigate the other two mechanisms. Drainage should stop if yield stress exceeds a critical value $\tau_{c,d}$ whose order of magnitude is given by [3]:

$$\tau_{c,d} \sim \rho g r \quad (5.3)$$

where r refers to the external radius of curvature of Plateau borders. At high air content $\Phi > 99\%$, $r \approx R/\sqrt{(1-\Phi)/0.33}$ [1] whereas at low air content $\Phi \rightarrow 64\%$, $r \rightarrow R$. In our case $\Phi = 83\%$; we take $r \sim R$, so $\tau_{c,d} \sim \rho g R$.

Ripening is expected to be slowed down or stopped when the yield stress of the interstitial material reaches the order of magnitude of the bubble capillary pressure P_C [4]. Therefore, we define the critical stress for ripening as:

$$\tau_{c,r} \sim \gamma/R \quad (5.4)$$

Both critical stresses for drainage and ripening depend on the bubble radius R . We can estimate their value for cement foam samples, where $\rho \simeq 2000 \text{ kg/m}^3$ and $\gamma \simeq 30 \text{ mN/m}$. The obtained curves are shown in Fig 5.16. We notice that for the bubble sizes we have studied, i.e. $100 \mu\text{m} < R < 1000 \mu\text{m}$, $\tau_{c,d} < \tau_{c,r}$. $\tau_{c,r}$ is two orders of magnitude above $\tau_{c,d}$ when R is a few $100 \mu\text{m}$, which explains that ripening is the dominant destabilization mechanism at small bubble size. When $R \rightarrow 1 \text{ mm}$, critical stresses for drainage and ripening are the same order of magnitude, and drainage can take place even if no major evolution of bubble size occurs.

To summarize, the orders of magnitude of the stresses in Fig. 5.16 are in adequation with experimental observations: ripening is the major destabilization mechanism for the smaller bubble size, and drainage starts to play a role when $R \rightarrow 1 \text{ mm}$.

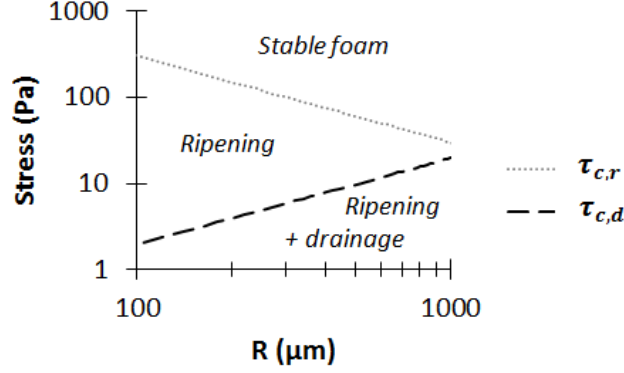


Figure 5.16: Comparison of driving stresses for drainage and ripening. The curves define three possible behavior of cement foams when no experimental artifice is used to slow down ripening or drainage: stable foam if $\tau_y > \tau_{c,r}$, both drainage and ripening if $\tau_y < \tau_{c,d}$ and only ripening at intermediate yield stress values.

5.4.2 Characteristic destabilization times

To get deeper understanding of drainage and ripening, we can calculate their respective time scales.

Let us first calculate a rough estimation of drainage characteristic time t_d . It depends on the cement foam sample height H and the drainage velocity v : $t_d = H/v$. The velocity is given by Darcy's law for pressure gradient induced by gravity ρg :

$$v = \frac{k}{\mu_{app}} \rho g \quad (5.5)$$

Where k is the permeability and μ_{app} the apparent viscosity of the cement paste. Permeability of a foam depends of the air fraction and the bubble size [10]:

$$k = \frac{4(1 - \Phi)^{3/2}}{1700(1 - 2.7(1 - \Phi) + 2.2(1 - \Phi)^2)^2} R^2 \quad (5.6)$$

For $\Phi = 0.83$, this gives $k = 5.10^{-4} R^2$.

To assess the apparent viscosity of the continuous phase, a rheological model must be chosen. Bingham model describes well the rheological behavior of cement paste [11], the stress τ and the shear rate $\dot{\gamma}$ in the paste are related by:

$$\tau = \tau_y + \mu_p \dot{\gamma} \quad (5.7)$$

where the yield stress τ_y and the plastic viscosity μ_p depends on the paste formulation. We have measured the flow curves of three cement pastes with no surfactant, at water-to-cement ratio from 0.37 to 0.5 (results not shown here). For all three of them, stress at $\dot{\gamma}_{100} = 100 \text{ s}^{-1}$ is close to $2\tau_y$, i.e. $\mu_p \sim \tau_y / \dot{\gamma}_{100}$.

At the scale of the Plateau borders and nodes, the stress is $\tau \sim \rho g r$ where r is the charateristic size of the channels and is close to the bubble radius R for the studied air fraction. The apparent viscosity is therefore

$$\mu_{app} = \tau / \dot{\gamma} \sim \frac{\rho g R \tau_y}{(\rho g R - \tau_y) \dot{\gamma}_{100}} \quad (5.8)$$

From equations 5.5, 5.6 and 5.8, we find that the characteristic drainage time is

$$t_d \sim \frac{H \tau_y}{5.10^{-4} R (\rho g R - \tau_y) \dot{\gamma}_{100}} \quad (5.9)$$

This gives, for $\tau_y = 1 \text{ Pa}$, $t_d \sim 30 \text{ min}$ when $R = 200 \text{ }\mu\text{m}$ and $t_d \sim 1 \text{ min}$ when $R = 700 \text{ }\mu\text{m}$.

Regarding ripening, characteristic time is given by [12]:

$$t_r = \frac{2R_0^2}{K_2} \quad (5.10)$$

where K_2 is the diffusion coefficient. For nitrogen and low molecular weight surfactants $K_2 \sim 50 \text{ }\mu\text{m}^2/\text{s}$. For polydisperse foams, characteristic time given by equation 5.10 is the time during which the average bubble size grows from its initial value R_0 to $2 R_0$. In the case of monodisperse foams, ripening is delayed. First, there is an induction period during which defaults appear and grow in the foam. The length of this induction period is not known. However, we chose to use equation 5.10 with $R_0 = R$ to assess the time evolution of the defaults due to ripening.

We obtain $t_r \sim 50 \text{ min}$ when $R = 270 \text{ }\mu\text{m}$ and $t_r \sim 90 \text{ min}$ when $R = 365 \text{ }\mu\text{m}$. These calculated times are the same order of magnitude than the ripening times observed in Fig. 5.10.

Comparison of drainage and ripening characteristic times shows that when cement paste yield stress is below driving pressures for both drainage and ripening, drainage occurs faster than ripening as soon as $R \gtrsim 200 \text{ }\mu\text{m}$.

	R = 200 μm	700 μm	1 mm
$\tau_y = 1 \text{ Pa}$	Drainage + ripening $\sim 30 \text{ min}$	Drainage $\sim 1 \text{ min}$	Drainage $\sim 1 \text{ min}$
10 Pa	Ripening $\sim 30 \text{ min}$	Drainage $\sim 1 \text{ h}$	STABLE
100 Pa	Ripening $\sim 30 \text{ min}$	STABLE	STABLE

Table 5.3: Characteristic destabilization times for cement foams with different bubble size and interstitial yield stress

5.4.3 Effect of Bingham capillary number

We have identified ripening as the major destabilisation mechanism. To go further, we can use the Bingham capillary number which compares the yield stress (stabilizing effect) with the capillary pressure inside the bubbles, which leads to ripening:

$$Ca_y = \frac{\tau_y}{\tau_{c,r}} = \frac{\tau_y}{\gamma/R} \quad (5.11)$$

We expect that a suitable criterion for foam stability would be under the form of a critical capillary number Ca_y^* . Most intuitive calculation of Bingham capillary number would use the yield stress of the free cement paste τ_y obtained from Fig. 5.4. The calculated values are plotted in Fig. 5.14 and 5.15 and compared to the stability of TTAB and Steol samples. Ca_y for all the samples are summarized in Fig. 5.17. We see that Ca_y cannot be used to predict cement foam stability: even if stability improves with increasing bubble size as expected, no improvement can be seen when τ_y increases up to 50 Pa.

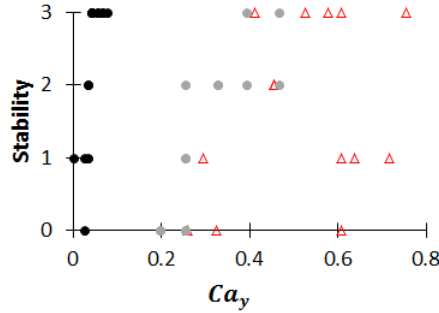


Figure 5.17: Cement foam stability as a function of Bingham capillary number calculated from free cement paste yield stress. Black dots correspond to Steol samples with $\tau_y = 3$ Pa, grey dots to Steol samples with $\tau_y = 18$ Pa and empty triangles to TTAB samples.

τ_y is therefore not the adequate yield stress that we can take into account to define a stability criterion. Chapter 4 provides two hints to define a better criterion :

- The yield stress of the cement paste when it is confined in the foam structure can be higher than the free yield stress. It is the effective stress that the bubbles must overcome to deform, consequently, it is more likely to be related to foam stability than free yield stress. Interstitial yield stress $\tau_{y,int}$ can be obtained from macroscopic foam yield stress $\tau_{y,foam}(\Phi)$ by [13]:

$$\tau_{y,int} = \left(1 - \frac{\tau_{y,foam}(\Phi)}{\tau_{y,aq}(\Phi)}\right)^{3/2} \frac{\gamma}{Rc^{3/2}(1-\Phi)^2} \quad (5.12)$$

where $\tau_{y,aq}(\Phi) = 0.6 \frac{\gamma}{R} (\Phi - \Phi_c)^2$ is the yield stress of aqueous foam with the same air content and $c=110$ is a constant.

- Yield stress of cementitious materials at rest increases with time due to flocculation and creation of hydrate bonds between the particles [11]. Therefore, we can wonder what age t^* should be taken into account to define a stability criterion. We have seen in Fig. 5.10 that for unstable samples, the size of the bigger bubbles doubles in several tens of minutes, so we choose to try $t^* = 15$ min.

5.4.4 15 min interstitial Bingham capillary number

We have measured cement foam yield stress at 15 min with rheometry protocol described in chapter 4. Interstitial capillary number have been deduced using Equation 5.12. Note that bubble size have an effect on interstitial yield stress: interstitial yield stress decreases when bubbles size increases.

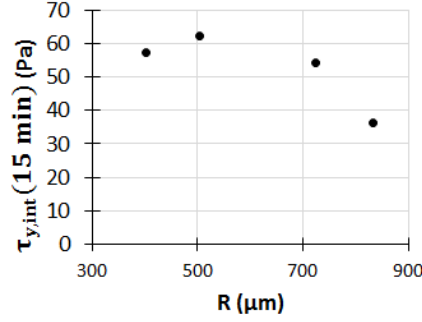


Figure 5.18: Interstitial yield stress calculated from foam yield stress measured at 15 min for samples containing TTAB, $W/C_f=0.42$

Two hypothesis can account for this observation. First, equation 5.12 has been empirically obtained on model yield stress fluids (oil-in-water emulsion and beads suspension) when $Ca_{y,int} = R\tau_{y,int}/\gamma < 0.5$. The interstitial yield stress value obtained for the bigger bubbles in Fig. 5.18 gives $Ca_{y,int} \simeq 1$, so that a deviation of the yield stress from the value given by equation 5.12 is possible.

Besides, a possible effect of bubble size is illustrated by the high resolution tomography pictures in Fig. 5.19. When the bubbles are small, the bigger cement grains, whose diameter before the start of hydration is about 100 μm , have similar size as the Plateau borders. Note that the synchrotron pictures have been taken two months after the sample preparation, when most of the cement has reacted with water and formed hydrates, and that therefore apparent cement grain size on the pictures is smaller than their initial size. The diameter of the bigger particles that can enter the Plateau borders is given by equation [14]:

$$d_{PB} = 2R \frac{0.27\sqrt{1-\Phi} + 3.17(1-\Phi)^{2.75}}{1 + 0.57(1-\Phi)^{0.27}} \quad (5.13)$$

With $\Phi = 83\%$, we obtain $d_{PB} = 60 \mu m$ if $R = 300 \mu m$ and $d_{PB} = 160 \mu m$ if $R = 800 \mu m$. As a consequence, when the bubbles are small, bigger cement grains cannot enter the Plateau borders and are stuck in the foam nodes. This leads to a segregation of cement grains following their size, this segregation can change the yield stress of the cement paste.

Stability of samples is plotted as a function the interstitial capillary number at $t^* = 15$ min in Fig. 5.20. We can see for all the curves that a transition from unstable samples at $Ca_{y,int}(t^*) \lesssim 1$ to stable samples when $Ca_{y,int}(t^*)$ is higher. We can therefore define a critical value of the capillary number $Ca_{y,int}^*(t^*) = 1$. It is important to note that the value of t^* is expected to highly depends on the preparation method of cement foam sample

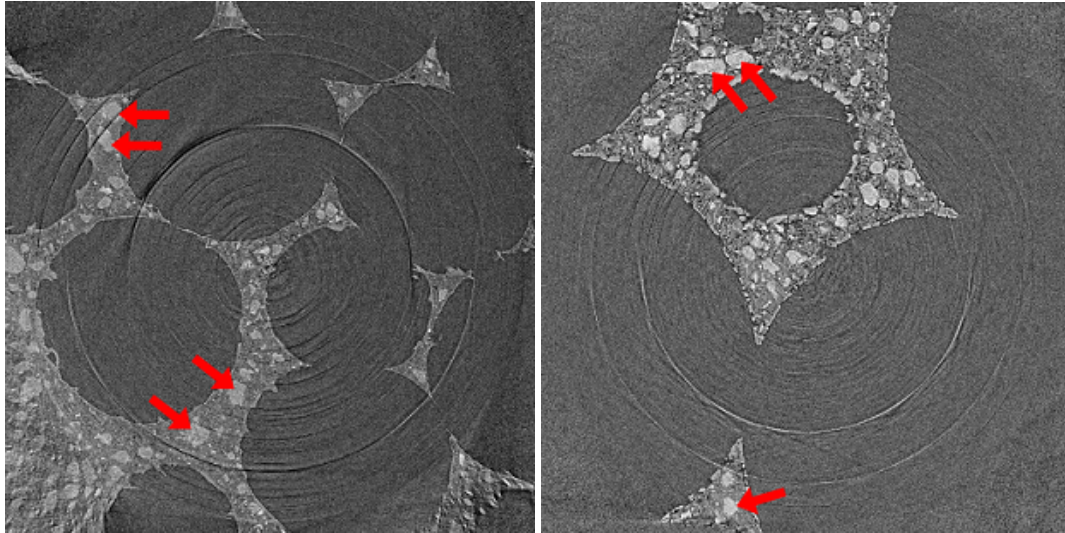


Figure 5.19: Synchrotron slices of TTAB cement foams stabilized by C_6F_{14} , for $R=265 \mu\text{m}$ (left) and $R=550 \mu\text{m}$ (right), two months after preparation. Image width is $1300 \mu\text{m}$. Red arrows indicate some of the bigger cement grains.

and can be affected, for instance, by the polydispersity of the foam and the setting time of the cement.

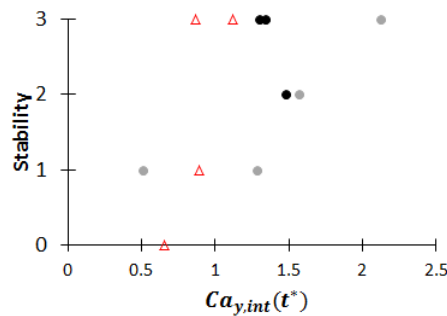


Figure 5.20: Cement foam stability as a function of Bingham capillary number calculated from interstitial yield stress at 15 min. Black dots correspond to Steol samples with $\tau_y = 3 \text{ Pa}$, grey dots to Steol samples with $\tau_y = 18 \text{ Pa}$ and empty triangles to TTAB samples.

5.5 Conclusion

We have investigated the mechanisms at stake in the destabilization of cement foam samples. We first note that a proper choice of surfactant can prevent coalescence of the films up to cement hardening.

For most cement foam samples, prepared either with anionic or cationic surfactant, ripening is the leading destabilization mechanism. Drainage is also sometimes observed when yield stress of cement paste is very low or bubble size is big. In these cases, drainage takes place faster than ripening.

Ripening is avoided if $Ca_{y,int}(t^*) > Ca_{y,int}^*(t^*) \simeq 1$ where t^* depends on the preparation method of the foam. This criterion is independent of bubble size, cement paste yield stress and surfactant. Yield stress used for the calculation of this criterion is the interstitial yield stress.

In this work, the air fraction of the samples has been kept constant and both cement used have similar setting times. In addition, we have studied foams with initially very narrow bubble size distribution. We can wonder how these factors change the stability criterion and whether they affect its value or the time t^* .

Bibliography

- [1] I. Cantat, S. Cohen-Addad, F. Elias, F. Graner, R. Höhler, O. Pitois, F. Rouyer, and A. Saint-Jalmes, *Foams - Structure and dynamics*. Oxford University Press, 2013. [104](#), [105](#), [107](#), [117](#)
- [2] B. Feneuil, O. Pitois, and N. Roussel, “Effect of surfactants on the yield stress of cement paste,” *Cement and Concrete Research*, vol. 100, pp. 32–39, 2017. [104](#), [106](#), [108](#), [109](#), [110](#), [125](#)
- [3] S. Guignot, S. Faure, M. Vignes-Adler, and O. Pitois, “Liquid and particles retention in foamed suspensions,” *Chemical Engineering Science*, vol. 65, pp. 2579–2585, 2010. [104](#), [117](#)
- [4] I. Lesov, S. Tcholakova, and N. Denkov, “Factors controlling the formation and stability of foams used as precursors of porous materials,” *Journal of Colloid and Interface Science*, vol. 426, pp. 9–21, 2014. [104](#), [117](#)
- [5] H. Bey, F. Wintzenrieth, O. Ronsin, R. Höhler, and S. Cohen-Addad, “Stabilization of foams by the combined effects of an insoluble gas species and gelation,” *Soft Matter*, vol. 13, pp. 6816–6830, 2017. [107](#)
- [6] H. Bessaies-Bey, *Polymères et propriétés rhéologiques d'une pâte de ciment : une approche physique générique*. PhD thesis, Université Paris-Est - SIE, 2015. [108](#)
- [7] N. Roussel and P. Coussot, “Fifty-cent rheometer for yield stress measurements: From slump to spreading flow,” *Journal of Rheology*, vol. 49, no. 3, pp. 705–718, 2005. [108](#)
- [8] R. J. Flatt and P. Bowen, “Yodel: a yield stress model for suspensions,” *Journal of the American Ceramic Society*, vol. 89, no. 4, pp. 1244–1256, 2006. [108](#)
- [9] A.-L. Biance, A. Delbos, and O. Pitois, “How topological rearrangements and liquid fraction control liquid foam stability,” *Physical Review Letters*, vol. 106, p. 068301, 2011. [117](#)
- [10] F. Rouyer, O. Pitois, E. Lorenceau, and N. Louvet, “Permeability of a bubble assembly: from the very dry to the wet limit,” *Physics of Fluids*, vol. 22, p. 043302, 2010. [118](#)

- [11] N. Roussel, A. Lemaître, R. J. Flatt., and P. Coussot, “Steady state flow of cement suspensions: A micromechanical state of the art.,” *Cement and Concrete Research*, vol. 40, pp. 77–84, 2010. [118](#), [120](#)
- [12] O. Pitois, “Foam ripening,” in *Foam Engineering: Fundamentals and Applications* (P. Stevenson, ed.), pp. 59–73, John Wiley & Sons, 2012. [119](#)
- [13] F. Gorlier, Y. Khidas, and O. Pitois, “Yielding of complex liquid foams,” *Journal of Rheology*, vol. 61, pp. 919–930, 2017. [120](#)
- [14] N. Louvet, R. Höhler, and O. Pitois, “Capture of particles in soft porous media,” *Physical Review E*, vol. 82, p. 041405, 2010. [121](#)

Appendices

Appendix A: aqueous foam stability

Stability of aqueous foam is shown in Fig. 5.21 for several surfactants studied in [2] and appendix of chapter 2. All foams contain perfluorohexane.

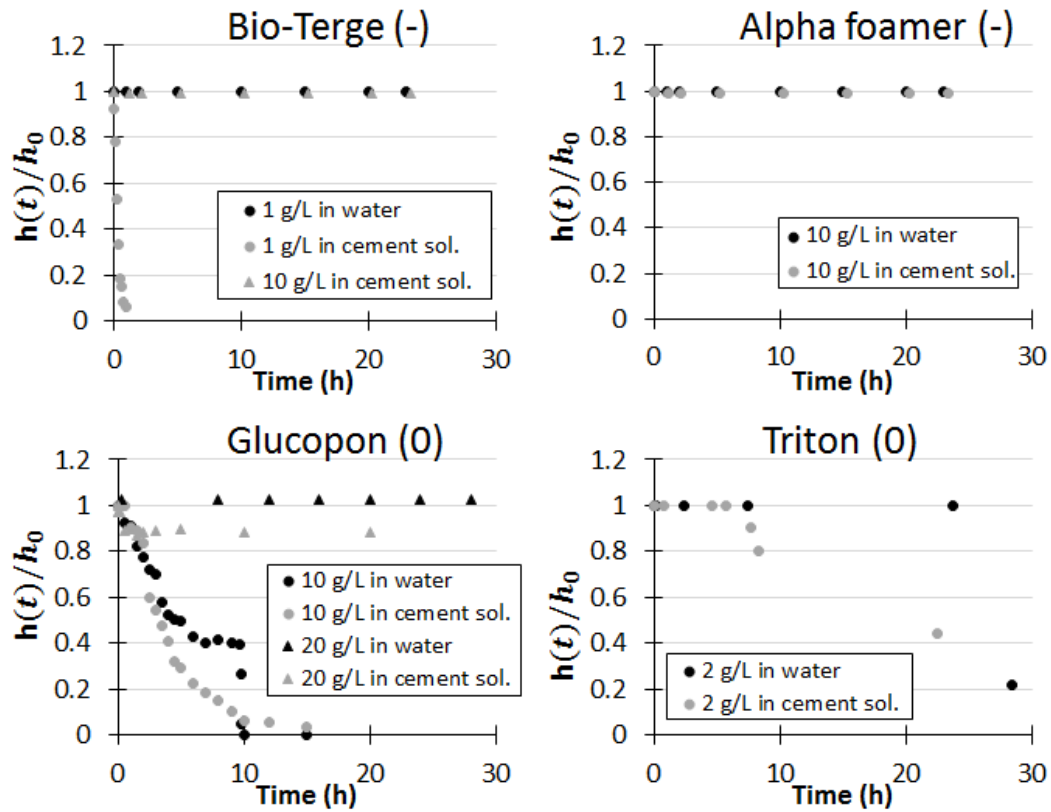


Figure 5.21: Stability of aqueous foams containing perfluorohexane with surfactants studied in chapter 2.

Synthetic cement pore solution makes Bio-Terge foam less stable. Whereas Bio-Terge at 1 g/L can stabilize aqueous foam. Glucopton at 10 g/L was not enough to get stable foams for 10 hours, whereas 20 g/l provided stable foams in water and synthetic cement pore solution. Alpha Foamer and Triton are stable at the studied concentration in water and synthetic cement pore solution for at least 10 h.

Chapter 6

Water imbibition of open-cell cement foams

Sommaire

6.1 Introduction	127
6.2 Materials and methods	128
6.2.1 Materials	128
6.2.2 Cement foam production	128
6.2.3 Characterization of the foam morphology	129
6.2.4 Permeability measurement	130
6.2.5 Imbibition experiment	131
6.3 Results and discussion	131
6.4 Conclusion	136
Bibliography	137

6.1 Introduction

Durability of construction materials can be jeopardized by successive imbibition/drying cycles. Therefore, controlling sorption properties of those materials is a crucial issue and water repellents can be used for preventing or decreasing water absorption [1]. Theory of capillary imbibition has been intensively studied from the pioneering works of *Bell & Cameron* [2], *Lucas* [3] and *Washburn* [4]. They assumed, in agreement with experimental observations, that under the action of capillary effects, a wet front progresses through the sample while saturating the material behind. The above basic theory turns out to be inappropriate when applied to complex materials with several levels of porous phases. This is the case for foamed concretes [5], autoclaved aerated concretes [6] and aerated gypsum [7] for example, in which effects of multimodal distributions of pores remain difficult to understand in terms of material sorption characteristics. However, designing materials with appropriate imbibition properties requires understanding how sorption behav-

ior depends on the material morphology. Here we investigate the imbibition behavior of well-controlled cement foams. In contrast to autoclaved aerated concrete, the studied cement foams are open-cell foams with cell window size that depends on both pore size and foam density. We show that those pore windows control the imbibition properties of such material. Moreover, choice made for the surfactant when preparing cement foam is proven to be crucial.

6.2 Materials and methods

6.2.1 Materials

Two surfactants are used: tetradecyltrimethyl ammonium bromide (TTAB) provided by Sigma-Aldrich and Steol[®] 270 CIT provided by Stepan. The main difference between the surfactants lies in the charge of the hydrophilic head: TTAB is positively charged and Steol negatively charged. This leads to different adsorption behavior on cement grains surface. More information about these surfactants and their behavior in cement paste can be found in reference [8].

We use two different cements; their compositions and physical properties are specified in Table 6.1. The first is used in TTAB samples and will be referred to in the following as C1; it is manufactured by Lafarge, in Saint-Vigor factory. C2 is used in Steol samples and is a CEM I cement from Lafarge, Lagerdorf.

	C1	C2
CaO/SiO ₂	3	3
MgO	1.1%	0.8%
Na ₂ O + 0.658 K ₂ O	0.34%	0.5%
SO ₃	2.58%	2.5 %
Cl ⁻	0.03%	0.04 %
Gypsum	2.4%	4%
Density (g/cm ³)	3.21	3.15
SSB (cm ² /g)	3586	4330

Table 6.1: Chemical and physical properties of cements. C1 refers to CEM I cement from Lafarge, Saint-Vigor and C2 to CEM I cement from Lafarge, Lagerdorf.

6.2.2 Cement foam production

To prepare cement foam samples, we mix a precursor aqueous foam with a cement paste. Precursor foam is made from a surfactant solution in distilled water and from nitrogen gas. For each sample, all the bubbles have the same size. They are generated through a 100 μm size T-junction with two entrances, one for gas and one for foaming solution. Then they are collected in a column, where the foam is kept at constant liquid fraction

until it is mixed to cement paste. Perfluorohexane is sometimes added to nitrogen during precursor foam generation to avoid destabilization of cement foams samples (see chapter 5).

Cement paste is prepared by mixing water and cement. In the case of Steol samples, large amount of surfactant is added to cement paste before the mixing with precursor foam to reduce its yield stress (see chapters 4 and 5). Mixing of precursor foam and cement paste is then carried out with millimeter-sized channels, which does not break the bubbles. Fresh cement foam is then poured in 26-mm diameter and 6-cm high airtight molds.

Cement foam preparation protocol is kept constant for all the samples to avoid effect of cement age on the results. All samples are demolded one week after preparation and kept in a box at 100% humidity for three weeks before the imbibition experiment.

6.2.3 Characterization of the foam morphology

The cement foam production method allows us to obtain samples with very well controlled morphology. The morphology does not depend on the surfactant. Bubble radius R of the cement foam samples is equal to the bubble radius of the precursor foam and the radius of the cell windows R_{op} depends on R and the air volume content Φ (or solid volume content $\Phi_s = 1 - \Phi$).

Two samples are scanned with X-ray tomography after cement hardening. The obtained images are analyzed with image analysis software to extract the bubble radius R and size of the openings between the bubbles. We can check in Fig. 6.1 that the average bubble radius for both samples is equal to the radius of the bubbles in the precursor foam.

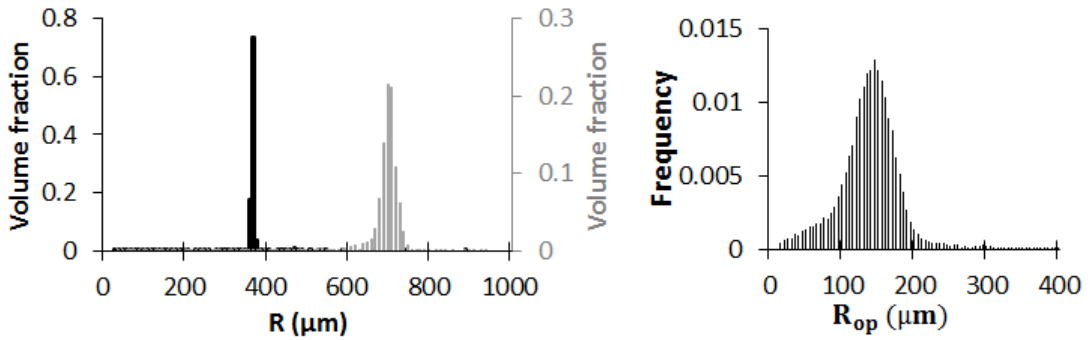


Figure 6.1: Bubble size distribution and opening size distribution obtained by X-ray tomography on hardened cement foam samples at 83% air fraction. Left: Bubble size distribution by volume for TTAB sample with precursor foam bubble radius 370 μm (black, left axis) and Steol samples with precursor foam bubble radius 685 μm (grey, right axis). Right: Window size distribution for TTAB sample with $R=370 \mu\text{m}$.

Area of the windows between the bubbles is related to the solid volume fraction Φ_s by $S(\Phi_s) \equiv \pi R_{op}^2 \approx S_0 \left(1 - \sqrt{\frac{\Phi_s}{\Phi_{s,c}}}\right)$ where $\Phi_{s,c} = 0.36$ and S_0 is the surface of the films when $\Phi_s \rightarrow 0$ [9]. S_0 can be estimated for instance for an hexagonal face in a Kelvin-Voigt bub-

bles: $S_{0,Kelvin} = \frac{3\sqrt{3}}{2} \left(\frac{\pi}{6\sqrt{2}} \right)^{2/3} R^2$ [9]. Therefore, the opening radius can be estimated by the following equation:

$$R_{op} \approx R \sqrt{\frac{3\sqrt{3}}{2\pi} \left(\frac{\pi}{6\sqrt{2}} \right)^{2/3} \left(1 - \sqrt{\frac{\Phi_s}{\Phi_{s,c}}} \right)} \quad (6.1)$$

For $\Phi_s = 0.17$ and $R = 370 \mu\text{m}$, the calculated value of the window size is $R_{op} \approx 140 \mu\text{m}$; it fits well with the average value obtained from the tomography pictures (see size distribution in Fig. 6.1, right).

6.2.4 Permeability measurement

Gas-flow permeability was measured with a home-made setup (see Fig. 6.2). A gas flow controller was used to push dry nitrogen through the foam sample (length L and circular cross-section $S = 5.3 \text{ cm}^2$) embedded with PTFE ribbon and fitting a cylindrical tube. The pressure difference ΔP across the sample was measured thanks to a manometer. Several measurements were performed as a function of the gas flow rate Q (see a typical measurement in Fig. 6.2). The foam permeability was deduced from the Darcy law:

$$k = \frac{\eta L / S}{d(\Delta P) / dQ} \quad (6.2)$$

where $\eta = 1.8 \cdot 10^{-5} \text{ Pa}\cdot\text{s}$ is the dynamic viscosity of the gas.

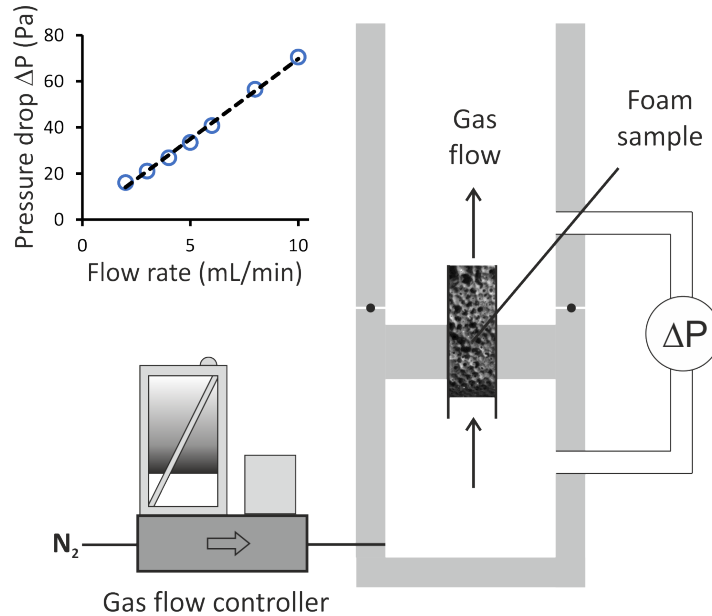


Figure 6.2: Setup used for measuring air-flow permeability of cement foams. A gas flow controller is used to push nitrogen at volume flow rate Q through the foam sample. The pressure difference ΔP across the sample is measured thanks to a manometer. A typical example for the resulting $\Delta P(Q)$ curve is presented.

6.2.5 Imbibition experiment

Water imbibition was studied by measuring the capillary rise through foam samples. Samples were put in contact with a thin layer (5 mm) of water in a 30-cm diameter container. The diameter of the container is large compared to the sample dimension so that we can assume that the height of the liquid layer does not vary during an experiment. The rising front was followed using a camera (see the picture in Fig. 6.4).

6.3 Results and discussion

Results for foam permeability are presented in Fig. 6.3 as a function of solid volume fraction Φ_s , for several samples with different pore radius R , and for both TTAB and Steol surfactants. Note that it is more convenient to plot the dimensionless permeability, i.e. $k/V_b^{2/3}$, with $V_b = 4/3\pi R^3$, because $k/V_b^{2/3}$ is expected to depend only on Φ_s . Fig. 6.3 shows such a behavior, where $k/V_b^{2/3}$ decreases from 0.018 to 0.010 as Φ_s increases from 0.1 to 0.17. Note that permeability values are close for the two studied surfactants. We have reported theoretical values provided by *Lusso & Chateau* for the foam permeability of disordered monodisperse foams [10]. It can be seen that this theoretical curve is in very good agreement with our data. In the following, we will refer to that curve for estimating foam permeability of our foam samples.

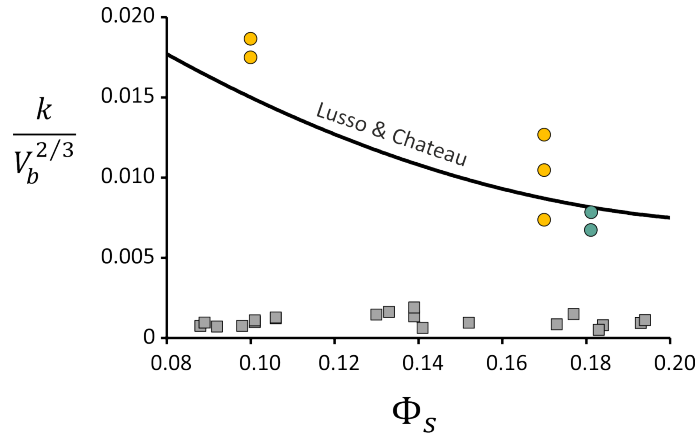


Figure 6.3: Results for cement foam permeability as measured by gas flow experiment (circles: yellow for TTAB samples and green for Steol samples) and deduced from imbibition experiment using equation 6.4 (squares). The black line corresponds to the theoretical values provided by *Lusso & Chateau* [10].

Typical results for water imbibition are presented in Fig. 6.4. All TTAB foam samples reach the height $h = 1$ cm within 1 s. After the rapid rising regime, data show a stair-shape curve in the linear-log scale. This behavior is related to the saturation height (the so-called Jurin height) for imbibition of the foam pores. The further increase of the front height can be explained by the imbibition of the foam porous skeleton (i.e. cement matrix), which is characterized by a much lower imbibition velocity. Note that the second

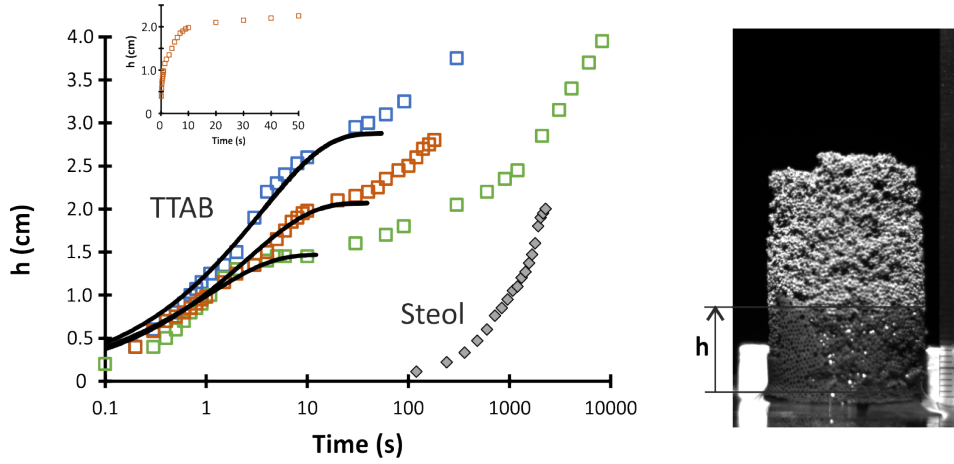


Figure 6.4: Typical imbibition curves, i.e. water capillary rising height as a function of time, for TTAB and Steol cement foams. Such curves are obtained from images of the foam samples (see left picture, sample diameter: 26 mm), showing clearly the water rising front. Blue squares: TTAB, $\Phi_s = 0.14$, $R = 265 \mu\text{m}$. Orange squares: TTAB, $\Phi_s = 0.10$, $R = 360 \mu\text{m}$. Green squares: TTAB, $\Phi_s = 0.10$, $R = 550 \mu\text{m}$. Grey diamonds: Steol, $\Phi_s = 0.18$, $R = 575 \mu\text{m}$. Solid lines correspond to equation 6.4 fitted to experimental data using $\gamma = 0.065 \text{ N/m}$ and $\mu = 0.001 \text{ Pa}\cdot\text{s}$, with the following parameters: Blue squares ($\bar{r} = 460 \mu\text{m}$, $k = 3.5 \cdot 10^{-10} \text{ m}^2$). Orange squares ($\bar{r} = 640 \mu\text{m}$, $k = 3.5 \cdot 10^{-10} \text{ m}^2$). Green squares ($\bar{r} = 900 \mu\text{m}$, $k = 6 \cdot 10^{-10} \text{ m}^2$). Inset: data (TTAB, $\Phi_s = 0.10$, $R = 360 \mu\text{m}$) with linear scale for time.

imbibition regime corresponds to long times, i.e. several hours, so within our experimental conditions water evaporation is expected to take place. As we are mostly interested in the imbibition properties provided by the foam geometry of such cement material, rather than the intrinsic imbibition properties of the cement matrix, in the following we consider only the first and rapid regime. Note that in this regime, the volume of absorbed water is $\Omega(t) = (1 - \Phi_s) \times h(t)$.

Let us briefly recall the classical theory for capillary imbibition of liquids through porous media. By introducing the mean curvature for the water interface in the pores, $1/\bar{r}$, the driving capillary pressure is given by the Laplace law: $2\gamma/\bar{r}$. The progression of the interface at height h is restrained by gravity, so the effective driving pressure is $\Delta P = 2\gamma/\bar{r} - \rho gh(t)$. The resulting interface velocity can be estimated via the Darcy law: $V_D = k/\mu \times \Delta P/h$, where $V_D = \Phi dh/dt$ is the Darcy velocity. The equation for the evolution of the interface height is therefore:

$$v_1 \equiv \frac{dh}{dt} = \frac{2\gamma k}{\Phi \mu \bar{r}} \frac{1}{h} - \frac{\rho g k}{\Phi \mu} = \frac{a}{h} - b \quad (6.3)$$

where parameters $a = 2\gamma k/(\Phi \mu \bar{r})$ and $b = \rho g k/(\Phi \mu)$ have been introduced. Note that the ratio a/b corresponds to the Jurin height: $h_\infty = 2\gamma/(\rho g \bar{r})$. The solution of equation 6.3 is given by [4]:

$$t = -\frac{h}{b} - \frac{a}{b^2} \ln\left(1 - \frac{bh}{a}\right) \quad (6.4)$$

Equation 6.4 is plotted against experimental data for TTAB cement foams in Fig. 6.4.

Note that the value for the saturation height sets the value for \bar{r} , so fitting equation 6.4 to our data provides the expected value for the foam permeability k . Following such a procedure, we obtain values for \bar{r} and k presented in Figs. 6.5 and 6.3 respectively. Let us first discuss values obtained for \bar{r} : the radius of curvature of the interface is set mainly by the pore size, and secondarily by solid volume fraction Φ_s (see Fig. 6.5). This result is consistent with the theory of capillarity in thin tubes, as expressed by the Jurin law: smaller pores induce smaller radii of curvature, and consequently larger capillary pressures. The observed relation between \bar{r} and bubble size can be approximated by: $\bar{r} \approx 1.5R$. Note that for a perfectly wetting cylindrical tube of radius R , one would have $\bar{r} \approx R$. This deviation reflects the complex pore shape in foam and the numerous gaps (windows between pores) located around each pore. Note that the foam pore shape geometry with solid struts and gaps has some similarity with bundles of cylindrical fibers as studied by *Princen* [11]. Of course, the size of those gaps decreases as Φ_s increases, i.e. the surface area covered by solid walls increases, and this could explain the weak effect observed for Φ_s .

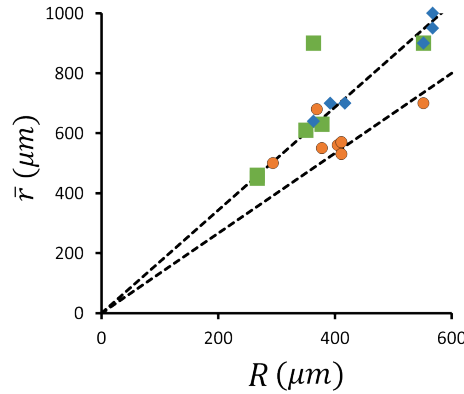


Figure 6.5: Radius of curvature for the water/air interface in cement foam samples, as deduced from equation 6.4, as a function of the pore size. Different symbols are used for indicating the solid volume fraction of the foam samples: blue diamonds ($\Phi_s \approx 0.10$), green squares ($\Phi_s \approx 0.15$) and orange circles ($\Phi_s \approx 0.20$). The dotted lines correspond to equations $\bar{r} = 1.32R$ and $\bar{r} = 1.72R$.

Permeability values deduced from imbibition results (see Fig. 6.3) are found to be one order of magnitude smaller than measured foam permeability, i.e. within the range $0.2\text{--}0.6 \cdot 10^{-10} \text{ m}^2$. In other words, using the measured foam permeability values in equation 6.4 would give imbibition velocity 10 times larger than observed velocity. In order to understand the physical origin of this deviation, we have taken images of the imbibition process with a larger image frequency (100 i/s) and a higher magnification. Such image sequence is presented in Fig. 6.6 as a single spatio-temporal image (image width corresponds to time). This reveals how the water front proceeds during rising through the porous structure: from pore to pore, the capillary ascending motion pauses regularly, and the durations of those pauses appear to be distributed within the range $0.05 \text{ s} - 0.2 \text{ s}$. It is recognized that interface motions can be slowed down or even stopped by passing through pore junctions or through capillaries with significant expansion of the cross-section [12, 13, 14]. We therefore attribute the observed pauses to the windows between the pores, where the interface is expected to flatten, i.e. $\bar{r} \rightarrow \infty$, for satisfying contact

angle conditions at sharp edges constriction geometry [13]. This means that the driving capillary pressure drops at pore windows and then spreading of thin precursor film emanating from the rising liquid promotes the sudden pull-up of the interface in the new pore, where equilibrium contact angle conditions can be recovered. Note that the porous nature of the cement skeleton may contribute to such breakthrough. This process takes the time identified as the pauses during imbibition (see Fig. 6.6 (c)).

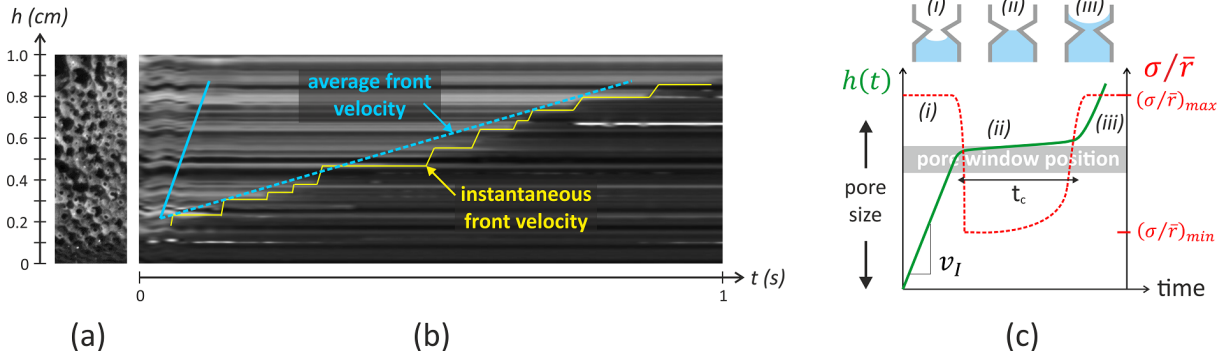


Figure 6.6: Capillary water imbibition observed at the pore scale. (a) Image of the foam sample and (b) spatio-temporal image (width corresponds to time: 1 pixel = 0.01 s) of the water rising front (yellow curve) observed at frame rate of 100 images per second. A stair-shape curve is obtained, which means that the capillary ascending motion pauses regularly. The dotted line corresponds to the average front velocity with slope (dh/dt) , whereas the continuous line shows the slope $10 \times (dh/dt)$. (c) Schematic plot of the interface ascending motion at pore scale, where the rising velocity is v_I for the main part of the pore – i.e. areas (i) and (iii), whereas it drops down to a low value at pore window, i.e. area (ii). Configurations of the interface are shown by sketches (i), (ii) and (iii). The evolution of the driving capillary, i.e. γ/\bar{r} , is also presented: first it drops down at pore window, and it rebuilds after a characteristic time t_c .

We propose to account for the effect of the pauses by introducing the average duration t_c spent by the interface between two neighbor pores during the vertical motion (see Fig. 6.6). The dynamics of the vertical motion between two successive stops can still be considered as mainly governed by the balance between capillary effects and Darcy's law (leading to equation 6.4). Therefore, the average time for the interface to travel a length $2R$ is equal to $2R/v_I + t_c$, and the modified imbibition velocity is given by:

$$v_{I,t_c} = \frac{2R}{\frac{2R}{v_I} + t_c} = \frac{v_I}{1 + \frac{v_I}{2R/t_c}} \quad (6.5)$$

In the following we choose to use k values provided by *Lusso & Chateau* [10] (see Fig. 6.3) and to consider t_c as a fitting parameter such as $t_c = t_0(1 + p\frac{h}{t_0})$, where t_0 is a minimal time and coefficient p accounts for the slowdown effect of gravity (time t_c is expected to increase as a function of height). Parameters t_0 and p can be determined by fitting equation 6.5 to our data. In practice, we chose h_i values within the range of interest and we calculate the corresponding times $t_i = t_{i-1} + (h_i - h_{i-1})/(v_{I,t_c})_i$, where $(h_i - h_{i-1})$ correspond to small steps. Results obtained by fitting equation 6.5 to data from Fig. 6.4

are presented in Fig. 6.7, showing reasonable agreement. Note that both \bar{r} and k values are now consistent. This procedure is performed for all samples, providing values for the fitting parameters: $t_0 \approx 0.005$ s, and p is shown in figure E (inset), where the average value is given by $p \times R \approx 0.005$ s. This corresponds to $p \approx 0.1$ s/cm, or equivalently, the average time t_c is approximately equal to 0.1 s for $h \approx 1$ cm, which is consistent with observed pause durations in Fig. 6.6. The additional parameter t_c is therefore useful for reconciling k values and \bar{r} values in the water capillary imbibition process of cement foams, and it shows that pore windows have a significant influence on water imbibition properties. The analysis of p values reveals that p increases with both pore size and gas volume fraction, so does foam permeability. Indeed, recent work showed that $k/R^2 \sim (R_{op}/R)^3$ [15]. We identify a simple relationship between p and k : $(pR)/k \approx 10^6$ s/m², which indicates that the pore halting mechanism depends on geometry of the pore windows. Further study would be useful for clarifying this issue.

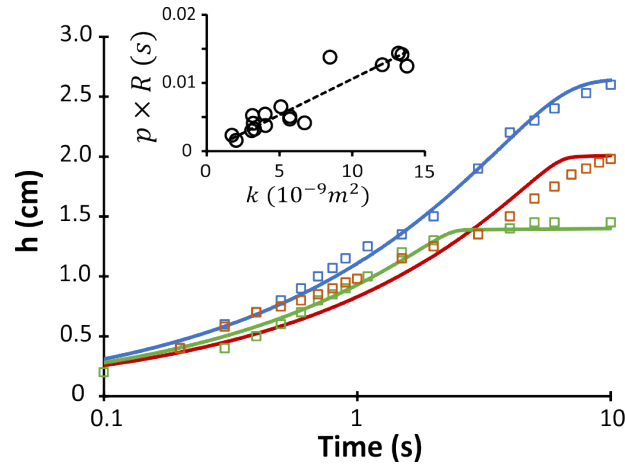


Figure 6.7: Water capillary rising height as a function of time for TTAB cement foams (data from Fig. 6.4). Solid lines correspond to equation 6.5 fitted to experimental data using $\gamma = 0.065$ N/m and $\mu = 0.001$ Pa.s, with the following parameters: Blue squares ($\bar{r} = 460$ μm , $k = 8.5 \cdot 10^{-9}$ m², $t_0 = 0.005$ s, $p = 0.06$ s/cm). Orange squares ($\bar{r} = 660$ μm , $k = 5 \cdot 10^{-9}$ m², $t_0 = 0.005$ s, $p = 0.18$ s/cm). Green squares ($\bar{r} = 950$ μm , $k = 12 \cdot 10^{-9}$ m², $t_0 = 0.005$ s, $p = 0.23$ s/cm). Inset: Results for $p \times R$ as a function of foam permeability for all studied TTAB samples. The dotted line corresponds to equation $pR = 10^6 k$.

Finally we discuss the effect of surfactant. Whereas imbibition velocities for TTAB cement foams were found to be of the order of 1 cm/s, Steol cement foam requires almost 1000 s for the water front to reach $h = 1$ cm (i.e. 0.001 cm/s). Moreover, an “induction period” of almost 100 s is observed before measurable imbibition. In fact, such behavior cannot be described with equation 6.4 whatever the value for k . On the other hand, such slow kinetics can be reconciled with theory using equation 6.5 with $t_c \sim 100$ s. This extremely long time suggests that additional chemical effects are involved, such as the dissolution of dried surfactant remaining onto the cement surface. Note that Steol surfactant has been shown to induce high water contact angles on cement surface, provided that Steol concentration is low enough [8]. Initial Steol concentration is rather high in

this study, but one can expect that Steol molecules, that are known to adsorb significantly on cement/hydrate grains, are consumed by new hydrate surface area, making the Steol concentration drop below a critical value. Therefore, a plausible mechanism for Steol action is (1) the in-situ hydrophobization of the cement skeleton, (2) the surfactant layer remains on the surface of the foam skeleton as the sample is left for drying, and (3) the slow dissolution of the dried hydrophobic surfactant layer by the imbibing water. As TTAB surfactant has not been shown to induce such hydrophobization effect on cement [8], TTAB cement imbibition does not exhibit such specific behavior.

6.4 Conclusion

Water imbibition has been studied in cement foams prepared from two distinct foaming solutions, namely TTAB and Steol surfactant solutions. Thanks to a dedicated foaming method, we were able to produce samples with controlled pore size and gas volume fraction. Results obtained for TTAB show imbibition behavior consistent with Washburn theory if the permeability parameter is used as a fitting parameter. However, fitted values were found to one order of magnitude smaller than theoretical and measured values. Observation of the imbibition process at the pore scale revealed that the capillary ascending motion pauses regularly, which makes the imbibition velocity decrease and explains the low fitted values for the foam permeability. This was attributed to the effect of pore windows, i.e. passages between pores. We have introduced a characteristic time corresponding to the excess time spent by the interface at those pore windows. Using that time as a fitting parameter, we succeed to reconcile measured permeability values with measured imbibition velocities. The fitted values for the characteristic time are of the order 0.1 s, which was found to be consistent with direct observations of the imbibition process at the pore scale. Further work could be useful for evaluating the relevance of our approach for porous materials exhibiting the similar morphological features. Results obtained for Steol show extremely slow imbibition velocities, i.e. 1000 times smaller than for TTAB samples, which cannot be described using the classical Washburn theory. This effect has been attributed to the in-situ hydrophobization of the cement foam skeleton during the production process. As water is put in contact with the foam sample, imbibition is prevented by the water-repellent action of the dried surfactant layer. Imbibition proceeds on condition that the dried surfactant layer is dissolved by the imbibing water as the front goes along. This clearly shows that surfactant used for preparing cement foam has crucial effect on imbibition properties of such porous material.

Bibliography

- [1] C. Ma and B. Chen, "Properties of foamed concrete containing water repellents," *Construction and Building Materials*, vol. 123, pp. 106–114, 2016. [127](#)
- [2] J. M. Bell and F. K. Cameron, "The flow of liquids through capillary spaces," *Journal of Physical Chemistry*, vol. 10, pp. 658–674, 1906. [127](#)

- [3] R. Lucas, "Ueber das zeitgesetz des kapillaren aufstiegs von flüssigkeiten," *Kolloid-Zeitschrift*, vol. 23, pp. 15–22, 1918. [127](#)
- [4] E. W. Washburn, "The dynamics of capillary flow," *Physical Review*, vol. 17, pp. 273–283, 1921. [127](#), [132](#)
- [5] E. Kunhanandan Nambiar and K. Ramamurthy, "Air-void characterisation of foam concrete," *Cement and Concrete Research*, vol. 37, pp. 221–230, 2007. [127](#)
- [6] I. Ioannou, A. Hamilton, and C. Hall, "Capillary absorption of water and n-decane by autoclaved aerated concrete," *Cement and Concrete Research*, vol. 38, pp. 766–771, 2008. [127](#)
- [7] K. Song, J. Mitchell, H. Jaffel, and L. Gladden, "Magnetic resonance imaging studies of spontaneous capillary water imbibition in aerated gypsum," *Journal of Physics D: Applied Physics*, vol. 44, 2011. [127](#)
- [8] B. Feneuil, O. Pitois, and N. Roussel, "Effect of surfactants on the yield stress of cement paste," *Cement and Concrete Research*, vol. 100, pp. 32–39, 2017. [128](#), [135](#), [136](#)
- [9] I. Cantat, S. Cohen-Addad, F. Elias, F. Graner, R. Höhler, O. Pitois, F. Rouyer, and A. Saint-Jalmes, *Foams - Structure and dynamics*. Oxford University Press, 2013. [129](#), [130](#)
- [10] C. Lusso and X. Chateau, "Numerical modeling of disordered foam in 3d: Effective properties by homogenization," in *Poromechanics VI* (M. Vandamme, P. Dangla, J.-M. Pereira, and S. Ghabezloo, eds.), pp. 1347–1354, 2017. [131](#), [134](#)
- [11] H. M. Princen, "Capillary phenomena in assemblies of parallel cylinders. ii. capillary rise in systems with more than two cylinders," *Journal of Colloid and Interface Science*, vol. 30, pp. 359–371, 1969. [133](#)
- [12] H. Wiklund and T. Uesaka, "Microfluidics of imbibition in random porous media," *Physical Review E - Statistical, Nonlinear, and Soft Matter Physics.*, vol. 87, 2013. [133](#)
- [13] H. Mehrabian, P. Gao, and J. Feng, "Wicking flow through microchannels," *Physics of fluids*, vol. 23, pp. 1–14, 2011. [133](#), [134](#)
- [14] Z. Sadjadi, M. Jung, R. Seemann, and H. Rieger, "Meniscus arrest during capillary rise in asymmetric microfluidic pore junctions," *Langmuir*, vol. 31, pp. 2600–2608, 2015. [133](#)
- [15] V. Langlois, V. H. Trinh, C. Lusso, C. Perrot, X. Chateau, Y. Khidas, and O. Pitois, "Permeability of solid foam: Effect of pore connections," *Physical Review E*, vol. 97, p. 053111, 2018. [135](#)

Conclusion

When cement foams are prepared by mixing an aqueous foam and a cement paste, surfactants must be used. We have first selected various surfactants that are compatible with cement solution and investigated their effects on cement paste, without air bubbles. Depending on the type of surfactant and its concentration, addition of surfactant can have three different consequences on cement paste yield stress. (1) Some surfactants have low affinity to cement grains and hardly change the properties of the cement paste. (2) At low concentration, surfactants with high affinity to cement grains (mainly anionic surfactants) form a single layer that makes the cement grains hydrophobic. Hydrophobic interaction increases attraction between cement grains and enhances the yield stress of the cement paste. (3) At high concentration, the same surfactants form micelles on the cement grains surface, which creates a steric repulsion between the grains and makes cement paste yield stress drop.

Then, we have studied aerated cement pastes and cement foams. The identification of the three surfactant regimes has allowed us to control the properties of the produced cement foams, and to analyze the rheological measurements and the stability of the fresh materials, and the water imbibition of the solid foams.

When bubbles are added to cement paste at air fractions below 40%, their effect on the paste yield stress is strongly affected by the surface properties of cement grains. Hydrophobic cement grains irreversibly adsorb on bubble surface; this changes the surface characteristics of the bubbles, so that bubbles enhance the yield stress similarly to solid inclusions. On the other hand, when cement grains are hydrophilic and do not adsorb at air-liquid interfaces, behavior of bubbles in cement paste corresponds to observations in model yield stress fluids: dimensionless yield stress depends on the air volume content and on the deformability of the bubbles.

When air volume content is higher, around 83%, most foams tend to destabilize before cement hardening due to ripening. Unexpectedly, when yield stress of the cement paste τ_y is changed by the addition of superplasticizer or high amount of anionic surfactant, ripening can be stopped if the yield stress is relatively low, in the range $\tau_y^{**} < \tau_y < \tau_y^*$. Rheological measurements on the foam when $\tau_y < \tau_y^*$ show that the yield stress of the interstitial cement paste is greatly increased due to the confinement between the bubbles. In addition, water can be more easily extracted from the interstitial cement paste under gravity when $\tau_y < \tau_y^*$ than when $\tau_y > \tau_y^*$. Our hypothesis is that the yield stress enhancement and remarkable stability in the low yield stress regime is a consequence of the

reorganization of cement grains into a denser granular structure. Destabilization when $\tau_y < \tau_y^{**}$ is attributed to the deflocculated state of the smaller cement particles, which exit the foam skeleton.

Then, we have compared cement foams prepared with two different surfactants, with low and high affinities to cement grains. A stability criterion, independent on the surfactant, can be defined from the bubble radius R , the yield stress of the paste confined by the bubbles $\tau_{y,int}$ and the air-fluid surface tension γ . Foams are stable when the Bingham capillary number, evaluated for the interstitial cement paste at time t^* , is above a critical value. Time t^* is expected to depend on the preparation method of the cement foam.

Further studies on cement foam stability would be needed to understand the role of air volume fraction. In addition, the regime when cement grains are hydrophobic has not been investigated here. We expect that the adsorption of cement grains at air-fluid interfaces leads to the formation of closed porosity. Effect of cement membranes between the bubbles on foam stability and rheology remains to be investigated.

Finally, we have studied the water imbibition of cement foams with open porosity. We have observed that the imbibition is slower than the velocity predicted from the permeability measurement. We have introduced a characteristic time, corresponding to the excess time spent by the water interface at windows between the bubbles, to reconcile measured permeability values with measured imbibition velocities. For surfactant with low affinity to cement grain surface, the fitted values for the characteristic time are of the order 0.1 s, which was found to be consistent with direct observations of the imbibition process at the pore scale. Results obtained for surfactant with high affinity to cement surface shows extremely slow imbibition velocities, i.e. 1000 times smaller. The main reason must be the hydrophobization of the pore walls. This observation illustrates the strong relation between material formulation and its final properties.

Appendix A

Compressive resistance

In this appendix, we report some measurements of compressive strength of cement foams. We compare two surfactants (anionic and cationic). We study mostly samples at air fraction above 75% and a few samples at air fraction below 40%.

A.1 Materials and methods

A.1.1 Materials

Two surfactants and two cements are used. Samples containing TTAB cationic surfactant are made with CEM I cement from Lafarge, Saint-Vigor factory (C1). For samples containing Steol anionic surfactant, CEM I cement from Lafarge, Lagerdorf factory (C2) is used. Manufacturers and chemical formulas of surfactants, and cement chemical compositions can be found in chapter 5.

A.1.2 Sample preparation protocol

Precursor foam is generated as explained in chapters 3, 4 and 5. For each sample, it is mixed with a cement paste. Then samples are cast into 26-mm diameter and 6 cm high sealed molds. Samples are demolded 7 days after preparation and kept in a 100% humidity box for three additional weeks.

Three types of samples are prepared :

- Steol samples with high air content $\Phi \approx 83\%$. Preparation procedure is described in chapters 4 and 5.
- TTAB samples with high air content $\Phi \approx 83\%$. Preparation procedure is described in chapter 5; for the smaller bubble sizes, we use C_6F_{14} during precursor foam preparation to avoid ripening. Often, the density at the top of the sample and at the bottom of the sample are different. These samples are cut in two parts and both parts were weighted to measure their true density. Densities are between 200 and 500 kg/m³, that is to say that the corrected air fractions range from 76% to 92%.

- TTAB sample with low air content $\Phi < 40\%$. Preparation procedure is described in chapter 3. In particular, precursor foam is incorporated by hand into the cement paste.

A.1.3 Compression tests

All samples are tested in average 28 days after production (between 25 and 35 days). Samples are cut so that final height is between 25 and 35 mm.

Different presses are used for the different types of samples according to the needed crushing force required :

- Steol samples are tested with a press with maximal force 500 N at speed 0.1 mm/s. Before the test, sample ends are plastered to create flat parallel surfaces as shown in Fig. A.1.
- TTAB samples at high air content are tested with a press with maximal force 20 kN at speed 0.1 mm/s. Before the test, sample ends are plastered to create flat parallel surfaces as shown in Fig. A.1.
- TTAB samples at low air content are tested with a press with maximal force 100 kN at speed 1 mm/min = 0.016 mm/s. Sample top and bottom faces are filed so that their are flat and parallel. The surfaces are not plastered, but rubber layers are placed at the top and bottom of the sample during the compression test.

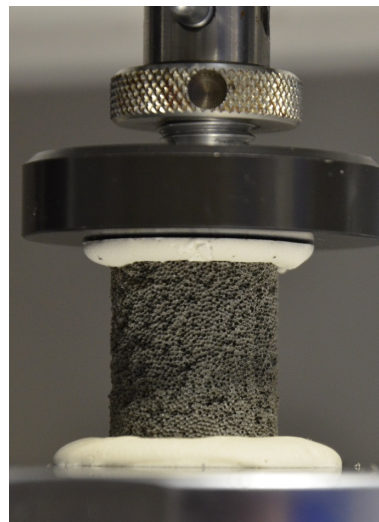


Figure A.1: Steol cement foam sample ($\Phi = 83\%$, $R = 380 \mu\text{m}$) ready for compression test. All the Steol and TTAB samples at air fraction above 75% have been plastered in order to make flat parallel ends.

A.2 Results and discussion

A.2.1 Curve shape

A.2.1.1 Air content $\Phi > 75\%$, Steol and TTAB samples

Examples of stress-strain curves for some samples with high air content are shown in Fig. A.2. Usually, a first peak occurs, then stress increases again.

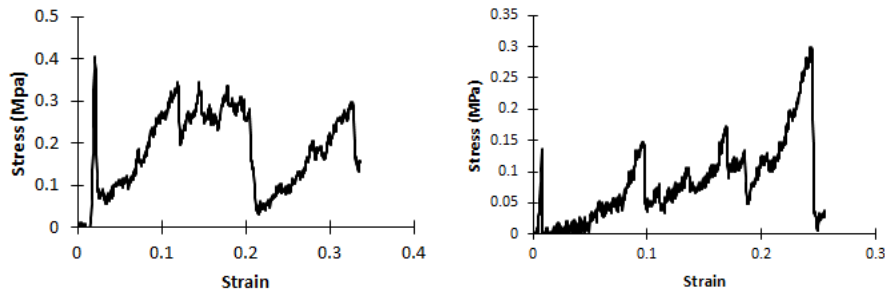


Figure A.2: Examples of stress-strain curve obtained during compression tests of TTAB samples with air content above 74%. Left: $\sigma_{peak} = \sigma_{max} = 0.40 \text{ MPa}$. Right: $\sigma_{peak} = 0.14 \text{ MPa}$ and $\sigma_{max} = 0.30 \text{ MPa}$

Two values can be extracted from these curves: the stress at the peak σ_{peak} and the maximal reached stress σ_{max} . For most of the samples, both values are the same order of magnitude, and sometimes, the maximal value is reached at the first peak.

With Steol samples, the press force is sometimes not enough to break the samples ; therefore, the peak value and the maximal value cannot be always measured.

We can compare this shape with a typical curve of brittle foam material [1] shown in Fig. A.3. In this typical curve, three phases can be seen. First, in the elastic regime, stress increases linearly up to a σ_{peak} . When σ_{peak} is reached, foam locally breaks. After this first rupture, during the the "plateau" regime, broken area expands: the more strain increases, the more Plateau borders are broken. When deformation approaches the air volume fraction Φ , amount of air voids in the crushed sample is very small and further increase leads to the compaction of the broken Plateau borders and nodes (densification) and then to compression of the plain material itself. In this typical curve, the peak value is the maximal stress before the beginning of densification.

In our case, densification phase is never achieved. Compression of plain cement paste should occur when deformation is nearly the initial air volume fraction Φ , but maximal deformation of our samples is 30% whereas air volume fraction of the denser samples is 75%. Therefore, the presence of distinct values for σ_{peak} and σ_{max} would not occur if the samples were homogeneous. A possible explanation is that σ_{peak} is the resistance of the weakest areas of the sample and σ_{max} , the resistance of the strongest areas.

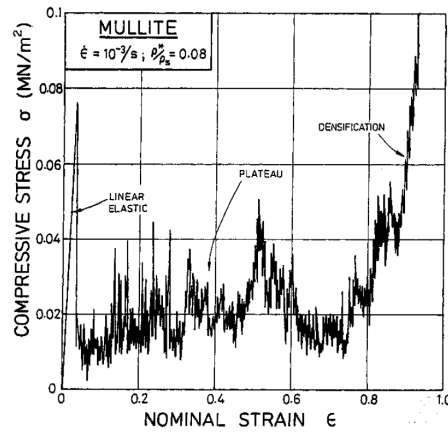


Figure A.3: Stress-strain curve during compression test of a brittle foam, deformation rate is 10^{-3} and air fraction, $\Phi = 92\%$ [1].

A.2.1.2 Air content $\Phi < 40\%$

Initial stress peak can also be observed when air content is below 40%, but the stress decrease after the first peak is small. In addition, the peak value is much lower than the maximum value, often one order of magnitude below.

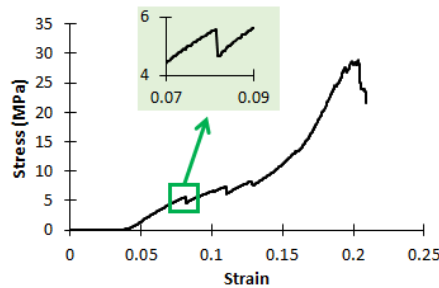


Figure A.4: Example of stress-strain curve obtained during a compression test, for a TTAB sample containing 8% of air.

When the maximum value is reached, several cracks have formed in the sample.

A.2.2 Compression resistance

A.2.2.1 Comparison with literature

Comparison of the resistance with data from literature (seen chapter 1) is presented in Fig. A.5. Note that air fraction is related to the density by the following equation:

$$\rho = \rho_{paste}(1 - \phi) \quad (A.1)$$

Where ρ_{paste} is the density of the paste without the bubbles and is related to the water-to-cement ratio by the formula:

$$\rho_{paste} = \frac{W/C + 1}{\frac{W/C}{\rho_E} + \frac{1}{\rho_C}} \quad (A.2)$$

Paste density decreases from 1950 kg/m³ when W/C=0.40 to 1835 kg/m³ when W/C=0.50.

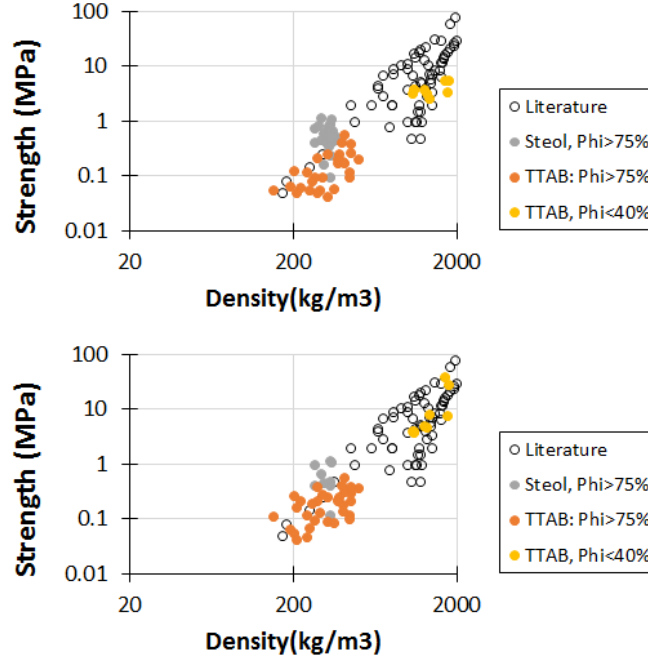


Figure A.5: Comparison of the measured strength with the results from the literature. Top: peak value σ_{peak} . Bottom: maximal value σ_{max} .

We can first note that the measured values are the same order of magnitude as literature values for low densities (i.e. $\Phi > 75\%$). For high density samples, maximal stress fits with literature values whereas peak stress is lower.

A.2.2.2 Effect of surfactant

As seen in Fig. A.5, compressive strengths for Steol foam samples are bigger than for samples containing TTAB, the difference is certainly larger than what appears in the graph because some of the Steol samples have not been broken. This can be explained by a stronger matrix in the case of Steol samples. Water-to-cement ratios are similar for both types of samples: between 0.39 and 0.5 with average value 0.43. However, cement C2 used to prepare Steol foams has smaller grains than C1, used in TTAB sample: Blaine specific surface area is 3586 cm²/g for C1 and 4330 cm²/g for C2. Therefore, C2 is expected to hydrate faster than C1 and to reach a higher degree of hydration of cement at 28 days, which increases the cement paste strength.

A.2.2.3 Effect of W/C

Decreasing water-to-cement ratio is expected to increase the strength of the interstitial cement paste, and therefore, increase the strength of the cement foams. The results for

cement W/C are plotted in Fig. A.6 for bubble size from 990 to 1100 μm . No effect of water-to-cement ratio can be seen on these graphs. No conclusion can however be drawn because of the large dispersion of the results.

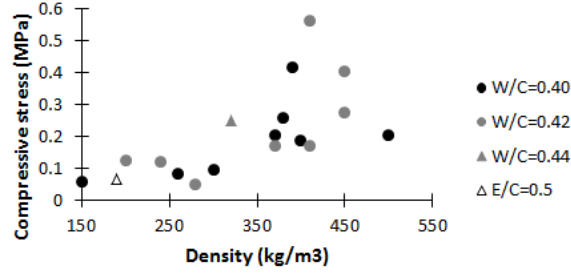


Figure A.6: Peak compressive strength for TTAB foams samples with bubble size 990-1100 μm , for several water-to-cement ratios.

A.2.2.4 Effect of bubble size

Peak stress results on TTAB foams and bubble suspensions are detailed in Fig. A.7 for several bubble sizes.

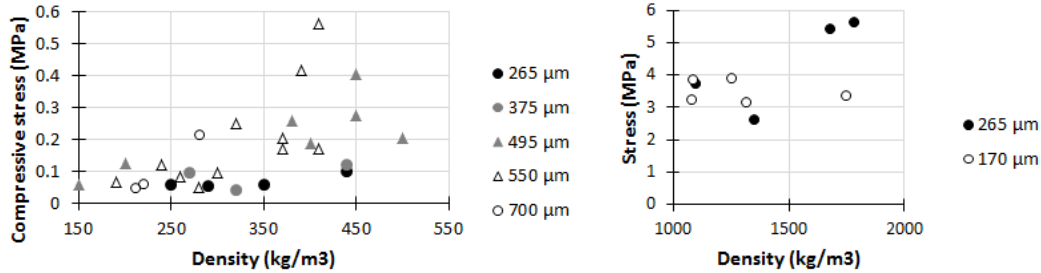


Figure A.7: Dependence of the measured strength σ_{peak} on the bubble radius for TTAB foams (left) and bubble suspensions (right).

In the low air fraction regime, no major effect of bubble size can be seen.

On the contrary, for $\Phi > 75\%$, strength decreases when bubble radius decreases. This effect may be due to a poor mixing in the samples containing the smaller bubbles. Indeed, areas of cement paste without bubbles can be seen. From the tomography images of a TTAB sample of bubble radius 370 μm and air fraction 83%, we measure the size of bubble-free areas and their total volume. A few of these areas have volume between 1 and 30 bubble size, and there is a large area of nearly 400 bubble volume. All together, they compose 12% of the total sample volume. Therefore, effective air content of the foam around these areas between bubbles is:

$$\Phi_{eff} = 1 - \frac{(1 - \Phi) - \Phi_{defaults}}{1 - \Phi_{default}} \approx 94\% \quad (\text{A.3})$$

This value corresponds to a density $\rho \approx 110 \text{ kg/m}^3$. Very few values of mechanical resistance can be found in the literature at this very low density. We can for instance mention the work of *Tonyan and Gibson* [2], who created foams at density 170 kg/m^3 and mechanical resistance 50 Pa . They used polyester fibers to reinforce the cement paste matrix. In our case, we obtain similar compressive strength for a simple cement paste matrix, without fiber reinforcement.

The difficulty to obtain a good mixing may be related to the small size of the Plateau borders when bubble radius is small. The diameter of the bigger spheres that can fit in the Plateau borders is given by equation 5.13. The values calculated for several bubble radius and air fractions are summarized in Table A.1. For C1 cement, grains of size above $60 \mu\text{m}$ compose 5% of the total volume of cement grains (for C2, 5% volume is filled by grains size above $40 \mu\text{m}$). That is to say that if Plateau border diameter is below $60 \mu\text{m}$, 5% of the grains must remain in the nodes.

	$\Phi=75\%$	$\Phi=80\%$	$\Phi=85\%$	$\Phi=90\%$	$\Phi=95\%$
R=200 μm	59 μm	46 μm	36 μm	28 μm	20 μm
R=300 μm	88 μm	70 μm	54 μm	42 μm	29 μm
R=400 μm	118 μm	93 μm	73 μm	56 μm	39 μm
R=500 μm	147 μm	116 μm	91 μm	70 μm	49 μm
R=600 μm	177 μm	139 μm	109 μm	84 μm	59 μm

Table A.1: Plateau border diameter at given bubble size and air volume fraction. Values in red indicate that at least 5% of the volume of C1 cement grains cannot fit in the Plateau borders.

A.3 Conclusion

Measured strength are the same order of magnitude as the values measured in the literature.

However, we have measured an unexpected effect of bubble size on TTAB samples at air fraction above 75%. The poor mixing, that has been observed on some samples with small bubbles, can account for this effect.

Bibliography

- [1] L. Gibson and M. Ashby, eds., *Cellular Solids: Structure and Properties*. Cambridge: Cambridge University Press, 1997. III, IV
- [2] T. D. Tonyan and L. J. Gibson, "Structure and mechanics of cement foams," *Journal of Material Science*, vol. 27, pp. 6371–6378, 1992. VII